Titanium, Iron, Neutrinos, and Asymmetric Explosions:

An Exploration of Supernovae and Their Remnants

by

Gregory Vance

A Dissertation Presented in Partial Fulfillment
of the Requirements for the Degree
Doctor of Philosophy

Approved November 2021 by the
Graduate Supervisory Committee:

Patrick Young, Chair
Evan Scannapieco
Cecilia Lunardini
Rogier Windhorst
Sumner Starrfield

ARIZONA STATE UNIVERSITY

December 2021

ABSTRACT

The lives of high-mass stars end with core-collapse supernovae, which distribute energy and chemical elements into the interstellar medium. This process is integral to the Galactic ecosystem, since stars and planets will form from the enriched interstellar medium. Since most supernovae are detected at intergalactic distances, opportunities to examine them in detail are rare. Computer simulations and observations of supernova remnants are frequently employed to study these events and their influence on the universe.

I explore the topic of supernovae using a multi-pronged approach, beginning with an examination of the core-collapse supernova engine. The radioisotopes ^{44}Ti and ^{56}Ni, produced in the innermost ejecta, provide a probe of this central engine. Using a three-dimensional supernova simulation with nucleosynthesis post-processing, I examine the production of these isotopes and their thermodynamic histories. Since production of ^{44}Ti is especially sensitive to the explosion conditions, insights can be gained by comparing the model with ^{44}Ti observations from supernova remnant Cassiopeia A.

Next, I consider supernova remnants as potential sources of high-energy neutrinos within the Milky Way galaxy. The developing field of neutrino astronomy has yet to identify the origins of the diffuse neutrino flux first detected by the IceCube Neutrino Observatory in 2013. In principle, high-energy Galactic sources like supernova remnants could contribute measurably to this flux. I also consider Galactic open clusters, environments which are rich in supernovae and other energetic phenomena. Statistical analysis finds no evidence of causal association between these objects and the IceCube neutrino events.

I conclude with a series of asymmetric three-dimensional supernova models, presented as a comparative analysis of how supernova morphology affects nucleosynthetic yields. Both real supernovae and simulations frequently exhibit aspherical morphologies, but the detailed thermodynamic consequences and the ultimate effects on yields are poorly understood. The simulations include symmetric and bipolar explosion geometries for both 15- and 20-solar-mass progenitor stars. Across the spectrum of models, I show how small changes in the peak temperatures and densities experienced by ejecta can influence the production of notable isotopes such as ^{44}Ti.

DEDICATION

To my wife, Rhonda. I never could have gotten this far alone.

TABLE OF CONTENTS

Page

CHAPTER Page

LIST OF TABLES

LIST OF FIGURES

Chapter 1

INTRODUCTION TO SUPERNOVAE

1.1 Overview

In the aftermath of the Big Bang, nearly all the matter in the newborn universe was left in the form of either hydrogen or helium atoms. Billions of years later, these two elements still comprise most of the available matter, but the metallicity of the universe has increased measurably. The Sun, which formed 4–5 billion years ago, consists of $Z_\odot \approx 1.4\%$ heavier elements (Lodders, 2010). Today's universe contains a variety of chemical elements—including carbon, nitrogen, oxygen, aluminum, silicon, and iron—which are sufficient to allow for the existence of rocky, life-hosting planets like Earth. The lengthy story of cosmic chemical evolution that brought about this fundamental change of composition in the universe has many important characters, but some of the most significant are high-mass stars and the core-collapse supernovae that end their lives.

Stars with a mass of $\sim$10 $\mathrm{M}_\odot$ or higher will eventually produce nuclei as heavy as iron in their cores via nuclear fusion as they reach the final stages of their lives. Once the star is able to extract no further energy from the process of nuclear fusion, its core collapses under gravity and the outer layers of the star are violently ejected in a supernova explosion. The supernova not only distributes the fusion products produced in the stellar interior during the star's life, but it also momentarily provides conditions of extreme temperature ($T \sim 10$ GK) and density ($\rho \sim 10^7$ g/cm^3) that allow for the fusion of r-process nuclei far heavier than iron. Material from the expanding supernova remnant can find its way deep into giant molecular clouds, which will eventually collapse to form new stars and planets with greater chemical diversity.

Studying the products of supernovae in detail can give insights into a range of astrophysical questions. For example, the distributions of iron and radioactive ^{44}Ti in a supernova remnant provide a probe of the explosion conditions in the innermost ejecta, in turn offering clues about the central engine of the supernova itself. Supernova remnants also represent the most probable population of Galactic cosmic ray accelerators (Blasi, 2013). If high-energy neutrino detections were found to spatially correlate with nearby supernova remnants, it would validate this hypothesis and represent a major step forward in solving the mystery of cosmic ray origins. Finally, the wider set of nucleosynthetic yields from a supernova shows cosmic chemical evolution in the making. Yields are strongly variable, sensitive to properties of the progenitor star and the morphology of the explosion, and they offer a laboratory for testing the predictions of nuclear physics models. This list is by no means exhaustive, but instead has been chosen to highlight the approaches that will be explored in this work.

Regrettably, opportunities for truly detailed study of supernova explosions "in the wild" are rare, since most supernovae are detected at intergalactic distances. Supernovae that are near enough to be resolved with telescopes occur with a frequency of only $\sim$1 century^{-1}, so a fortunate astronomer can perhaps expect to witness one such event over the course of a lifetime. Due to these inconvenient limitations, a large portion of supernova research focuses on either running computer simulations or observing supernova remnants, since both of these options are generally more accessible.

Computer simulations are an essential tool for studying the physics and nucleosynthesis of supernovae on human timescales, and they have become more sophisticated with the increasing availability of computing power since the 1990s. The rise of data visualization tools has also enhanced researchers' ability to interpret and share the results of complex simulations. These models provide a controlled environment in which current understanding of the driving physics behind stellar lives and deaths can be repeatedly tested against observational data. Modern simulations still leave much to be desired, but the iterative process of pushing models into closer agreement with observations can ideally help to refine the assumptions that underlie the models.

Supernova remnants are capable of persisting for millennia, working their way through stages of expansion and evolution long after the brightness of the initial explosion has waned. There are ~300 known Galactic supernova remnants with assorted ages, distances, fluxes, and morphologies (Green, 2014, 2017). Some are comparatively young and nearby, making for bright astronomical sources that have been well studied across the electromagnetic spectrum. One prominent example is Cassiopeia A (Cas A), which is one of the best-studied supernova remnants (e.g., Hwang *et al.*, 2004; Krause *et al.*, 2008; Grefenstette *et al.*, 2017). But there are also scores of little-known wispy specters, ancient by human standards, that are sometimes barely identifiable as supernova remnants. These are often difficult to observe due to their extremely low brightness, which limits how much can be learned about them.

1.2 Titanium and Iron

Thirty-four years ago, SN 1987A provided an unparalleled opportunity for astronomers to study a nearby supernova in detail. Observations of ^{56}Ni mixing in the explosion led to the development of a model for the core-collapse supernova engine which depends on hydrodynamic instabilities above the forming neutron star (Herant and Benz, 1992; Herant *et al.*, 1994). This model has weathered the trials of more than 20 years of verification to become the standard supernova engine paradigm. One way to begin to understand the finer details of this central engine is to examine the isotopes ^{44}Ti and ^{56}Ni, both of which are produced in close proximity to the engine itself.

Due to emission from radioactive decay, ^{44}Ti is readily observable at X-ray energies, and its half-life of ∼60 yr means that it can still be detected in remnants that are hundreds of years old. Production of both ^{44}Ti and ^{56}Ni depends on radiation entropy and α-rich freeze-out conditions (Thielemann *et al.*, 1996), with yields of ^{44}Ti being especially sensitive. Since ^{56}Ni is produced under the same conditions and decays to ^{56}Fe via ^{56}Co with half-lives of less than 90 days, observations of iron abundance in supernova remnants are often used in concert with ^{44}Ti as diagnostics of the deep internal supernova conditions. Detailed study of the production of ^{44}Ti and iron (plus ^{56}Ni) in both computer models and supernova remnants can lead to insights about the thermodynamic conditions in the midst of the explosion.

1.3 Neutrinos

Supernova remnants are also of interest to the field of particle astrophysics, where their status as energetic sources makes them theoretically well motivated as cosmic particle accelerators. The Galactic population of supernova remnants is almost certainly responsible for the bulk of hadronic cosmic rays at energies of up to ∼100 TeV, though the supporting evidence is indirect (Blasi, 2013). The standard theoretical framework for this idea is a process known as diffusive shock acceleration (Bell, 2014), but numerous more exotic scenarios have been proposed to argue that select supernova remnants might achieve cosmic ray energies in excess of 1 PeV. Some such ideas require the combination of supernovae with energetic environments such as compact star clusters (e.g., Bykov *et al.*, 2015).

The question of cosmic ray origins is an unsolved mystery, especially at energies above 3 PeV (e.g., Blasi, 2013; Gabici *et al.*, 2019). The secret to obtaining definitive evidence may lie in high-energy neutrino astronomy, since cosmic ray accelerators are expected to also be neutrino sources and neutrinos are not deflected by Galactic magnetic fields (Ahlers and Halzen, 2018). High-energy neutrino detectors, such as IceCube (Gaisser and Halzen, 2014), provide data for such investigations. Statistical correlation of neutrino events with a class of known astronomical sources (such as supernova remnants) would represent a step towards solving the cosmic ray origins puzzle. On the other hand, the lack of any such correlation could also reveal information through its disagreement with theory.

1.4 Asymmetric Explosions

Modern supernova simulations (and the stellar evolution models that necessarily precede them) regrettably suffer from a wide range of uncertainties and inaccuracies. Some common problems include inaccurate convection treatment in stellar progenitors (Young *et al.*, 2005), dimensionally oversimplified modeling of inherently three-dimensional explosions (Young and Fryer, 2007), and inconsistent consideration of the effects of the explosion mechanism (Fryer *et al.*, 2008). Published nucleosynthesis results from different research groups, using different stellar evolution or supernova hydrodynamics codes, rarely agree with one another. Furthermore, simulations often assume spherically symmetric explosions, whereas remnant observations show that real core-collapse supernovae frequently have bipolar, unipolar, or other aspherical morphologies. Changes in morphology can alter thermodynamic conditions inside the explosion significantly, influencing the elemental yields in ways that are seldom considered.

Meaningful scientific progress with supernova nucleosynthesis models depends on resolution of these issues. Newer work should strive to use stellar evolution models with more accurate treatment of convection (e.g., Young *et al.*, 2003) and fully three-dimensional explosion hydrodynamics codes (e.g., Fryer *et al.*, 2006). With full three-dimensional simulations of supernovae comes the responsibility to also model realistic three-dimensional explosion asymmetries. This is doubly important for nucleosynthesis studies in particular, since the influence of asymmetries on the thermodynamic trajectories of material can alter the yields of the simulation in ways that have yet to be rigorously quantified. Greater understanding of both the causes and consequences of asymmetry could ultimately help to bring model predictions into agreement with observations.

1.5 Summary of Chapters

The chapters of this dissertation are organized as follows. Chapter 2 presents an exploration of the supernova engine via a three-dimensional simulation and its applications to ^{44}Ti observations of supernova remnant Cas A. Chapter 3 is a statistical analysis considering both supernova remnants and open clusters as Galactic candidate sources of high-energy neutrinos. Chapter 4 is a collection of asymmetric supernova simulations comparing their yields and the effects of the explosion geometry on thermodynamic trajectories of the stellar material. Chapter 5 closes the dissertation and presents the broad conclusions of my work.

Chapter 2

TITANIUM AND IRON IN THE CASSIOPEIA A SUPERNOVA REMNANT

2.1 Abstract

Mixing above the proto-neutron star is believed to play an important role in the supernova engine, and this mixing results in a supernova explosion with asymmetries. Elements produced in the innermost ejecta, e.g., ^{56}Ni and ^{44}Ti, provide a clean probe of this engine. The production of ^{44}Ti is particularly sensitive to the exact production pathway and, by understanding the available pathways, we can use ^{44}Ti to probe the supernova engine. Using thermodynamic trajectories from a three-dimensional supernova explosion model, we review the production of these elements and the structures expected to form under the "convective-engine" paradigm behind supernovae. We compare our results to recent X-ray and γ-ray observations of the Cassiopeia A supernova remnant.

2.2 Introduction

Guided by the observed mixing of ^{56}Ni in SN 1987A, astronomers began to develop a model for the core-collapse supernova (CCSN) engine where the efficiency of potential energy release in the collapse is increased through hydrodynamic instabilities above the proto-neutron star (Herant and Benz, 1992). The first successful explosion produced by modeling the collapse and engine of a massive star in multiple dimensions demonstrated that this physics was key to the explosion process (Herant *et al.*, 1994). Twenty-five years later, although the nature of the hydrodynamic instabilities remains a matter of debate, this engine has now become the standard supernova engine (e.g., Fryer and Young, 2007; Takiwaki *et al.*, 2014; Melson *et al.*, 2015; Burrows *et al.*, 2018). The basic model argues that after the collapse of a massive star, the core reaches nuclear densities and bounces, driving a shock that soon stalls. The region between the dense proto-neutron star and the stalled shock is susceptible to a number of convective instabilities. Convection distributes the energy from the proto-neutron star's surface outwards to the edge of the stalled shock, and it also reduces the mass at the stalled shock by transporting material that was piling up at the shock inwards to the proto-neutron star. Both of these factors increase the probability of a successful explosion occurring.

This supernova-engine paradigm has undergone a continuous series of verification and validation tests (including a broad range of code-comparison studies such as those listed in the previous paragraph) comparing model predictions to observations. For example, driven by the need for explosion asymmetries in models of SN 1987A, this engine model argued for asymmetries that could develop at low modes, possibly producing the "kicks" seen in pulsars (Herant, 1995; Scheck *et al.*, 2006). By noting that the explosion energy for this mechanism is set to the energy stored in the convective region prior to the launch of the shock, engine theorists were able to explain the fact that although the collapse releases $\sim 10^{53}$ erg, typical explosion energies are $\sim 10^{51}$ erg (Fryer, 1999). At a time when supernova observations predicted that only very massive stars would explode (Hamuy and Pinto, 2002), this engine argued that only stars with masses (neglecting mass loss) below ~ 23 $M_\odot$ would explode (Fryer, 1999)[1]. Likewise, in a time when the remnant mass distribution was believed to be a set of delta functions (Thorsett and Chakrabarty, 1999), this model predicted a range of neutron star and black hole remnant masses (Fryer and Kalogera, 2001). Both of these predictions were ultimately confirmed by later observations (Lattimer, 2012).

---

[1] Not surprisingly, mass loss can alter this effect and allow more massive stars to explode.

With the acceptance of this paradigm, observations could then be turned to better understand the details of the model. For example, although the convective engine does not predict a mass gap in the mass distribution of compact remnants, the existence of a mass gap can place constraints on the uncertainties in the engine (Fryer *et al.*, 2012). The nucleosynthetic yields also place strong constraints on the supernova engine. Unfortunately, most elements can only be observed if they are excited by the reverse shock, and any abundance study must incorporate the uncertainties in estimating the distributions and masses of the different elements in the ejecta. The reverse shock is produced as the supernova shock decelerates in the circumstellar medium, and it is often difficult to distinguish asymmetries in the explosion from asymmetries in the circumstellar medium in these observations. The exception to these limitations is the measurement of ^{44}Ti. The decay half-life of ^{44}Ti is ~ 60 yr, and hence is ideally suited for studies of 100–1000 yr old remnants. Photons emitted in the radioactive decay of ^{44}Ti and its daughter products are a direct measurement of the ^{44}Ti yield, unaffected by uncertain shock dynamics and asymmetries in the circumstellar medium. In addition, ^{44}Ti is produced in the innermost ejecta, providing a direct probe of the central core-collapse engine. NuSTAR observations of the ^{44}Ti distribution in the Cassiopeia A supernova remnant provided the first glimpse of the asymmetries in the supernova engine, as well as a direct confirmation of the low-mode asymmetries predicted by the convective supernova engine (Grefenstette *et al.*, 2014, 2017).

Discussion of ^{44}Ti and ^{56}Ni production in the inner ejecta of supernovae dates back just as far as investigations of the convective supernova engine (e.g. Thielemann *et al.*, 1990; Hoffman *et al.*, 1995; Diehl and Timmes, 1998). The two topics are nearly inseparable given the importance of ^{44}Ti and Fe as observational probes of deep interior supernova conditions. Thielemann *et al.* (1996) pointed out that the production of these isotopes depends on radiation entropy and on the strength of the α-rich freeze-out. (Hoffman *et al.*, 1999) discussed equilibrium features and sensitivity to reaction rates. More recently, Magkotsios *et al.* (2010) presented a detailed grid analysis of ^{44}Ti and ^{56}Ni production in CCSNe. The bulk of their analysis studied simple trajectories fitting power laws and exponential decays. A pair of two-dimensional explosions were briefly examined but not analyzed in detail.

Cassiopeia A (Cas A) is one of the best-studied supernova remnants, with a broad set of constraints on the progenitor at the time of collapse as well as the explosion energetics and asymmetries (Young *et al.*, 2006). The existence of nitrogen knots in the supernova remnant (Fesen and Becker, 1991) argues that the stellar material must have undergone CNO processing and the helium envelope should have been exposed (Arnett, 1996). This argues that the explosion was a type-Ib/IIb supernova, a fact confirmed by spectral and light-curve observations of the light-echo (Krause *et al.*, 2008). The ejecta mass is more difficult to predict, and is based both on kinematic properties and emission measures across a wide range of wavelengths. These models predict ejecta masses between 2 and 4 $M_\odot$. If the total mass of the star at explosion was the remnant mass ($\sim$ 1.2–2 $M_\odot$) plus the ejecta mass, then the progenitor helium star had a mass of $\sim$ 3.5–6 $M_\odot$. This corresponds to an initial progenitor mass of roughly 13–23 $M_\odot$, with the majority of the hydrogen envelope being stripped off by a binary interaction. These constraints also place limits on the explosion energy (Chevalier and Oishi, 2003).

Current studies of the nucleosynthetic yields of Cas A have only scratched the surface of what we might learn from this data. For example, Wongwathanarat *et al.* (2017) published yields for a model resembling Cas A, but did not include a detailed description of thermodynamic trajectories. They also assumed a single value of Y_e based on the progenitor composition outside a cutoff radius in their preferred model, which was chosen to better match the Cas A remnant. Neutrino processing may affect the final yields, but assuming a single value of Y_e is not realistic (Saez *et al.*, 2018; Fujimoto and Nagakura, 2019). Couch *et al.* (2015) simulated the last few minutes of Si-shell burning in 3D before modeling the collapse and explosion, which they also ran in 3D with a single octant and a network of 21 isotopes. Their star was evolved to Si buring using MESA, which suffers from incorrect treatment of mixing (Arnett and Moravveji, 2017; Arnett and Meakin, 2011; Arnett *et al.*, 2009). Harris *et al.* (2017) ran an explosion engine in 2D out to $t \sim 1$ s. They use the Woosley and Heger (2007) progenitor models evolved using KEPLER, which also lacks an accurate treatment of convection. Eichler *et al.* (2018) ran two simulations of different masses and examined how the varying Y_e values changed the yields of heaver nuclei well beyond the iron group, but their 2D models suffer from dimensionality problems with convection in the explosion.

In this project, we compare the spatial and velocity distributions of the ^{44}Ti in an explosion based on the convective engine to the observed distributions from NuSTAR and XMM. We produce a bimodal distribution in the Fe/^{44}Ti ratio, which we argue could be a common feature of supernova remnants. In addition, we find that deceleration of the shock can re-heat material significantly enough to alter thermodynamic trajectories and the resulting yields. The methods used in these calculations are described in section 2.3, with the ^{44}Ti distributions presented in section 2.4. The ^{44}Ti yields relative to iron-peak elements (also synthesized in the innermost ejecta) provide constraining probes of the strength of the engine, but this requires understanding the detailed thermodynamic trajectories that are produced in these explosions, which are also discussed in section 2.4. We conclude with a brief discussion of the other yields of Cas A.

2.3 Methods

2.3.1 Stellar Models Using Tycho

The progenitor star was simulated using the stellar evolution code Tycho (Young and Arnett, 2005). Tycho is a one-dimensional stellar evolution code with a hydrodynamic formulation of the stellar evolution equations. It uses OPAL and revised low temperature opacities (Iglesias and Rogers, 1996; Alexander and Ferguson, 1994a; Rogers and Nayfonov, 2002; Ferguson *et al.*, 2005; Serenelli *et al.*, 2009), a combined OPAL and Timmes equation of state (HELMHOLTZ) (Timmes and Arnett, 1999; Rogers and Nayfonov, 2002), gravitational settling (diffusion) (Thoul *et al.*, 1994), general relativistic gravity, time lapse, curvature, automatic rezoning, and an adaptable nuclear reaction network with a sparse solver. A 177-element network terminating at ^{74}Ge is used throughout the evolution. The network uses the latest REACLIB rates (Rauscher *et al.*, 2000; Angulo *et al.*, 1999; Iliadis *et al.*, 2001; Wiescher *et al.*, 2006), weak rates from Langanke and Martínez-Pinedo (2000), and screening from Graboske *et al.* (1973). Neutrino cooling from plasma processes and the Urca process is included.

Mass loss uses a choice of updated versions of the prescriptions of (Kudritzki *et al.*, 1989) or prescriptions based on Vink *et al.* (2001); Mokiem *et al.* (2007) for OB mass loss, Bloecker (1995) for red supergiant mass loss, and Lamers and Nugis (2002) for WR phases.

Tycho incorporates a description of turbulent convection projected down to 1D secularly evolving average behavior (Arnett and Moravveji, 2017), which is based on three-dimensional, well-resolved simulations of convection sandwiched between stable layers, which were analyzed in detail using a Reynolds decomposition into average and fluctuating quantities (Meakin and Arnett, 2007; Arnett *et al.*, 2009, 2010; Arnett and Meakin, 2011; Arnett and Moravveji, 2017). Unlike mixing-length theory, it has no free convective parameters to adjust. The inclusion of these processes, which approximate the integrated effect of dynamic stability criteria for convection, entrainment at convective boundaries, and wave-driven mixing, results in significantly larger turbulently mixed regions. Therefore the extent of material processed by particular core or shell burning phases is higher, and the stellar core at a given stage is more massive and denser.

The progenitor used here is a non-rotating 15 $M_\odot$ star with solar composition from Lodders (2010). The mass of the final model used as the initial condition for the supernova calculation was 13.15 $M_\odot$. This model does not include stripping by a binary companion. The retention of a hydrogen envelope would affect the late time behavior of the explosion significantly (Ellinger *et al.*, 2013, i.e.), but the production of ^{44}Ti and ^{56}Ni depends only on the structure of the deep interior of the star. Relatively early mass loss would change the structure of the progenitor star's core, but the best candidate for the progenitor of Cas A is a binary with late-time envelope ejection (Young *et al.*, 2006). Comparing the progenitor model from this calculation with a stripped model of similar mass, the radial profiles inside the H envelope revealed the density and temperature differing by less than a factor of 10. We note that massive star models in the literature suffer from incorrect mixing physics (Meakin and Arnett, 2007; Arnett *et al.*, 2009, 2010; Arnett and Meakin, 2011; Arnett and Moravveji, 2017), which leads to significantly greater discrepancies. At minimum, this difference makes our model no less relevant than models presented in other works. Evolution was terminated when negative velocities existed throughout the core and the central temperature rose to $T > 5 \times 10^9$ K. Figure 2.1 shows the mass fraction of isotopes plotted against mass coordinate (enclosed mass) for the final model.

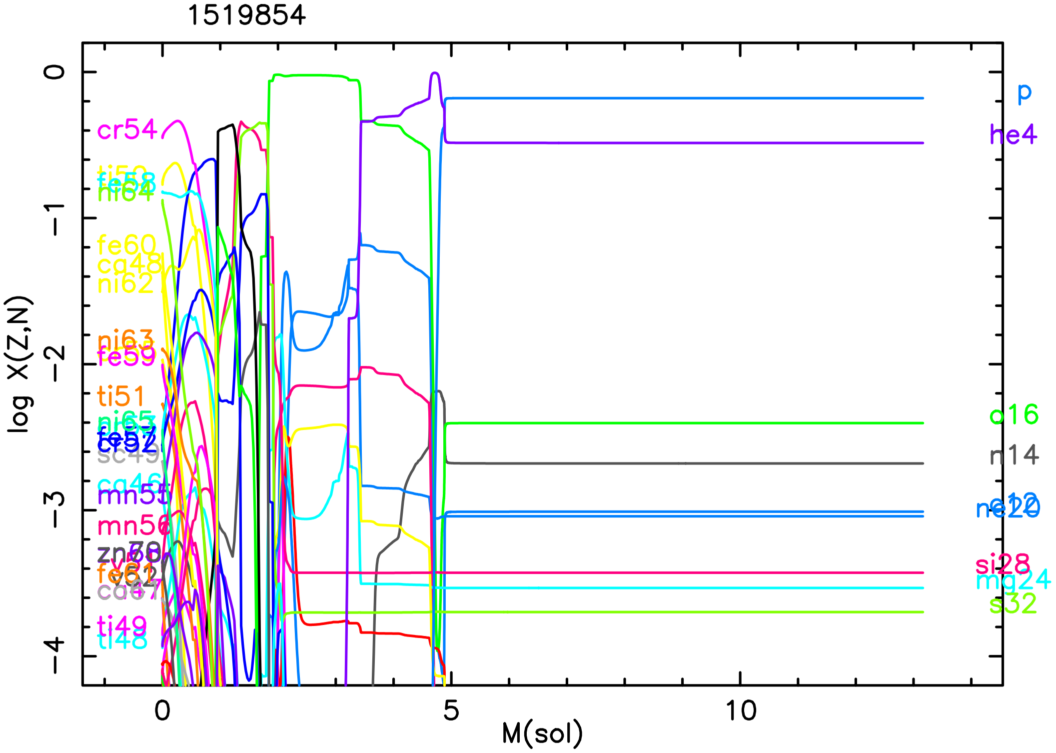

Figure 2.1: Mass fractions for isotopes plotted against mass coordinate (enclosed mass) for the final progenitor star model.

2.3.2 Collapse and Explosion Models

To model the stellar collapse and ensuing explosion, we use a one-dimensional Lagrangian code to follow the collapse through core bounce. This code includes three-flavor neutrino transport using a flux-limited diffusion calculation and a coupled set of equations of state to model the wide range of densities in the collapse phase (see Herant *et al.*, 1994; Fryer, 1999, for details). It includes a 14-element nuclear network (Benz *et al.*, 1989) to follow the energy generation.

The shock is then revived by adding an energy injection following the parameterized method of Fryer *et al.* (2018). In this model, roughly 5×10^{51} erg was deposited into the inner 0.02 $M_\odot$ in the first 150 ms. Some of this energy is lost through neutrino emission and the total explosion energy at late times for this model is 1.5×10^{51} erg. This explosion is then mapped into our three-dimensional calculations, using 1 million SPH particles. The mapping took place when the supernova shock had moved out of the iron core and propagated into the Si-S rich shell at $t < 1$ s. We note that our 1D methods employed for modeling the collapse, core bounce, and initial explosion do not capture the full physics of the central engine (for a discussion, see Fryer *et al.*, 2018), and this is a source of uncertainty in our yields calculations. The details of the engine change the shock trajectories, and neutrino chemistry can change Y_e values (Saez *et al.*, 2018; Fujimoto and Nagakura, 2019). The nature of the shock affects mostly the yields after the shock falls below NSE (before it falls out of NSE, the yields are set by the equilibrium values, not the time-dependent evolution). Our model captures one instance of the range of asymmetric trajectories, and it should be noted that no model at this time is sufficiently accurate to dictate exactly the properties of the asymmetries (Janka *et al.*, 2016). In addition, any model that does not include convection-driven asymmetries from the progenitor star cannot properly capture the asymmetries (Arnett *et al.*, 2015). The 3D explosion model used here also displays stochastic asymmetries, implying that any manner of convective asymmetry could generate similar results. If this behavior is universal, it could have important implications. These points taken together indicate that nucleosynthetic patterns arising from convection-like behavior are robust, regardless of the driver. As discussed below, this increases the utility of NSE nucleosynthesis, particularly of ^{44}Ti and ^{56}Ni, as diagnostics of the conditions in the progenitor star.

The latter point, the Y_e values, could alter our results as well (see, e.g., Magkotsios *et al.*, 2010). Although more detailed models have addressed neutrino interactions and the evolution of Y_e, the neutrino physics is not yet sufficiently accurate to model this correctly (Saez *et al.*, 2018). In light of this, any nucelosynthetic calculation under these conditions is subject to uncertainty. In order to assess the effect of these uncertainties on the results presented here, we carried out a series of nucleosynthesis calculations using thermodynamic trajectories from the explosion model with a range of values for Y_e. The vast majority of material that reached sufficiently high temperatures for production of ^{44}Ti and ^{56}Ni saw yield changes of no more than 3–4% for Y_e values from 0.495 to 0.499. This is a larger range of Y_e than we would expect from the material ejected in this particular explosion, so these results provide a conservative bound on our uncertainties. As discussed later in Section 2.4, many of our more important results are general enough to be robust to small changes in the nucleosynthetic conditions, so we expect these uncertainties to not qualitatively alter our conclusions.

The 3D simulation used the SNSPH smoothed particle hydrodynamics (SPH) code (Fryer *et al.*, 2006) to follow the long-term evolution of the supernova explosion and remnant. This code has been extensively used to follow the ejecta of supernovae (Hungerford *et al.*, 2003, 2005; Young *et al.*, 2009; Ellinger *et al.*, 2012, 2013; Wong *et al.*, 2014), taking advantage of the adaptive time steps and variable particle scale lengths in the method. A central gravity source with absorbing boundary was included to simulate a compact central object (CCO) with an initial mass of 1.35 $M_\odot$ and radius of 10^{-4} $R_\odot$. Total mass, linear momentum, and angular momentum accreted onto the central object were tracked.

The SNSPH code makes use of a limited nuclear reaction network of 20 isotopes to expedite the energy calculations for the hydrodynamics. The network terminates at ^{56}Ni and neutron excess is directed to ^{54}Fe. The network runs in parallel to the hydrodynamics calculations, and features its own time step subcycling algorithm in order to not slow down the hydrodynamics. Changes in energy and composition are fed back into the SPH calculation at each (SPH) time step. It accurately models the energy production during explosive burning to within 20%.

2.3.3 Detailed Nucleosynthetic Yields

In order to obtain more accurate nucleosynthetic data, the thermodynamic trajectories of the particles were post-processed using the Burnf code (Young and Fryer, 2007). Burnf is a flexible network (e.g., choice of isotopes, etc.) that employs the same architecture and microphysics as Tycho. This work is focused on comparisons with species readily observable in supernova remnants. With this aim, it was possible to economize on processor time by using a moderately sized network. Calculations here used a 524-isotope network complete up to ^{99}Tc, which provides accurate yields through the weak s-process. Reverse rates are calculated from detailed balance and allow a smooth transition to a nuclear statistical equilibrium (NSE) solver at temperatures $T > 10^{10}$ K. Neutrino cooling from plasma processes and the Urca process is calculated. For this work, Burnf chooses an appropriate time step based on the rate of change of abundances and performs a log-linear interpolation in the thermodynamic trajectory of each zone in the explosion calculation. The initial abundances are those of the 177 nuclei in the initial stellar model. Only particles that reached temperatures $T > 2 \times 10^8$ K were post-processed. The individual particle yields from post-processing with Burnf were recombined with the particle temporal and spatial information for analysis and visualization. Note that Harris *et al.* (2017) discuss some of the inherent issues and uncertainties involved in postprocessing abundances.

In addition to determining isotopic abundances for each individual SPH particle, we also recorded the peak temperature experienced by each particle over the length of the simulation and its density at the time of peak temperature. The peak temperature and associated density are diagnostics of nucleosynthetic conditions in supernova explosions; they influence nuclear reaction rates, especially for the products of α-rich freeze-outs, where rapidly changing conditions terminate nuclear reactions before NSE can be reached. Production of ^{44}Ti and ^{56}Ni, and their resulting ratio can be very sensitive to peak temperatures, peak densities, and lepton fraction in the explosion (Magkotsios *et al.*, 2010), so we expect this ratio to be spatially correlated with those conditions. High-energy emission lines from the decay of ^{44}Ti can be detected in young remnants. Under the assumption that most Fe-rich material originating in the interior of the remnant are dominated by ^{56}Fe from ^{56}Ni decay, the geometry of ^{56}Ni production and abundance relative to ^{44}Ti can be inferred (e.g., Grefenstette *et al.*, 2017).

2.4 ^{44}Ti and ^{56}Ni distribution

The isotope ^{44}Ti is produced in the innermost ejecta of a supernova and provides an ideal probe of the convective engine behind CCSNe. Unlike ^{56}Ni, the production of ^{44}Ti, and even the path by which it is produced, depends on the exact conditions of the explosion. Magkotsios *et al.* (2010) identified a number of pathways for ^{44}Ti that produce a wide variation in the ratio of ^{44}Ti to ^{56}Ni, including a "QSE-leakage chasm" where burning transitions from one QSE cluster to two, resulting in a mass fraction of ^{44}Ti that is substantially lower than would be the case for slightly higher or lower peak temperatures. Production of ^{56}Ni is relatively insensitive to small changes in thermodynamic conditions. The strong sensitivity in the ^{44}Ti production coupled to the much less sensitive ^{56}Ni production make the ratio of these yields a strong probe of the details of the explosion mechanism. In this section, we explore the dependency of the yields and, in particular, the ratio of ^{44}Ti to ^{56}Ni, on our specific explosion trajectories.

The nature of the convective engine is that it produces strong explosions along some directions (or lobes) with weaker explosions in between. The α-rich freeze-out

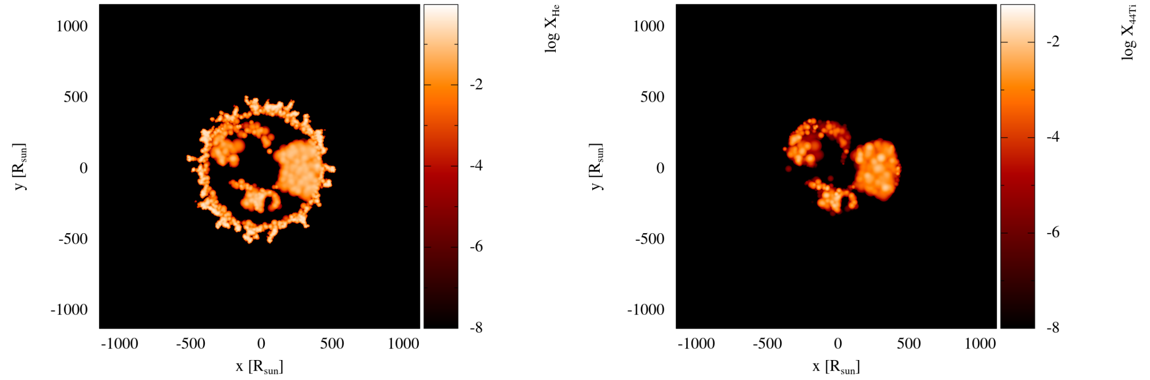

Figure 2.2: Abundance of ^{4}He (left) and ^{44}Ti (right) in an xy cross-section of the simulation. Much of the ^{44}Ti production corresponds to α-rich regions in the ejecta. Additional ^{4}He is present in the Rayleigh-Taylor fingers formed by the reverse shock from the H-He interface at the base of the envelope traveling through products of partial He burning.

region that Magkotsios *et al.* (2010) argued would be the most efficient at producing ^{44}Ti is tied to the strong explosive lobes and can be identified by regions where the ^{4}He abundance fraction is also high. Figure 2.2 (left) shows the ^{4}He abundance in xy cross-section of our three-dimensional model. The corresponding ^{44}Ti distribution, as shown in figure 2.2 (right), traces this α-rich region. Regions without a large fraction of α particles (^{4}He nuclei) did not produce much ^{44}Ti. The isotope ^{56}Ni is produced in this same region, but the ^{56}Ni/^{44}Ti ratio varies considerably. Figures 2.3 and 2.4 are histograms of all particle Fe/^{44}Ti values for the simulation for particles having ^{44}Ti mass fraction $X(^{44}\mathrm{Ti}) > 10^{-6}$. In figure 2.3, the particles are each weighted by their total mass. In figure 2.4, the particles are instead weighted by their total *iron* mass (including all Fe isotopes and ^{56}Ni, since ^{56}Ni eventually decays to ^{56}Fe). Each histogram shows two distinct populations of particles: those having Fe/^{44}Ti ratios of $\sim 10^{2.5}$ and those having Fe/^{44}Ti ratios of $\sim 10^{3.9}$. There are also minor peaks visible with Fe/^{44}Ti ratios near $10^{1.0}$ and $10^{1.8}$.

To understand the variations in the Fe/^{44}Ti ratio better, we must explore how

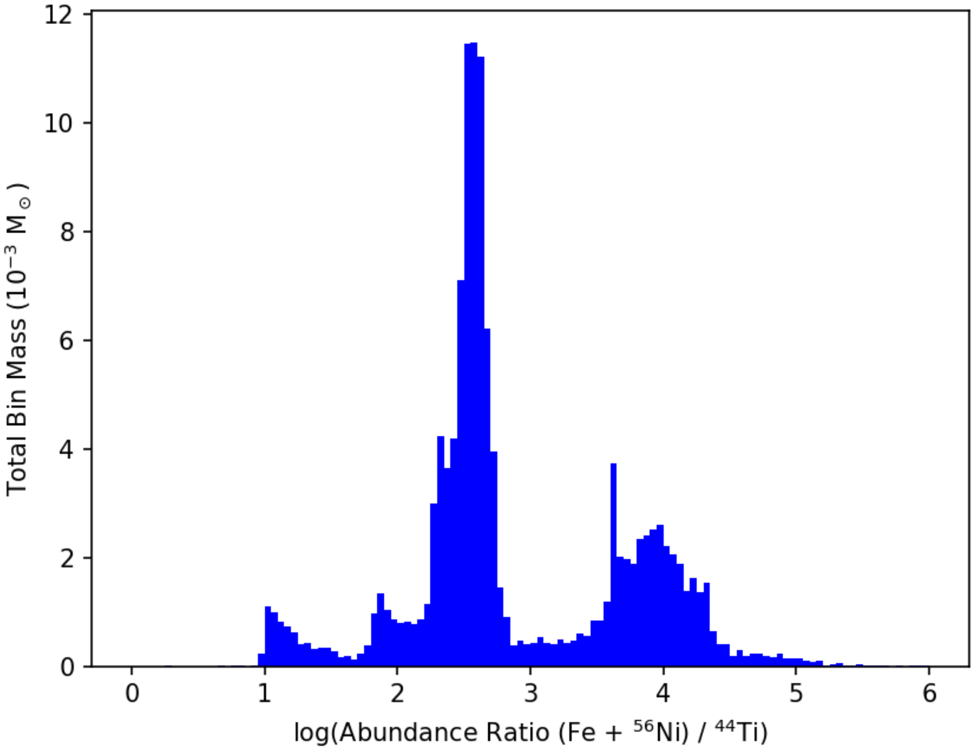

Figure 2.3: Histogram of particle Fe/^{44}Ti ratios for the simulation. Particles are weighted by their total masses, so each bin displays the sum of the masses of all particles it contains.

the temperature and density evolution of different ejecta can influence the final ^{44}Ti yield. Magkotsios *et al.* (2010) found that the peak temperature and density (at time of peak temperature) of material ejected from a supernova dictate the final ^{44}Ti and ^{56}Ni yields. While Magkotsios *et al.* (2010) studied a wide range of peak temperature/density pairs, we focus on the pairs encountered for the specific trajectories in our simulation. Figure 2.5 shows the ^{44}Ti abundance of our SPH particles as a function of the peak explosion conditions. This figure was produced by binning all the simulation particles in two dimensions by their peak temperature and associated density during the run. The color displayed in each bin indicates the total ^{44}Ti mass

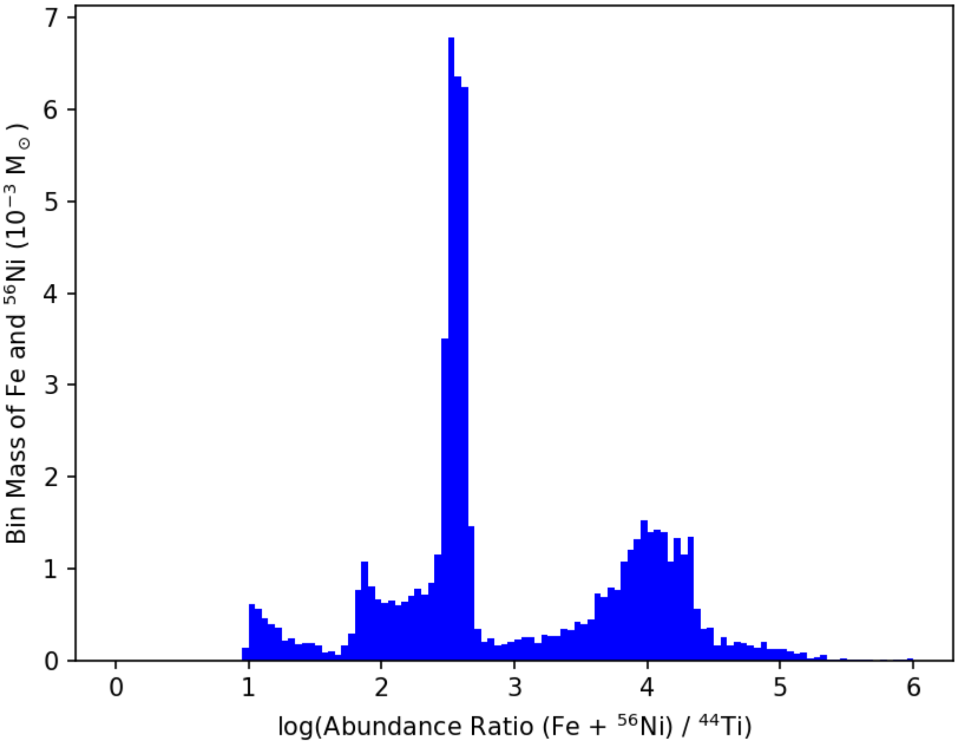

Figure 2.4: Alternate histogram of particle Fe/^{44}Ti ratios for the simulation. Particles are weighted by their total *iron* masses, so each bin displays the sum of the masses of all Fe isotopes plus ^{56}Ni from all particles in the bin.

fraction $X_{\mathrm{bin}}(^{44}\mathrm{Ti})$ of particles in the bin, which is given by

$$X_{\mathrm{bin}}(^{44}\mathrm{Ti}) = \frac{\sum_{i \in \mathrm{bin}} m_i X_i(^{44}\mathrm{Ti})}{\sum_{i \in \mathrm{bin}} m_i}, \tag{2.1}$$

where X_i denotes the mass fraction of a particular isotope or element in particle i, m_i is the total mass of particle i, and summation over $i \in$ bin means summing for all particles i in the bin. Figure 2.5 is scaled and colored in the style of Magkotsios *et al.* (2010) for ease of comparison with their results. The corresponding plot for ^{56}Ni production is shown in figure 2.6. Comparing these plots gives a first look at the conditions that produce the lowest and highest Fe/^{44}Tiratios. The hotter trajectories are the most efficient at producing ^{56}Ni and ^{44}Ti.

Figure 2.7 is similar to figures 2.5 and 2.6, but instead of displaying one abundance

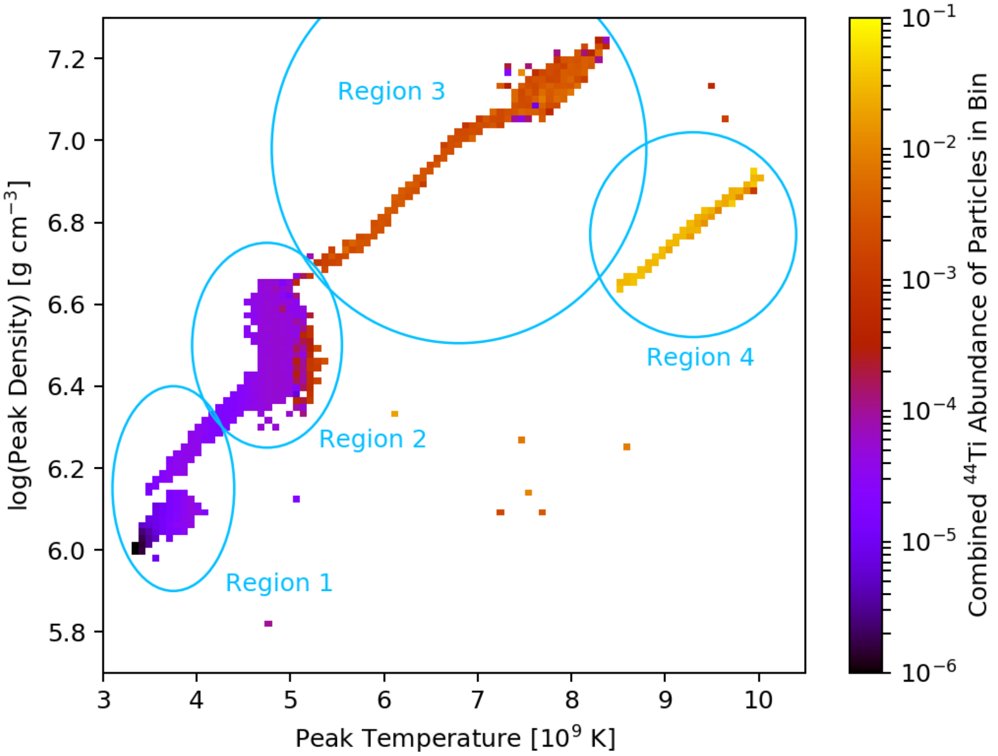

Figure 2.5: Two-dimensional histogram of the simulation particles by peak temperature and associated density during the run. Each particle is weighted by its ^{44}Ti mass divided by the total mass of all particles in the bin, so colors indicate the mass-averaged ^{44}Ti abundance of all contained particles. This figure is produced in the style of Magkotsios *et al.* (2010) for ease of comparison to their work.

in each bin, the colors now indicate the aggregate mass-weighted Fe/^{44}Ti ratio of all particles in the bin, which is given by

$$\frac{X_{\text{bin}}(\text{Fe}) + X_{\text{bin}}(^{56}\text{Ni})}{X_{\text{bin}}(^{44}\text{Ti})} = \frac{\sum_{i\in\text{bin}} m_i \left[X_i(\text{Fe}) + X_i(^{56}\text{Ni})\right]}{\sum_{i\in\text{bin}} m_i X_i(^{44}\text{Ti})}. \tag{2.2}$$

This series of figures shows the temperature and density conditions under which ^{44}Ti and ^{56}Ni production result in the bimodal ratios that appear to be characteristic of both Cas A and our simulation. Material produced at high temperatures in the α-rich freezeout region has a very low Fe/^{44}Ti ratio, of order a few hundred. This transitions rapidly to Fe/^{44}Ti of several thousand or even several times 10^4 at lower temperatures.

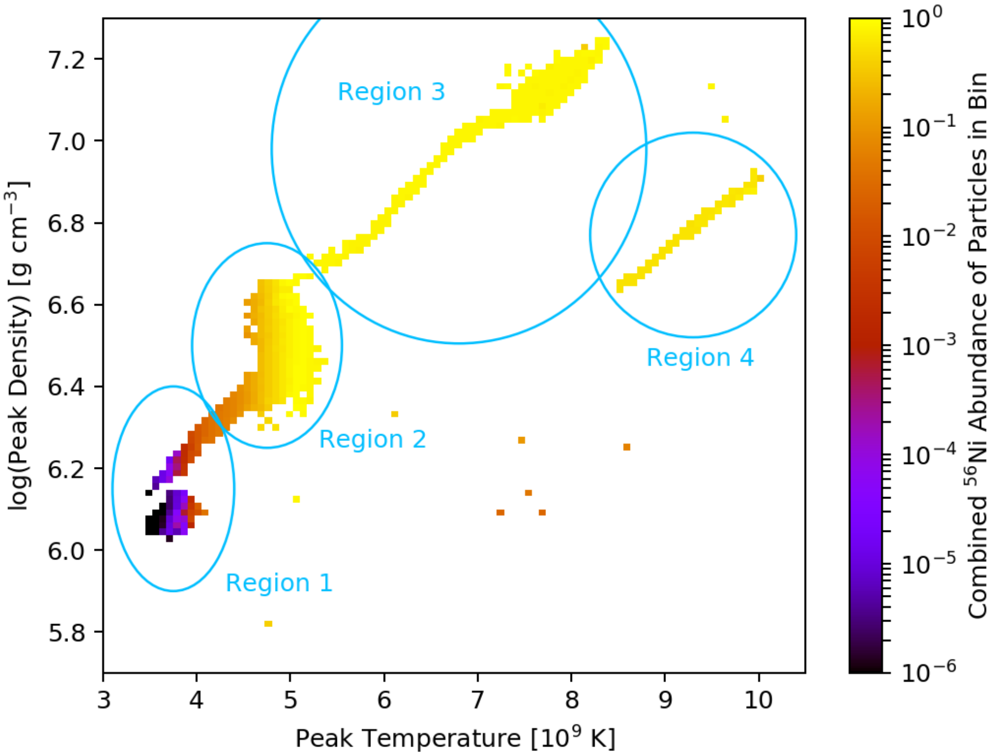

Figure 2.6: Same as figure 2.5, but colors indicate the combined ^{56}Ni abundance of each bin.

At even lower temperatures, there is another rapid transition to a small population of particles with Fe/^{44}Ti of several hundred. In this regime, ^{44}Ti and ^{56}Ni are produced in similar amounts at mass fractions of order 10^{-5} by explosive silicon burning. The Fe/^{44}Ti ratio is still several hundred due to the presence of iron isotopes remaining from the progenitor star's initial composition.

Figure 2.8 shows two-dimensional histograms of Fe/^{44}Ti ratio plotted against peak temperature and peak radiation entropy, where the total mass in each bin is indicated by the color scales. Peak radiation entropy is defined as the radiation entropy at the time of peak temperature, which is related to the peak temperature and density via

$$S_{\mathrm{rad}}(T_{\mathrm{peak}}) = \frac{T_{\mathrm{peak}}^3}{\rho(T_{\mathrm{peak}})}, \tag{2.3}$$

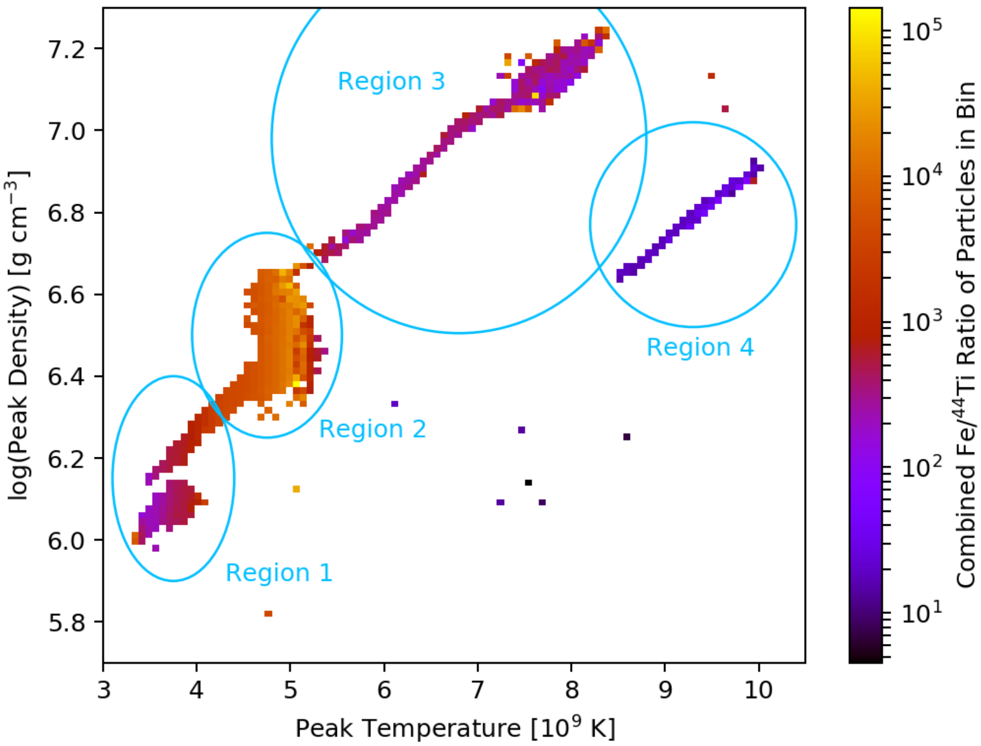

Figure 2.7: Two-dimensional histogram similar to figures 2.5 and 2.6, but with each bin color indicating the aggregate mass-weighted Fe/^{44}Ti ratio (including ^{56}Ni) of all particles in the bin.

where $T_{\rm peak}$ is the peak temperature and $\rho(T_{\rm peak})$ is the associated density. It can be seen that region 4, which has very low typical values of Fe/^{44}Ti, represents a small amount of overall mass relative to the other regions. The regions are well separated in peak temperature space, but the separation is much less clear in radiation entropy, since there is considerable degeneracy in T^3/ρ pairs that result in the same value of $S_{\rm rad}$.

Employing these plots, we can now better understand the yields from this explosion. To this end, we have separated the ejecta into four regions in peak temperature/density space that are numbered 1 through 4. Table 2.1 provides precise definitions for the boundaries delimiting each region, as well as some thermodynamic

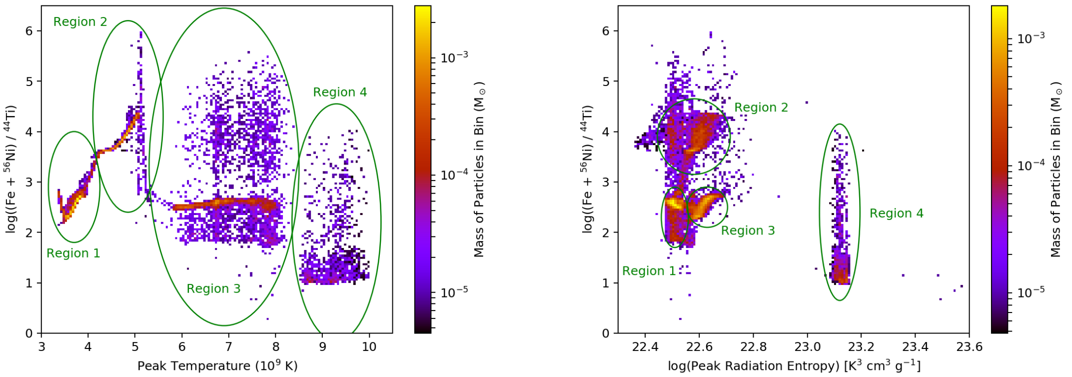

Figure 2.8: Two-dimensional histograms of Fe/^{44}Ti ratio as a function of peak temperature (left) and peak radiation entropy (right). The colors indicate the sum of the particle masses in each bin. Regions 1, 2, 3, and 4 (appearing from left to right) are well-separated in peak temperature.

quantities for the mean thermodynamic trajectories of particles in each. Magkotsios *et al.* (2010) identified multiple burning regions, and the yields from our first two regions can be understood by comparing to these burning regions.

Region 1 includes the outermost ejecta, the coldest material that still produces ^{44}Ti. The conditions in this ejecta correspond to the “Si-rich” zone (incomplete burning) identified by Magkotsios *et al.* (2010) to the left of the Ti-depleted chasm. Nuclear burning in this region produces and destroys ^{44}Ti through a variety of pathways and is sensitive to many nuclear reactions.

Region 2 is slightly hotter and corresponds to material just to the right of the QSE leakage chasm. The burning is more complete and the ^{56}Ni production rises dramatically, but it is still sensitive to some rates and the exact conditions of the ejecta. Magkotsios *et al.* (2010) found that, for the same temperature, the ^{44}Ti production is lower at higher densities (as it approaches the QSE leakage chasm) and peaks at slightly lower densities than those found in our model. In this way, the ^{44}Ti abundance is sensitive to the progenitor: the higher the progenitor’s mass, the higher the density in the trajectories producing a lower ^{44}Ti yield in this region.

Table 2.1: Thermodynamic properties for the mean trajectories of each region

Region Number	T_{peak} Range	$\log \rho(T_{\mathrm{peak}})$ Range	T_{peak} Mean	$\log \rho(T_{\mathrm{peak}})$ Mean	$\log S_{\mathrm{rad}}(T_{\mathrm{peak}})$ Mean	$\log(\mathrm{Fe}/^{44}\mathrm{Ti})$ Mean
—	(10^9 K)	[g cm^{-3}]	(10^9 K)	[g cm^{-3}]	[K^3 cm^3 g^{-1}]	—
1	(3.3, 4.2)	(5.9, 6.4)	3.65	6.08	22.61	2.58
2	(4.2, 5.3)	(6.1, 6.8)	4.77	6.45	22.59	3.92
3	(5.3, 8.4)	(6.6, 7.3)	7.04	7.03	22.51	2.82
4	(8.4, 10.1)	(6.5, 7.0)	9.20	6.77	23.12	1.57

NOTE—The second and third columns delimit the extent used in defining each region of particles.

Region 3 corresponds to α-rich nucleosynthesis produced in the energetic outflows of our asymmetric ejecta. This material is the least sensitive to uncertainties in nuclear rates.

Region 4 is characterized by very hot (above $\sim 9 \times 10^9$ K) but relatively low-density material. These conditions are very efficient at producing ^{44}Ti and this ejecta is responsible for the small amount of material appearing in figure 2.4 near $\log(\mathrm{Fe}/^{44}\mathrm{Ti}) \sim 1.0$ and 1.8. In general, our yields differ only slightly from those of Magkotsios *et al.* (2010), but we have much more efficient ^{44}Ti production in our region 4 than a peak temperature/density solution based on the models of Magkotsios *et al.* (2010). This material is the highest-entropy ejecta caused by the strongest explosion lobes. This is in the αp-rich region identified by Magkotsios *et al.* (2010). In Magkotsios *et al.* (2010), this region produced ^{44}Ti with the same efficiency as the α-rich region. In our simulations, this ejecta very efficiently produces ^{44}Ti, yielding the lowest Fe/^{44}Ti ratios.

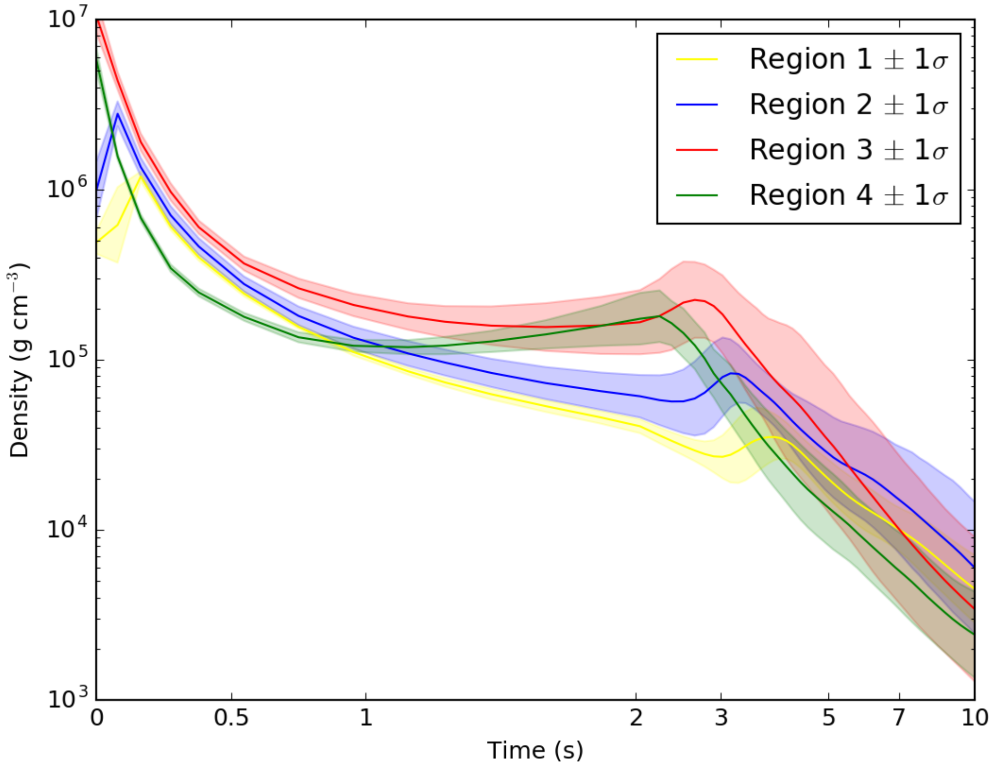

Figure 2.9: Mean density of thermodynamic trajectories for the ^{44}Ti-rich regions (region 1 in yellow, region 2 in blue, region 3 in red, and region 4 in green). Shaded areas represent 1σ spreads for particle densities. Means and standard deviations were calculated in log space. The t axis is a "symmetric log scale," which is linear near zero to more effectively show values at early times.

In the rest of this section, we will study these differences, determining that they arise from deviations of the evolution of the matter away from a simple power law or exponential trajectory. Although these simple trajectories are useful for parameter studies like those of Magkotsios *et al.* (2010), the sensitivity of ^{44}Ti production to the thermodynamic trajectory can make it difficult to produce exact yields with analytic trajectories. Figures 2.9–2.11 show the evolution of mean density, temperature, and radial velocity with time for the regions of interest. The lightly shaded regions show the 1σ spread of those quantities around the mean.

After times of 3–5 s, the shock stops accelerating and, in some cases, begins to

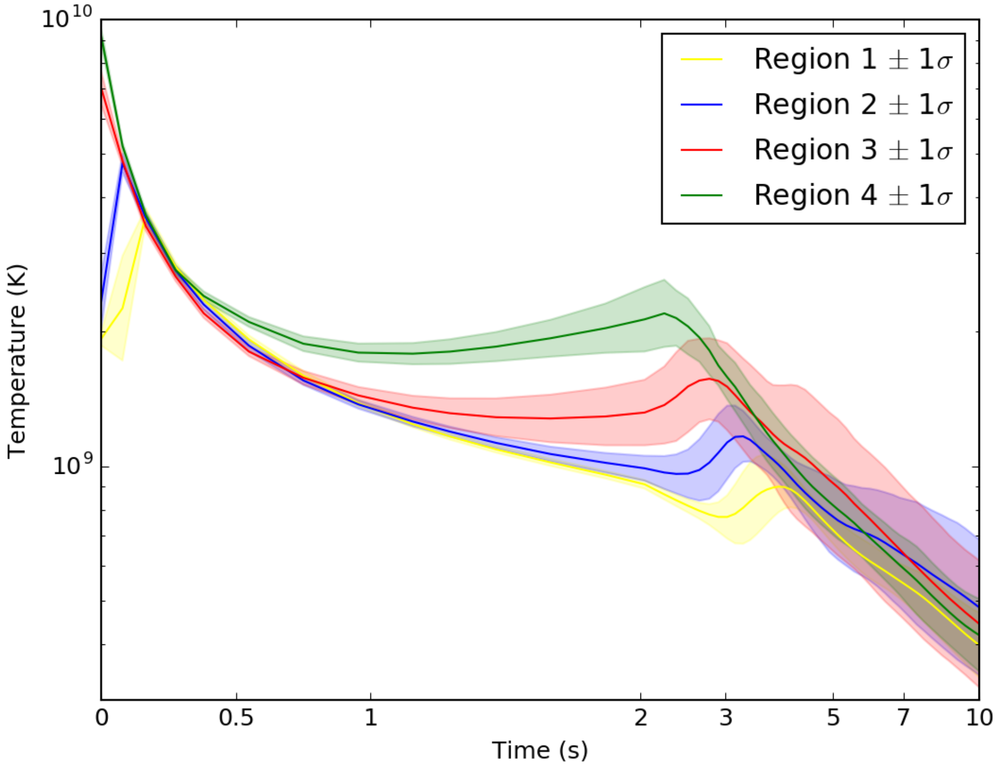

Figure 2.10: Mean temperature of thermodynamic trajectories for the ^{44}Ti-rich regions (region 1 in yellow, region 2 in blue, region 3 in red, and region 4 in green). Shaded areas represent 1σ spreads for particle temperatures. Means and standard deviations were calculated in log space. The t axis is a "symmetric log scale," which is linear near zero to more effectively show values at early times.

decelerate. Convective motions result in some material with negative radial velocities at certain points in the evolution. This causes a pileup of matter, and the densities and temperatures of the ejecta's thermal trajectories tend to increase. It is this pileup that alters the yields, causing differences when compared to expectations based on studies using power law trajectories. Especially for our hottest ejecta, the pileup pushes the temperature into a regime where nuclear burning is extremely active, and it is unsurprising that the ^{44}Ti production varies dramatically for this matter with respective to the Magkotsios *et al.* (2010) results for the same peak temperatures and densities.

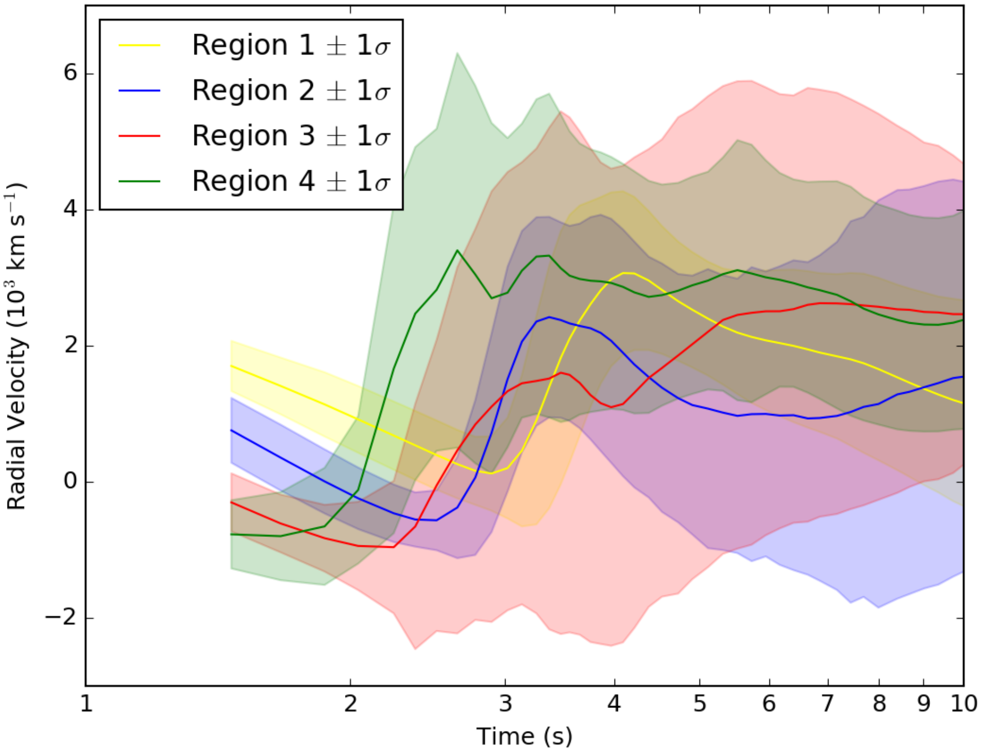

Figure 2.11: Mean radial velocity of thermodynamic trajectories for the ^{44}Ti-rich regions (region 1 in yellow, region 2 in blue, region 3 in red, and region 4 in green). Shaded areas represent 1σ spreads for particle radial velocities. Unlike figures 2.9 and 2.10, means and standard deviations in this figure are calculated normally (i.e., in linear space). Also, the t axis here uses a conventional log scale. Note: radial velocity data was unavailable for simulation times earlier than 1.25 s.

To understand the dependencies of the yields on the temperature and density evolution better, we performed nucleosynthesis calculations for trajectories corresponding to the mean trajectories in the four regions. For each of these trajectories, we start with initial mass fractions of $X(^{16}\mathrm{O}) = 0.7$, $X(^{28}\mathrm{Si}) = 0.2997$, and $X(^{56}\mathrm{Fe}) = 1.3 \times 10^{-3}$. For each region, we use two trajectories: the first based on the mean temperature/density evolution from our simulations and the second based on the best-fit power laws to each simulated trajectory. Exponential trajectories were found to be very poor fits to the evolution. The final yields of each of these models

Table 2.2: Comparison of selected final abundances for nucleosynthesis calculations using the mean trajectories from each region and the best-fit power law trajectories

	Region 1 Power Law	Region 1 Mean Traj.	Region 2 Power Law	Region 2 Mean Traj.	Region 3 Power Law	Region 3 Mean Traj.	Region 4 Power Law	Region 4 Mean Traj.
n	2.16×10^{-49}	1.14×10^{-48}	3.66×10^{-57}	1.54×10^{-55}	1.41×10^{-44}	9.52×10^{-45}	2.56×10^{-42}	3.79×10^{-43}
p	3.46×10^{-31}	6.11×10^{-34}	1.19×10^{-26}	3.04×10^{-29}	3.32×10^{-13}	2.58×10^{-15}	1.01×10^{-12}	2.40×10^{-14}
^{4}He	2.25×10^{-16}	1.20×10^{-16}	7.78×10^{-11}	7.61×10^{-11}	6.24×10^{-2}	1.09×10^{-1}	1.77×10^{-1}	2.80×10^{-1}
^{28}Si	5.38×10^{-1}	7.22×10^{-1}	1.07×10^{-1}	2.37×10^{-1}	9.22×10^{-5}	1.41×10^{-4}	3.10×10^{-4}	2.09×10^{-4}
^{44}Ti	6.54×10^{-6}	1.91×10^{-7}	4.31×10^{-5}	5.22×10^{-5}	1.08×10^{-3}	2.14×10^{-3}	3.08×10^{-3}	4.93×10^{-2}
^{56}Ni	8.46×10^{-6}	1.56×10^{-6}	6.50×10^{-1}	3.93×10^{-1}	9.00×10^{-1}	8.42×10^{-1}	7.86×10^{-1}	5.75×10^{-1}
Fe+^{56}Ni	1.13×10^{-3}	1.15×10^{-3}	6.82×10^{-1}	4.18×10^{-1}	9.01×10^{-1}	8.44×10^{-1}	7.89×10^{-1}	5.88×10^{-1}

can be found in table 2.2. The final yields can differ between our simulation trajectories and the simple power laws by more than a factor of 2. In the case of ^{44}Ti, production varies by an order of magnitude in region 4. For region 1, these differences demonstrate just how sensitive the yields are in the incomplete-burning, Si-rich phase. In regions 3 and 4, the differences are caused because the pileup alters the temperature considerably when nuclear burning is still active. Figures 2.12–2.15 show the evolution (based on the simulation trajectories) of the ^{44}Ti, ^{56}Ni, ^{28}Si, neutron, proton, and α-particle abundances both plotted against time and plotted against temperature. Figures 2.16–2.19 show this same evolution for the best-fit power law models.

Region 1 has the lowest peak temperature, and the pileup occurs when the ejecta is already quite cool. In this case, the bump in temperature has very little effect on the final yields. However, the initial rapid temperature evolution (somewhere in between an exponential decay and a power law decay) means that the burning time frame is much more abrupt in our simulations with respect to a power law fit, producing less ^{44}Ti. This causes our region 1 yields to be lower than those expected from a power

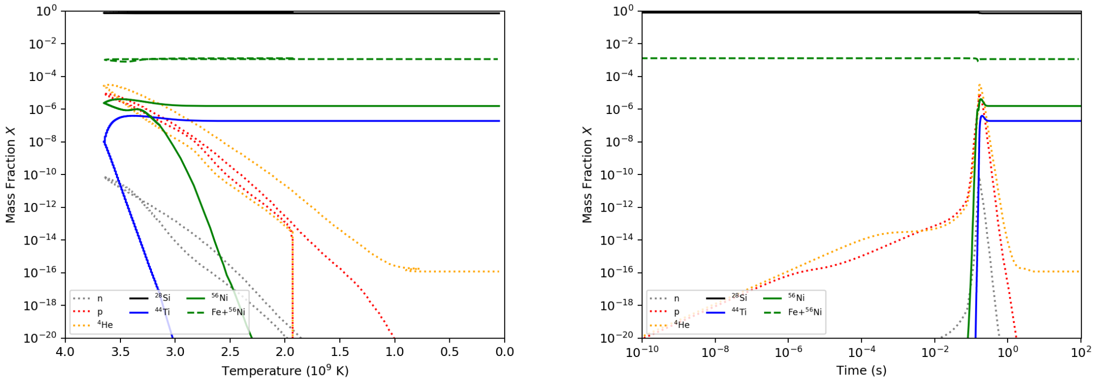

Figure 2.12: Mass fraction evolution plotted against temperature (left) and time (right) for a series of significant isotopes. Temperature and density trajectories used were the mean of the region 1 particles. (See figures 2.9 and 2.10.)

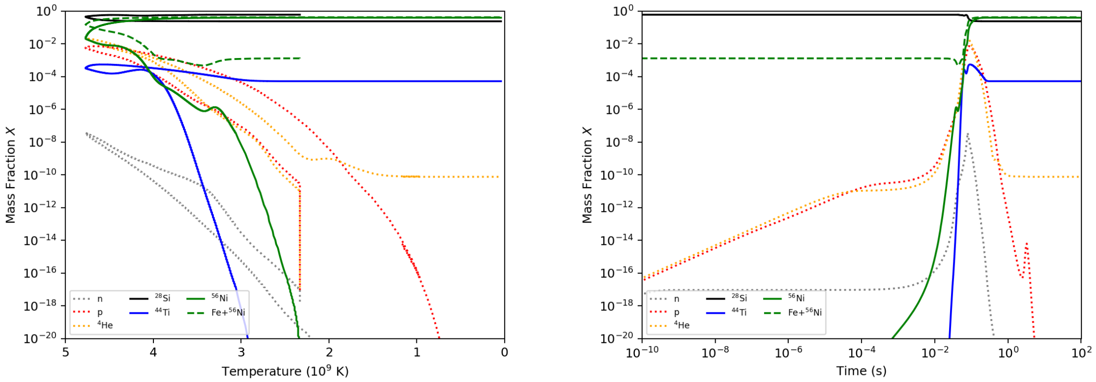

Figure 2.13: Same as Figure 2.12, but for the region 2 particles' mean trajectories.

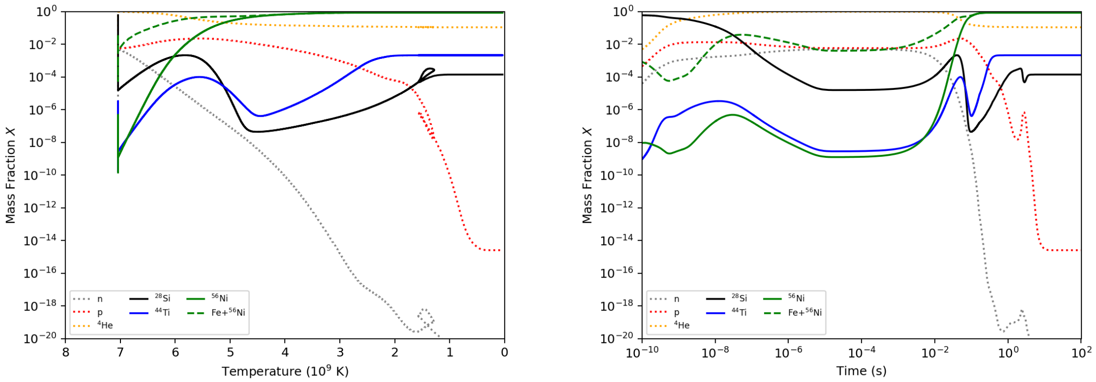

Figure 2.14: Same as Figure 2.12, but for the region 3 particles' mean trajectories.

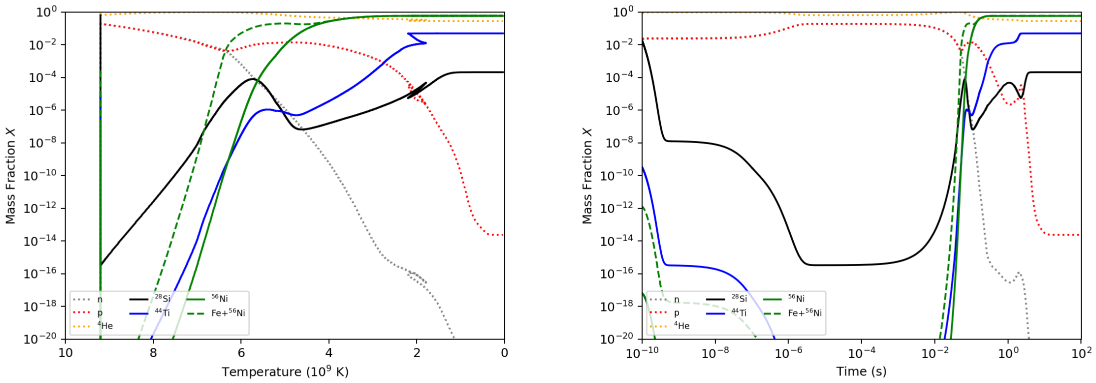

Figure 2.15: Same as Figure 2.12, but for the region 4 particles' mean trajectories.

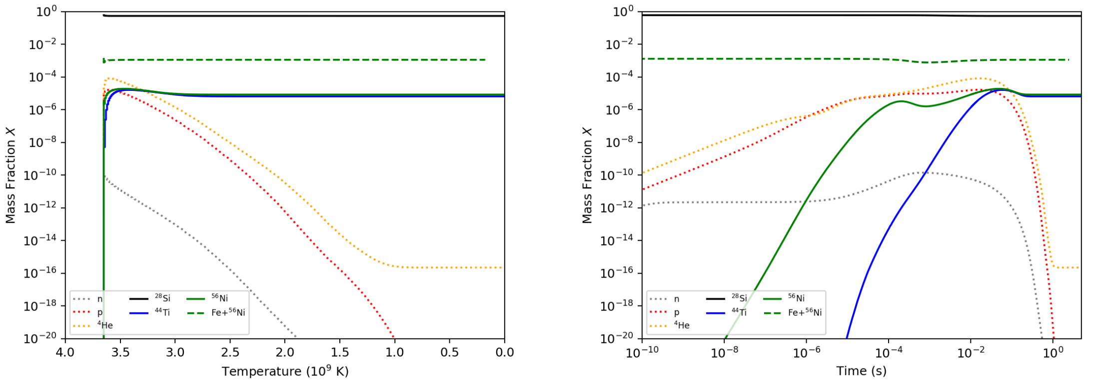

Figure 2.16: Mass fraction evolution plotted against temperature (left) and time (right) for a series of significant isotopes using best-fit power law trajectories for temperature and density of the region 1 particles.

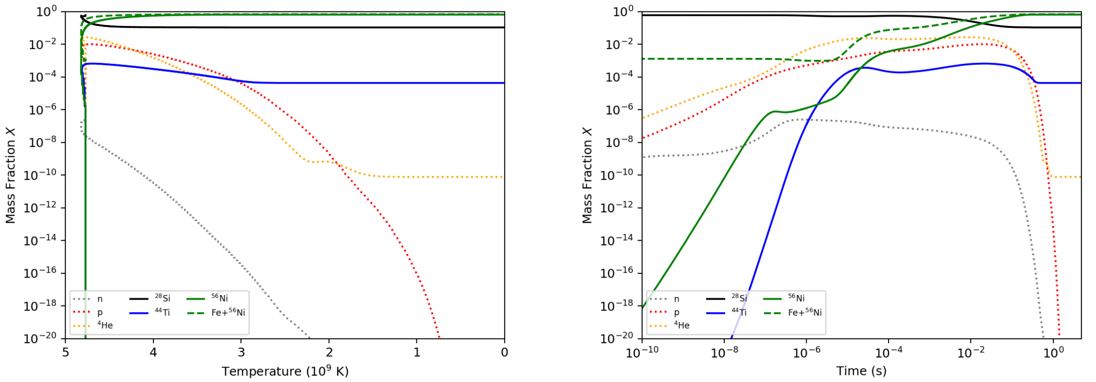

Figure 2.17: Same as Figure 2.16, but using best-fit power law trajectories of the region 2 particles.

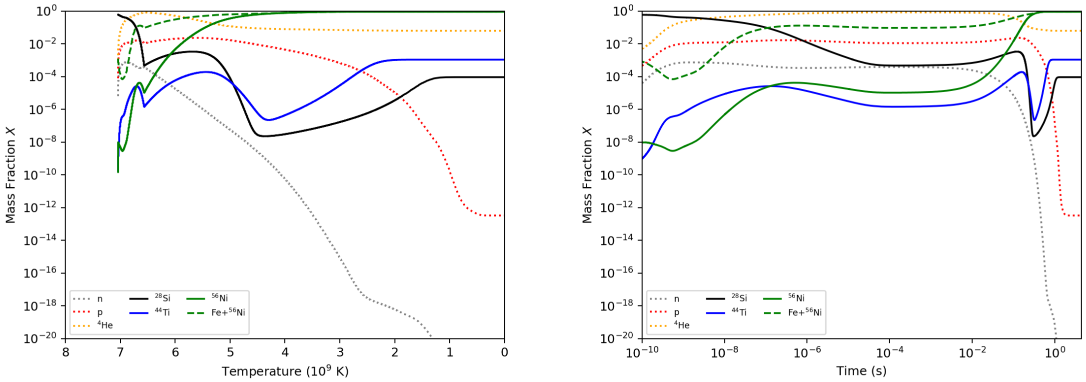

Figure 2.18: Same as Figure 2.16, but using best-fit power law trajectories of the region 3 particles.

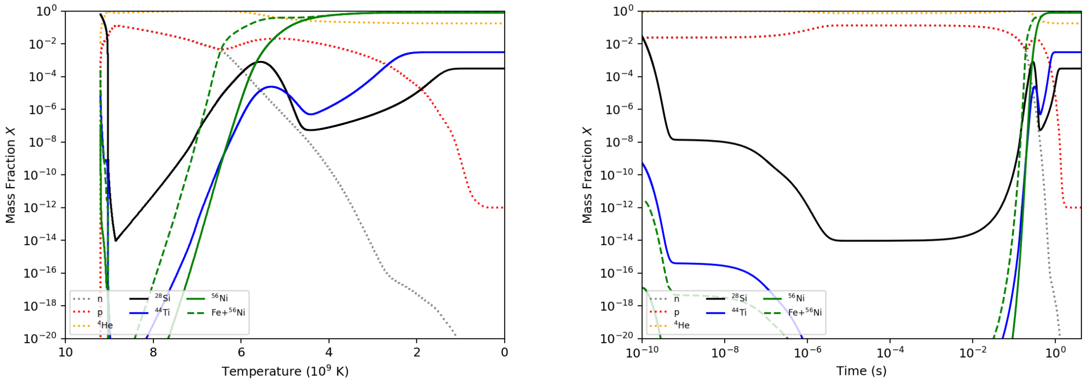

Figure 2.19: Same as Figure 2.16, but using best-fit power law trajectories of the region 4 particles.

law profile. The same abrupt evolution occurs in region 2, causing slightly different final yields. As with region 1, the increase in the temperature when the material is hit by the reverse shock has only a minimal effect on the final yields.

Regions 3 and 4 are hotter than the first two regions and most of the ^{44}Ti production occurs when the trajectory is well mimicked by a power law. However, the reverse shock drives the temperatures in these two regions sufficiently high to alter the late-time burning, altering the final yields. In these cases, this phase increases the net ^{44}Ti production.

In the very broad α-rich freezeout region both ^{56}Ni and ^{44}Ti have a weak dependence on thermodynamic conditions and converge on a low Fe/^{44}Ti ratio, the exact value of which can be altered by dynamics that deviate from an analytic trajectory. The transition to the QSE-leakage chasm is extremely sharp in temperature. Within the chasm, many particles have log(Fe/^{44}Ti) $\sim$ 3.9, and very little material with intermediate Fe/^{44}Ti is produced. On the Si-burning side of the chasm ^{44}Ti abruptly rises, though not to the level seen in the α-rich freezeout. At lower temperatures, production of both ^{56}Ni and ^{44}Ti are similar and much reduced, but the presence of Fe in the star's original composition conspires to maintain a ratio of log(Fe/^{44}Ti) $\sim$ 2.6. This low temperature, low ^{56}Ni material should, in principle, be distinguishable from high temperature production with a similar log(Fe/^{44}Ti) $\sim$ 2.6 by the presence of significant amounts of Si. For material in a Population I supernova with $\rho(T_{\rm peak}) < 1.0 \times 10^8$ g cm^{-3}, a broadly bimodal Fe/^{44}Ti distribution like that observed in Cas A is a natural consequence of the nucleosynthesis. Since the formation of this bimodal distribution in Fe/^{44}Ti is so robust to details of the trajectories, we should find observationally that this distribution is a common feature of supernova remnants.

These studies of the yields production confirm the basic trends in Magkotsios *et al.* (2010) with the yields depending on different physics in different regions, but the final results *do* depend on the temperature/density evolution of the ejecta. In some cases, an exponential decay followed by a power law decay may be a better fit for the trajectories, but neither of these trajectories account for the pileup and heating of the ejecta which, for some cases, can significantly alter the yields. It is important to gain intuition from simple trajectories, but quantitative results will require studies using simulated temperature/density evolution.

2.5 Summary

In this paper, we studied the ^{44}Ti and ^{56}Ni production in a three-dimensional supernova explosion model. For the most part, these two isotopes are both produced in the innermost ejecta of the explosion, and their distributions reflect the asymmetries in the supernova engine. Figure 2.20 shows the ^{44}Ti distribution at late times in our model. The asymmetries in this distribution trace asymmetries in the explosive engine. The total iron distribution (shown in figure 2.21) extends beyond the ^{44}Ti, but also traces the asymmetries in the explosive engine. Figure 2.22 shows the Fe/^{44}Ti ratio in regions with ^{44}Ti mass fraction $X(^{44}\mathrm{Ti}) > 10^{-6}$. As shown in Figures 2.3 and 2.4, the Fe/^{44}Ti ratios of particles in the explosion form a largely bimodal distribution with peaks at log(Fe/^{44}Ti) ~ 2.5 and log(Fe/^{44}Ti) ~ 3.9. This formation of such a distribution is robust under a range of conditions, so it would be expected as a common feature of supernova remnants.

The Fe/^{44}Ti ratio provides additional clues into the nature of the supernova explosion. We have shown how the density and temperature evolution affects this ratio. Asymmetric supernovae like our model produce a wide range of conditions that can produce Fe/^{44}Ti ratios that vary from as low as log(Fe/^{44}Ti) ~ 1.0 (up to $\sim 10\%$ of the total mass of iron in ^{44}Ti) to high log(Fe/^{44}Ti) values exceeding 5.0 (very little ^{44}Ti). In general, the trends in these yields follow the trends studied by Magkotsios *et al.* (2010) where the α-rich freezeout region produces the most ^{44}Ti (lowest Fe/^{44}Ti value). Material produced in the chasm or in the incomplete-burning (i.e., silicon-rich) region produces higher Fe/^{44}Ti values. High ^{44}Ti abundances in maps of supernova remnants like those done by NuSTAR (Magkotsios *et al.*, 2010) probe strong shock regions.

However, the density and temperature evolution can vary dramatically from the

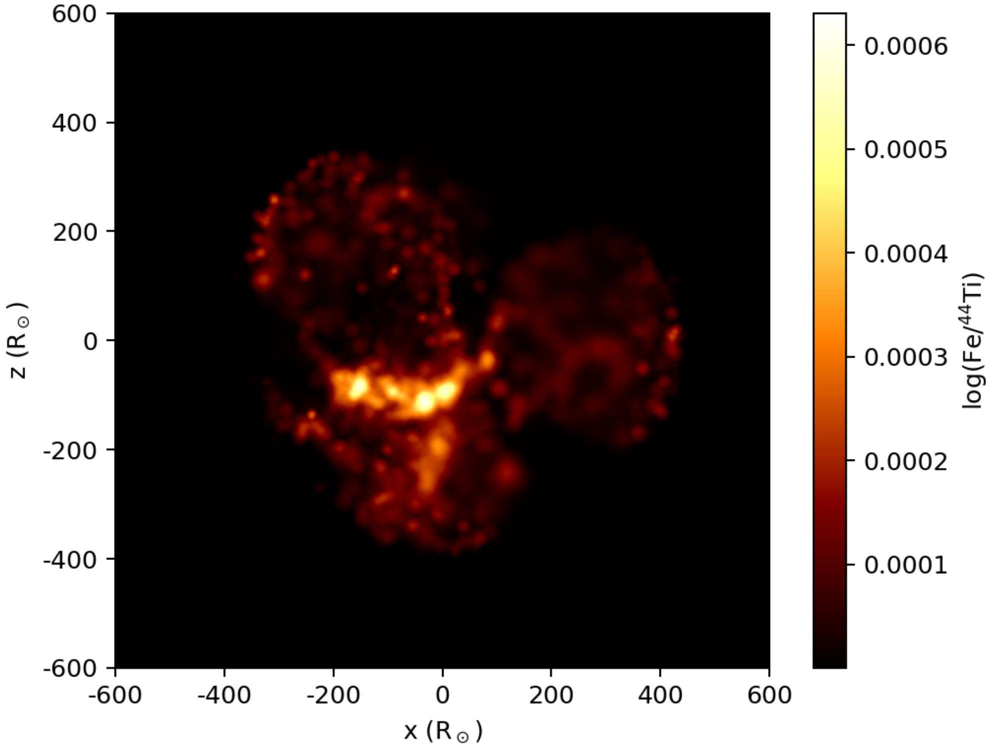

Figure 2.20: Rendering in 3D of the ^{44}Ti distribution tracing the asymmetries in the supernova engine. The color intensity indicates the log of the mass fraction of ^{44}Ti. The distribution of the ^{56}Ni traces the same regions.

simple power law or exponential decays studied in most parameter studies. In our asymmetric explosions, shocks can cause some ejecta to re-heat while still undergoing nuclear burning, and these alterations in the evolution can significantly alter the final yields. Detailed three-dimensional studies such as those presented here are essential in using details in the observed abundances to probe the exact conditions of the shocks.

In this work, we also demonstrate that full 3D supernova models are capable of developing stochastic large-scale asymmetries driven by convection from fallback of material onto the proto-neutron star. Since this asymmetry formed on its own and was not imposed by the model setup, it seems likely that other 3D models could independently develop similar behaviors. Indeed, this behavior could be an important

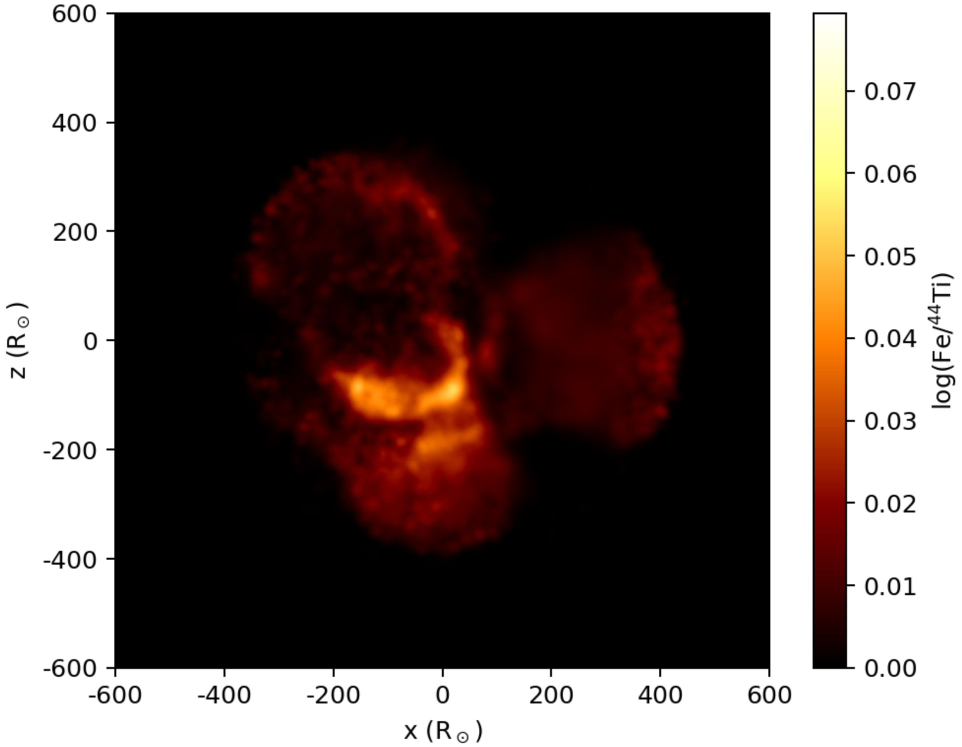

Figure 2.21: Rendering in 3D of the total iron distribution, consisting of all Fe isotopes plus ^{56}Ni. As with figure 2.20, the color intensity indicates the log of the mass fraction. The total iron production in our model extends beyond the ^{44}Ti distribution (see figure 2.20).

universal feature of supernovae. The uniformity of this nucleosynthetic behavior under the effect of stochastic motions from convective processes implies that the details of circulation of material from any early time process, whether convection from the engine, changing gravitational potential, or pre-explosion progenitor convection, are not the dominant controllers of Fe/^{44}Ti. We should expect a bimodal Fe/^{44}Ti distribution in the majority of supernovae with ejecta that reaches NSE temperatures. Uniformly low Fe/^{44}Ti would indicate that only very high density material reached NSE temperatures. In order for lower density material to produce only low Fe/^{44}Ti, little QSE processing can take place despite material being heated to NSE. Therefore

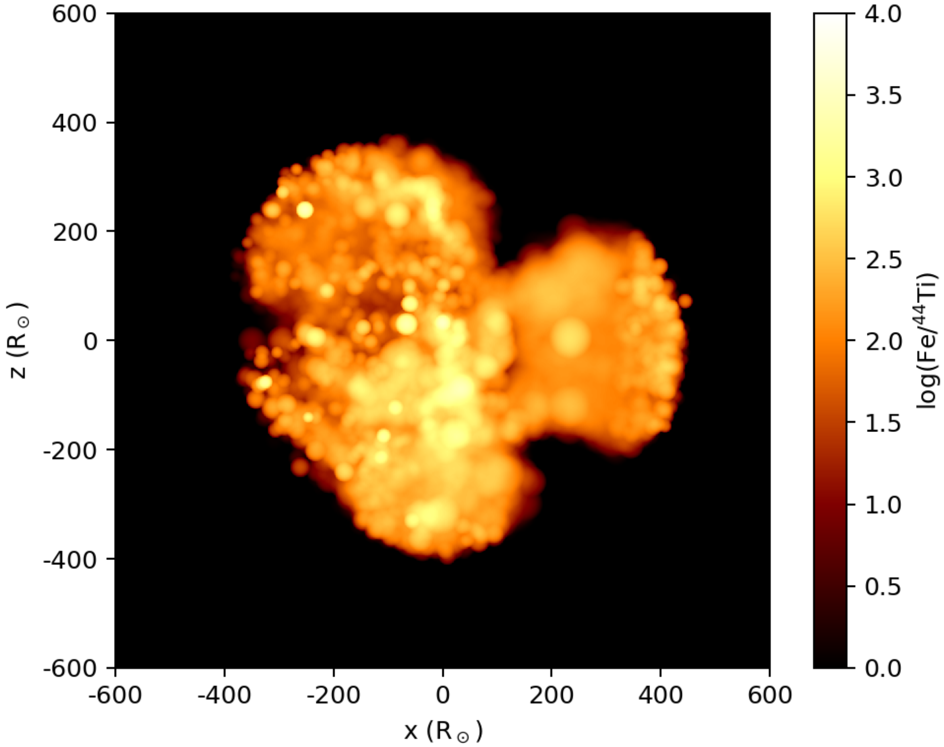

Figure 2.22: Rendering in 3D of the spatial Fe/^{44}Ti ratio in our model. The color intensity indicates the log of the ratio.

a low Fe/^{44}Ti unimodal distribution requires a very massive progenitor to produce the requisite densities and a strongly asymmetric explosion to excavate the high density material without heating shallower, lower density regions to NSE temperatures.

Many remnants are too distant to be resolved with high-energy telescopes. However, we can use the Doppler broadening of lines to study the structure in the ejecta. Figure 2.23 shows the velocity distribution of the ^{44}Ti, ^{56}Ni, and the Fe + ^{56}Ni ejecta for a few different lines of sight in our simulation. The structure in these velocity distributions can provide evidence of asymmetries in the explosive engine. Hard X-ray and γ-ray missions that have good energy resolution may be able to resolve these features. As the sample of such observations grow, we will be able to study the level

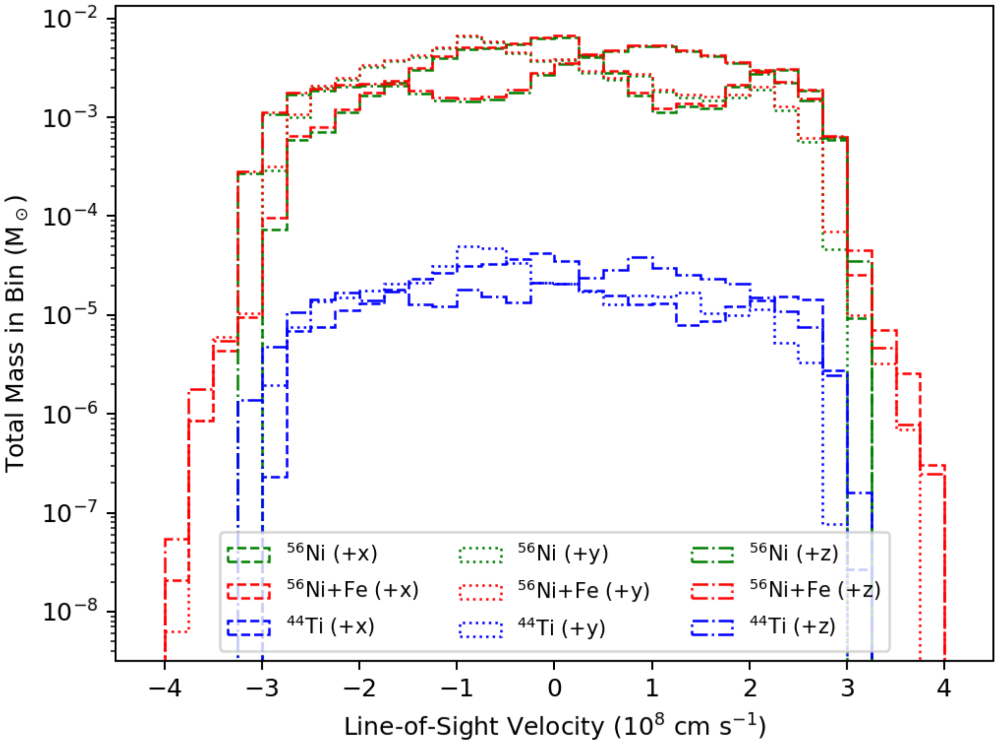

Figure 2.23: A visualization of ^{56}Ni, ^{44}Ti, and total iron distribution plotted against line-of-sight velocity for a sample of three lines of sight (parallel to the x axis, parallel to the y axis, and parallel to the z axis.

of asymmetry in core-collapse supernovae.

Other abundances also depend on the shock strength (figure 2.24), and observing the variations of these abundances in different regions of the remnant can also probe properties of the explosion. Figure 2.24 shows both the total yield distribution as well as the yield distributions in each of our four regions independently. The hotter regions visibly produce heavier elements in greater abundance, but we defer a detailed study of these abundances to a later paper. Our models do not include late-time engine interactions that are seen in many multi-dimensional models (e.g., Harris *et al.*, 2017). These effects will also alter the yields, and much more work is needed to understand the full yields from supernovae.

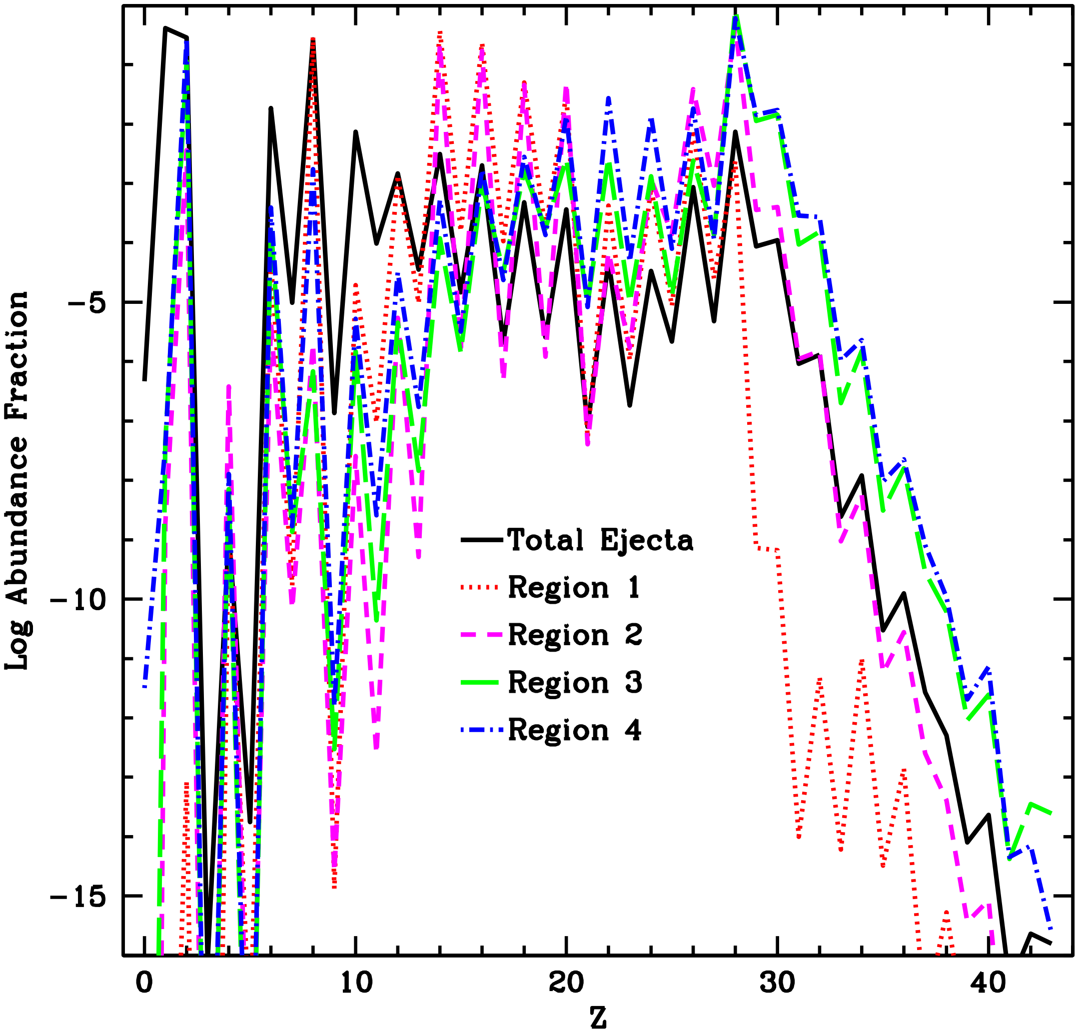

Figure 2.24: Total and specific abundances plotted against isotope proton number Z for all four discussed regions in our explosive ejecta.

Chapter 3

SEARCHING FOR A GALACTIC COMPONENT IN THE ICECUBE TRACK-LIKE NEUTRINO EVENTS

3.1 Abstract

Searches for spatial associations between high-energy neutrinos observed at the IceCube Neutrino Observatory and known astronomical objects may hold the key to establishing the neutrinos' origins and the origins of hadronic cosmic rays. While extragalactic sources like the blazar TXS 0506+056 merit significant attention, Galactic sources may also represent part of the puzzle. Here, we explore whether open clusters and supernova remnants in the Milky Way contribute measurably to the IceCube track-like neutrino events above 200 TeV. By searching for positional coincidences with catalogs of known astronomical objects, we can identify and investigate neutrino events whose origins are potentially Galactic. We use Monte Carlo randomization together with models of the Galactic plane in order to determine whether these coincidences are more likely to be causal associations or random chance. In all analyses presented, the number of coincidences detected was found to be consistent with the null hypothesis of chance coincidence. Our results imply that the combined contribution of Galactic open clusters and supernova remnants to the track-like neutrino events detected at IceCube is well under 30%. This upper limit is compatible with the results presented in other Galactic neutrino studies.

3.2 Introduction

The observed spectrum of cosmic rays extends to energies in excess of 10^{18} eV (Beatty and Westerhoff, 2009), raising fundamental questions about the nature of cosmic ray origins. Especially above the spectral feature known as "the knee" at $\sim 3 \times 10^{15}$ eV (3 PeV), it is still unknown where or how particles are accelerated to such high energies (e.g., Blasi, 2013; Gabici *et al.*, 2019). Cosmic rays at these energies are deflected by Galactic magnetic fields en route to Earth, scrambling their arrival directions and greatly complicating the task of source identification (Halzen and Hooper, 2002).

High-energy neutrino astronomy may hold the key to overcoming this problem, since cosmic accelerators are also expected to be astrophysical beam dumps. In an astrophysical beam dump, accelerated cosmic rays encounter ambient matter or photons in close proximity to the cosmic ray source, resulting in pp or $p\gamma$ interactions which can produce neutral and charged pions (π^0, $\pi^\pm$) (Gaisser, 1990; Ahlers and Halzen, 2018). Subsequent pion decays yield gamma ray photons and neutrinos (as well as antineutrinos), which constitute secondary emission that can be used to trace the location of the accelerator (Halzen and Hooper, 2002). Neutrinos are of particular interest, since they can reach Earth without deflection by magnetic fields and, in most cases, without flux attenuation due to intervening matter or background photons.

In 2013 and 2014, the IceCube Collaboration published the first evidence of high-energy extraterrestrial neutrinos (IceCube Collaboration, 2013; Aartsen *et al.*, 2014b). A diffuse flux of neutrinos with energies of 0.01–2 PeV was detected, and its origins are still largely a mystery (see, e.g., Aartsen *et al.*, 2017a,e, 2019; Albert *et al.*, 2020). With the exception of the blazar TXS 0506+056 (IceCube Collaboration *et al.*, 2018; Mirzoyan, 2017; Ojha and Valverd, 2018) (possibly PKS 1502+106 (IceCube

Collaboration, 2019) and NGC 1068 (Aartsen *et al.*, 2020b) as well), the majority of IceCube's neutrino events remain unattributed to any known astronomical sources. Despite the prominence of the TXS 0506+056 result, an analysis by the IceCube Collaboration concluded that the combined diffuse neutrino flux contribution of all blazars listed in the 2nd Fermi-LAT AGN Catalog (2LAC) could be no more than 27% (Aartsen *et al.*, 2017b), so the search continues for contributions from other types of sources.

In principle, the diffuse neutrino flux should have components of both Galactic and extragalactic origin. Observations so far are consistent with isotropy, suggesting that any Galactic component is sub-dominant (Aartsen *et al.*, 2017a). Still, it is plausible that ∼10–20% of the flux originates within our Galaxy, with the overall neutrino spectrum having a softer Galactic component concentrated at energies $\lesssim$ 100 TeV and a harder extragalactic component accounting for most of the highest-energy events (Palladino and Vissani, 2016). It has been claimed that an excess of the IceCube neutrino flux above 100 TeV comes from the Galactic plane (Neronov and Semikoz, 2016), but the IceCube Collaboration found that this excess flux is still compatible with the flux observed from other regions of the sky with a p-value of ∼43% (Aartsen *et al.*, 2016). A more recent analysis by IceCube constrained the Galactic component to less than 14% of the total flux above 1 TeV (Aartsen *et al.*, 2017e). Other works, including those using the neutrino detector ANTARES, have found constraints that are either similar or even more restrictive ($< 9.5\%$ with 90% confidence) (e.g., Mandelartz and Becker Tjus, 2015; Denton *et al.*, 2017; Albert *et al.*, 2017).

Two main techniques have been used in attempts to associate high-energy neutrinos with Galactic or extragalactic sources: spatial association and neutrino emission modeling. Studies searching for spatial associations often use statistical techniques to search for excesses in the number of neutrino events arriving from the directions of known objects or from pre-selected regions of the sky (e.g., Emig *et al.*, 2015; Moharana and Razzaque, 2015; Neronov and Semikoz, 2016; Moharana and Razzaque, 2016; Aartsen *et al.*, 2017b,e; Lucarelli *et al.*, 2019; Hooper *et al.*, 2019; Lunardini *et al.*, 2019; Kheirandish and Wood, 2019; Moharana *et al.*, 2020). Since gamma ray emission due to π^0 decays is also expected from high-energy neutrino sources, gamma ray catalogs are often used to provide physically motivated lists of known objects for these types of analyses. In the neutrino emission modeling approach, authors determine the expected neutrino flux from specific classes of sources (either individually or collectively) and compare their theoretical predictions with the empirical flux limits and spectral indices provided by neutrino observatories (e.g., Yuan *et al.*, 2011; Ahlers and Halzen, 2014; Bednarek *et al.*, 2014; Anchordoqui *et al.*, 2014; Mandelartz and Becker Tjus, 2015; Bykov *et al.*, 2015; Ahlers *et al.*, 2016; Bai *et al.*, 2016; Chakraborty and Izaguirre, 2016; Murase and Waxman, 2016; Halzen *et al.*, 2017; Gupta and Razzaque, 2017; Bykov *et al.*, 2018; Palladino *et al.*, 2018; Sudoh *et al.*, 2018). Many such predictions are not yet testable and will require additional years of data or the increased sensitivity of future neutrino detectors such as KM3NeT (Adrián-Martínez *et al.*, 2016) or IceCube-Gen2 (IceCube-Gen2 Collaboration *et al.*, 2014).

In this work, we use a spatial association approach to search for a Galactic contribution among the track-like subset of neutrino events detected at IceCube (Aartsen *et al.*, 2016). We restrict our Galactic search to two classes of energetic objects, both of which have seen consideration as potential high-energy neutrino sources: open clusters (OCs) (e.g., Odrowski *et al.*, 2013; Bednarek *et al.*, 2014; Bykov *et al.*, 2015; Gupta and Razzaque, 2017; Bykov *et al.*, 2018) and supernova remnants (SNRs) (e.g., Yuan *et al.*, 2011; Mandelartz and Becker Tjus, 2015; Ahlers *et al.*, 2016; Aartsen *et al.*, 2017e, 2020a). The track-like IceCube neutrino events and our chosen astronomical catalogs of Galactic OCs and SNRs are discussed fully in Section 3.3. The statistical analysis that we present is a variation of the well-known "nearest neighbor" method, which has seen previous use searching for coincidences with candidate neutrino sources (e.g., Emig *et al.*, 2015; Moharana and Razzaque, 2015; Lunardini *et al.*, 2019). In section 3.4, we discuss our method in detail and explain how its capabilities have been expanded for application to the Galactic plane. Our results are presented and discussed in Section 3.5, and we close with some brief conclusions in Section 3.6. Our findings are broadly consistent with upper limits on Galactic sources as quoted by other studies (Aartsen *et al.*, 2017e; Denton *et al.*, 2017; Albert *et al.*, 2017). The results act as a cross-check with previous SNR results by other authors, and also represent the first time that OCs have been considered in a spatial association neutrino search with a catalog of objects.

3.3 Data

3.3.1 IceCube Track-like Neutrino Events

The IceCube Neutrino Observatory is made up of of 5160 photomultiplier tubes frozen into 1 km^3 of Antarctic ice at the South Pole (Aartsen *et al.*, 2017c). When a high-energy neutrino (or antineutrino) of any flavor interacts with an atomic nucleus in the ice, relativistic charged particles are produced, emitting Cherenkov light that IceCube detects (Aartsen *et al.*, 2017d). Neutrino events in the detector have either a track-like signature or a cascade signature; the latter are produced by neutral-current interactions of all three neutrino flavors, as well as by charged-current interactions of electron and tau neutrinos (Aartsen *et al.*, 2017d). Cascades yield particle showers of range $\lesssim$ 20 m (Aartsen *et al.*, 2014a) with a light signature that is nearly spherically symmetric, so the angular uncertainty of cascade event reconstructions is $\gtrsim 10^\circ$ (Aartsen *et al.*, 2017d). In contrast, a charged-current interaction of a muon neutrino yields a high-energy muon which typically travels several kilometers through the ice (Chirkin and Rhode, 2004), producing a track-like signature with typical angular resolution of $\lesssim 1^\circ$ in reconstruction (Aartsen *et al.*, 2017d).

Our analysis uses 29 track-like neutrino events published by the IceCube Collaboration after six years of operation (Aartsen *et al.*, 2016). All of these events have observed energies of 200 TeV or more, an imposed energy cut which results in an expectation of roughly twice as many astrophysical events as background atmospheric events. Each neutrino event is published with angular errors on the reconstructed arrival direction corresponding to 50% and 90% confidence levels that are asymmetric in both right ascension and declination. For the purposes of our statistical analysis, we create circular error regions centered on each event with the same area as the original error ellipse by using the geometric mean of all four angular errors at the 90% confidence level (see Section 3.4.1). We use circularized errors because our statistical method is primarily sensitive to the total area of the error ellipse, and circular errors simplify the angular separation calculations required. Note that we do not consider cascade events in this work due to their large angular uncertainties—the smaller errors of the track-like events make them better-suited to point source searches using positional coincidence, since chance associations become less likely when the collection of all error ellipses covers a smaller solid angle on the sky.

The reconstructed arrival directions of the 29 track-like neutrinos are concentrated in the lower latitudes of the Northern Hemisphere (declinations $-5^\circ < \delta < +50^\circ$, see Figure 3.1). Most datasets published by the IceCube Collaboration require that the vertex of neutrino interaction occur within the instrumented detector volume, but this set of track-like events allows for interactions both inside and outside the

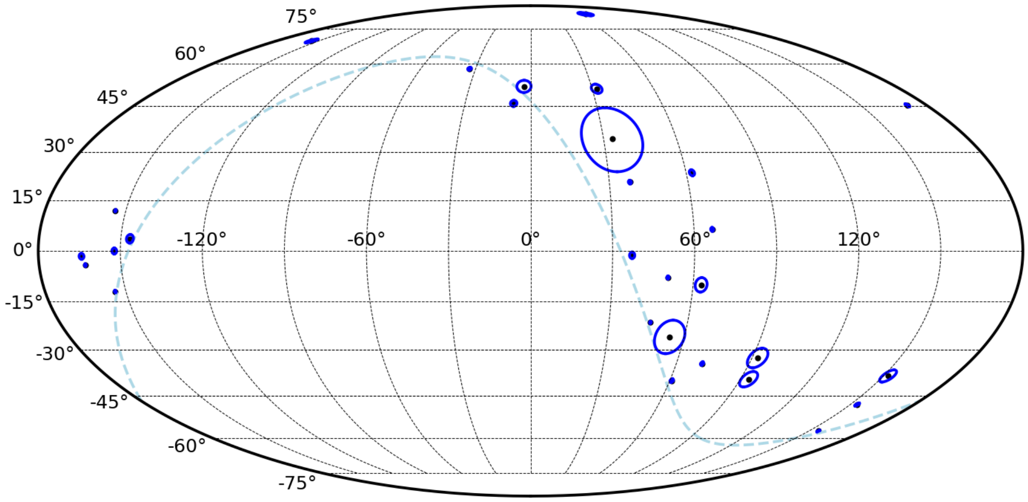

Figure 3.1: Sky map in Galactic coordinates showing the distribution of arrival directions (black dots) and angular errors (blue circles) for the 29 track-like neutrinos (Aartsen *et al.*, 2016). The displayed errors have been circularized as described in the text. The dashed light blue line shows the celestial equator.

detector. This increases the effective area of the detector due to the long range of the muons produced by muon neutrino interactions, but makes it necessary to restrict the field of view to the Northern Hemisphere (below IceCube's horizon) where the Earth efficiently filters out the background noise of atmospheric muons.

3.3.2 Candidate Sources: Open Clusters

OCs are one class of Galactic source which has been suspected of playing host to high-energy cosmic accelerators. Many such OCs represent compact collections of dense interstellar matter grouped together with energetic objects such as massive OB stars, compact massive binaries, pulsars (often with associated pulsar wind nebulae), and SNRs (Bednarek *et al.*, 2014). Several of these types of objects have been investigated as suspected cosmic ray accelerators by themselves. For instance, Galactic SNRs are likely the principal source of cosmic rays at energies below the knee (see Section 3.3.3). The Eta Carinae binary system in Trumpler 16 has been detected in gamma-ray observations up to ∼100 GeV and has been studied as a potential accelerator (Tavani *et al.*, 2009; Abdo *et al.*, 2009; Farnier *et al.*, 2011; Bednarek and Pabich, 2011; Gupta and Razzaque, 2017). Massive X-ray binaries (microquasars) including Cyg X-3 and LS 5039 have been proposed as Galactic neutrino emitters (Bednarek, 2005; Anchordoqui *et al.*, 2014). A few notable star clusters have been found to produce TeV gamma-ray emission, including Cygnus OB2 (Aharonian *et al.*, 2002) and the larger Cygnus X star-forming region (Yoast-Hull *et al.*, 2017; Abeysekara *et al.*, 2021), Westerlund 2 (Aharonian *et al.*, 2007), Westerlund 1 (Abramowski *et al.*, 2012), and Cl* 1806-20 (H. E. S. S. Collaboration *et al.*, 2018). Such emission could be indicative of π^0 decays associated with hadronic neutrino production. Several theoretical studies of star clusters have examined neutrino detection prospects, and the results suggest fluxes detectable by IceCube or by next-generation detector KM3NeT, especially if several acceleration mechanisms are simultaneously active within the same cluster (Bednarek *et al.*, 2014; Bykov *et al.*, 2015, 2018).

A wide variety of physical accelerator scenarios have been proposed in order to explain the observed TeV gamma-ray emission from select OCs. These scenarios frequently involve powerful winds from massive stars, supernova shocks from the deaths of those stars, and/or compact objects from the collapsed cores of exploded stars interacting with dense regions of ambient gas and dust within the star cluster (e.g., Bednarek *et al.*, 2014, and references therein). In massive binary systems, particle acceleration may occur in the region where the two stars' stellar winds collide (Bednarek and Pabich, 2011; Bednarek *et al.*, 2014; Gupta and Razzaque, 2017). Galactic microquasars are powered by accretion disks whose associated jets could transfer considerable kinetic energy to relativistic nuclei (Bednarek, 2005; Anchordoqui *et al.*, 2014). The collision of a supernova shock with the cumulative stellar winds of a compact cluster of young stars might theoretically be capable of accelerating protons to energies in excess of 1 PeV (Bykov *et al.*, 2015, 2018). At this time, it is unclear which of these processes (if any) contribute most to the high-energy budget of a star cluster; indeed, the answer may vary from one cluster to the next (Bednarek *et al.*, 2014).

For our investigation of OCs, we employ two datasets: (1) an extensive, general catalog of Galactic OCs and (2) a more restricted list of massive, young OCs which may provide an optimal accelerator environment for producing neutrinos and gamma-ray emission. Below, we briefly describe each list of candidate sources and our motivations for selecting those objects.

- *New catalog of optically visible open clusters and candidates* (Dias *et al.*, 2002)

  OPENCLUST is a list of Galactic OCs which was first compiled in 2002 from a combination of older catalogs (Lauberts, 1982; Lyngå, 1987; Mermilliod, 1995) and several isolated papers published more recently (for a full list, see Dias *et al.*, 2002). Many objects were visually checked by the authors using Digitized Sky Survey[1] (DSS) plates in order to verify their coordinates and existence. The list includes fundamental parameters and kinematic data where available, and is designed to be an efficient tool for use in OC studies, since all of the included data is stored in a single machine-readable table. The catalog is regularly updated online[2]—the version used in this work contains entries for a total of 2167 OCs and OC candidates, at least 89% of which represent robustly identified OCs.

  This extensive collection of objects is useful for testing a broad hypothesis of potential causal association that is more model-independent: if there is a strong

---

[1] `https://archive.stsci.edu/dss/`

[2] HEASARC implementation: `https://heasarc.gsfc.nasa.gov/W3Browse/all/openclust.html`

causal connection between IceCube neutrinos and Galactic OCs—regardless of the underlying physical reasons—this catalog could reveal the existence of that connection. In addition, OPENCLUST lists the apparent angular size of each OC, which is important for our statistical analysis. OPENCLUST will also provide the framework for constructing a probabilistic model of the spatial distribution of OCs in the Milky Way (see Section 3.4.2); its sheer size makes it an ideal data set for this task.

- *"Accelerator-dominated" open clusters* (Odrowski *et al.*, 2013)

  This data set consists of 36 "accelerator-dominated" open clusters (ADOCs) compiled in 2013 by the IceCube collaboration. The ADOCs are selected from among the 650 Galactic OCs documented in the Catalog of Open Cluster Data (COCD) (Kharchenko *et al.*, 2005b) and its First Extension (Kharchenko *et al.*, 2005a). The authors limit their study to sources in the Northern Hemisphere, since that is where the sensitivity of IceCube is highest, and they also do not consider sources farther than 3–4 kpc from the Sun, with the goal of eliminating OCs with imprecise distance estimates or identifications. The primary selection criterion used to identify OCs in an "accelerator-dominated" phase was their evolutionary status—to be included, an OC must have a turn-off mass above 9 $M_\odot$, corresponding to an age of less than $\sim$40 Myr. OCs much older than this are assumed to be deficient in potential particle accelerators since massive stars will have died and their supernovae will have long since dispersed into the interstellar medium. The final list includes a range of young OCs with total masses between $\sim$400 $M_\odot$ and 3×10^4 $M_\odot$, which are largely concentrated in three cluster complexes associated with spiral arms of the Galaxy.

  The ADOC list is a narrow set of sources assembled with the specific aim of using IceCube to test the hypothesis of young OCs as cosmic ray accelerators and high-energy neutrino emitters. If cosmic ray acceleration within OCs contributes significantly to a Galactic neutrino flux component at IceCube, then these 36 OCs are the most likely candidates for detection. Like OPENCLUST, the COCD which the ADOCs were selected from also provides apparent angular sizes of each OC for our analysis. Finally, we note that Table 1 of Odrowski *et al.* (2013) lists IC 1448 among the 36 selected ADOCs, but this object is a galaxy (better known as NGC 7308) and is not present in the COCD. We will assume that the authors meant to refer to IC 1848 instead.

3.3.3 Candidate Sources: Supernova Remnants

As stated in Section 3.3.2, Galactic SNRs are likely to be the primary source of hadronic cosmic rays with energies at least up to ∼100 TeV, as indicated by a large yet circumstantial body of evidence (Yuan *et al.*, 2011; Blasi, 2013; Bykov *et al.*, 2015). Gamma-ray spectra observed from several SNRs including W44 (Ackermann *et al.*, 2013), IC 443 (Ackermann *et al.*, 2013; Tavani *et al.*, 2010), Cassiopeia A (Araya and Cui, 2010), Tycho's SNR (Morlino and Caprioli, 2012; Berezhko *et al.*, 2013), and others (e.g., Ohira *et al.*, 2011) have been found to favor hadronic emission models (i.e., π^0 decay) over leptonic explanations such as inverse Compton. There are also SNRs such as RX J1713.7−3946 (Abdo *et al.*, 2011) which have gamma-ray spectra that are more compatible with leptonic models. Therefore, the observation of a neutrino flux from SNRs with hadronic gamma-ray emission would offer another tool for differentiating between the two scenarios. The presence of accelerated particles in SNR shocks has been inferred in many cases from X-ray evidence of magnetic field amplification (Völk *et al.*, 2005; Vink, 2012; Bykov *et al.*, 2012, 2013; Schure *et al.*, 2012) and observations of unusual Hα line widths (Blasi, 2013; Heng, 2010).

The common theoretical framework for cosmic ray acceleration in SNRs is diffusive shock acceleration (DSA) at the supernova shock (for a review, see Bell, 2014). The general predictions of DSA are a power law spectrum $E^{-\Gamma}$ of cosmic ray energies with spectral index $\Gamma \approx 2.0$–2.4 up to a cutoff energy, which might extend as high as the knee in some cases (Villante and Vissani, 2008). As cosmic ray energies approach PeV scales, the role of Galactic SNRs becomes less certain; the ability of DSA to reach energies as high as the knee has been repeatedly questioned (e.g., Bell, 2014; Bykov *et al.*, 2015). Hence, a number of more complex scenarios have been proposed. It has been argued that only certain kinds of supernovae (Ptuskin *et al.*, 2010; Bell, 2014) or supernovae exploding in particular environments (Bykov *et al.*, 2015; Binns *et al.*, 2005) provide the conditions necessary to reach knee energies. Magnetic field amplification is likely to be one piece of the puzzle (Schure *et al.*, 2012), and the answer may also include plasma instabilities or alternative shock arrangements (e.g., Bell, 2014; Bykov *et al.*, 2015, and references therein). The SNR G40.5$-$0.5 has been proposed as a potentially detectable point source in IceCube given sufficient exposure over a period of $\sim$10 yr (Mandelartz and Becker Tjus, 2015). A few other Galactic SNRs, including Cassiopeia A, IC 443, Vela Junior, W33, and W41, have also been proposed as neutrino emitters, but theoretical predictions do not expect these to be detectable as point sources in IceCube above the atmospheric backgrounds (Yuan *et al.*, 2011; Mandelartz and Becker Tjus, 2015).

For our SNR study, we make use of another pair of catalogs: (1) a comprehensive list of every known Galactic SNR and (2) a limited subset of SNRs which have been detected at gamma-ray energies and are therefore more likely to play host to high-energy accelerators. The remainder of this subsection describes both of these catalogs and justifies their use.

- *Catalogue of Galactic supernova remnants by D. A. Green* (Green, 2014)

The Green SNRs catalog is a compilation of all currently known Galactic SNRs, which has seen numerous published versions since 1984 (for a list, see Green, 2014). Here, we make use of the updated June 2017 version (Green, 2017), which is available online.[3] The catalog lists 295 Galactic SNRs together with observational data on each object's position, angular size, morphology, radio emission spectral index, and derived flux density at a frequency of 1 GHz. Most of these objects have been detected through their radio emission due to relativistic electrons, which is free of Galactic extinction. More than 93% of the catalog's SNRs have been sufficiently observed in the radio that their flux density at 1 GHz can be determined and included. Due to Galactic absorption at other wavelengths, only ∼40% of the SNRs have been detected in X-rays and ∼30% in the optical. The catalog's completeness is influenced by some selection effects, primarily those affecting radio wavelengths (e.g., Green, 2015). The catalog is complete only down to a surface brightness of $\sim 10^{-20}$ W m^{-2} Hz^{-1} sr^{-1} at 1 GHz, and a higher limit likely applies near the Galactic center, where the background Galactic radio emission is brightest (Green, 2014, 2015).

Despite any limitations, the Green SNRs catalog is the largest available listing of Galactic SNRs. Much like OPENCLUST, the sheer number of objects present makes this collection ideal for testing the broadest class of hypotheses that connects IceCube neutrinos to Galactic SNRs. The angular size estimates in the catalog are relevant for our statistical analysis as presented in Section 3.4. We will also use the distribution of these SNRs to generate our probabilistic model of the distribution of SNRs in the Milky Way.

- *First Fermi LAT supernova remnant catalog* (Acero *et al.*, 2016)

---

[3] See `http://www.mrao.cam.ac.uk/surveys/snrs/`.

The Fermi LAT SNRs are the result of a systematic effort to characterize the 1–100 GeV gamma ray emission within 3° of all known radio SNRs from the Green SNR catalog (Green, 2014, 2017). A total of 30 candidate sources were found to have sufficient significance and spatial overlap with known radio SNRs to be classified by the authors as GeV counterparts of the associated radio SNRs. An additional 14 candidates were designated as "marginally classified" due to lower degrees of significance and/or spatial overlap, and a further 245 flux upper limits were presented in other cases. By scrambling the Galactic longitudes of known SNRs to create a mock catalog, the authors determined an upper limit of 22% for the fraction of candidates that were falsely identified as SNRs.

In this work, we use both the classified and marginally classified candidates from the Fermi LAT SNRs catalog for a grand total of 44 objects. The inclusion of the marginally classified candidates did not qualitatively change our results. The catalog provides positional data and angular radius estimates for each object, both of which are used for our analysis as presented in Section 3.4. Much like the ADOC list presented in Section 3.3.2, this catalog has the advantage that it carries greater physical motivation in terms of cosmic ray acceleration and neutrino emission. Since gamma-ray emission can result from the same hadronic processes, these Galactic SNRs are more likely to be neutrino emitters than most of the Green SNRs.

3.4 Methodology

3.4.1 Statistical Method of Coincidences

Our analysis technique is a variant of the well-established "nearest neighbor" method. Such methods have a history of use in both astronomy (e.g., de Ruiter *et al.*, 1977; Windhorst *et al.*, 1984; Sutherland and Saunders, 1992) and astroparticle physics (e.g., Virmani *et al.*, 2002; Moharana and Razzaque, 2015; Emig *et al.*, 2015; Lunardini *et al.*, 2019). Here, we summarize the important concepts, focusing mainly on the newest additions. We refer to our previous work (Emig *et al.*, 2015; Lunardini *et al.*, 2019) for a more extended presentation.

We begin with a collection of N neutrino events and M candidate sources. For each event ν_i, where $i = 1, \ldots, N$, we define the unitless quantity r_i as

$$r_i = \min_j \left(\frac{S_{i,j} - a_j}{\sigma_{\nu,i}} \right), \tag{3.1}$$

where $j = 1, \ldots, M$ runs over the set of candidate sources. The quantity $S_{i,j}$ is the angular separation between ν_i and the center of the jth candidate source, a_j is the angular radius of the jth candidate source, and $\sigma_{\nu,i}$ is the angular error associated with event ν_i. To simplify the calculation of r_i, the neutrino event error ellipses and the candidate sources are both treated as circular (which may cause individual values of r_i to be underestimated or overestimated). Where necessary, their shapes were circularized using the geometric mean of the available dimensions to yield a single angular radius for a circle with the same area as the original ellipse.[4] If the angular extent of a candidate source is unavailable, then we take the conservative approach of treating it as a point source with $a_j = 0$.

---

[4] By approximating small circles and ellipses on the spherical sky with their Euclidean equivalents, we can show that $A_{\text{circle}} = \pi r^2 = \pi(\sqrt{ab})^2 = \pi ab = A_{\text{ellipse}}$.

The quantity r_i can be regarded as the normalized angular separation between the arrival direction of ν_i and the edge of the nearest candidate source. From here onward, the index i will be dropped for simplicity, and the notation r will be used to indicate the normalized angular separation. For any catalog of candidate source positions and angular sizes, we can empirically calculate the r values, one for each of the N neutrino events. To test for a causal relationship between the candidate sources and the neutrinos, we compare the distribution of r values with a null distribution, which is the expected distribution of r values in a scenario where there exists no causal relationship and any apparent correlations are due to random chance. The null distribution is obtained using a Monte Carlo procedure which generates $K = 10^6$ randomized realizations of the N values for r.

Our primary strategy to compare the two distributions is to use the number of coincidences N_c as a test statistic. We define a *coincidence* as the occurrence of a neutrino event having $r < 1$, so the number of coincidences is an integer such that $0 \leq N_c \leq N$. Many of the K Monte Carlo realizations of the null distribution will include coincidences that occur by random chance. We define N_{better} to be the number of Monte Carlo realizations which happen to produce at least N_c coincidences. Then, $p = N_{\mathrm{better}}/K$ is our p-value, the approximate probability that a number of coincidences larger than or equal to the observed N_c is realized in the null distribution. If N_c greatly exceeds the typical number of coincidences expected in the null hypothesis, then $p \ll 1$, which could be indicative of a causal relationship between the neutrinos and the candidate sources.

As an alternative approach, we also study the entire distribution of r using a Kolmogorov-Smirnov (K-S) test. Using a two-sample K-S test, we evaluate the hypothesis that the N empirical r values were drawn from the same underlying distribution as the set of KN values drawn from the null distribution. If the test's p-value is near zero, it suggests that the empirical r values were drawn from an underlying distribution which differs from the null distribution in a statistically significant way. Such a result could indicate a relationship between the chosen candidate sources and the neutrinos, but not necessarily a causal one. While the first approach using the number of coincidences is a more direct way of discovering spatial correlations in the data, the K-S test approach is a more general check for consistency between the real data and the null distribution. We note that the p-values resulting from both strategies are pre-trial values, since they do not take into account the total number of hypotheses that were tested. Post-trial p-values would be larger, i.e., they would have lower significance.

3.4.2 Galactic Null Distributions

The Monte Carlo procedure for generating null distribution realizations approaches the problem by randomizing the positions of the M candidate sources while leaving the arrival directions of the N neutrino events fixed. Extragalactic sources can, in most cases, be assumed to have an isotropic distribution on the sky (Emig *et al.*, 2015; Lunardini *et al.*, 2019), which we imitate by choosing points uniformly distributed on the surface of a sphere. Since the candidate sources used in this work are Galactic sources, they are *not* distributed isotropically, but are instead heavily concentrated along the Galactic plane. For each candidate source catalog that we use, 96% or more of its objects are within 20° of the Galactic plane, i.e., they have Galactic latitudes b satisfying $-20^\circ < b < +20^\circ$. In addition, the SNR catalogs show a greater concentration of objects towards the Galactic center at Galactic longitude $\ell = 0^\circ$ and a correspondingly lower concentration towards the Galactic anticenter at $\ell = \pm 180^\circ$. Therefore, the Monte Carlo randomization must take all these physical realities into account.

Using the procedure known as transform sampling (e.g., see Section 7.2 of Press *et al.*, 1992), random values are generated from any desired probability distribution. To model the probability distribution function (PDF) of Galactic objects on the sky, we used Bayesian parameter estimation with the `dynesty` software package (Speagle, 2020) to obtain median posterior parameter values for a set of model distributions. Since `dynesty` also provides estimates of the Bayesian evidence, we were able to compare the models to one another using odds ratios and select those which showed the best agreement with the available data. We consider a factorized PDF having the form $F(b, \ell) = B(b)L(\ell)$, where $B(b)$ and $L(\ell)$ are assumed to be independent functions. This is accurate to first order, since the latitude and longitude distributions of objects in the Galactic disk arise from two distinct physical mechanisms (Binney and Dehnen, 1997; Oort, 1932), even if a mild interdependence may exist on small scales.

For the latitude distribution $B(b)$, the best model (as determined via odds ratios) used a functional form inspired by the plane-perpendicular blue-light distribution of edge-on galaxy disks (de Grijs *et al.*, 1997):[5]

$$B(b) = A_b \left[f_1 \operatorname{sech}\left(\frac{b - b_0}{h_{b1}}\right) + f_2 \operatorname{sech}\left(\frac{b - b_0}{h_{b2}}\right) \right] \qquad f_1 + f_2 = 1 \qquad f_1, f_2 \geq 0. \tag{3.2}$$

This model surpassed eight other models including a cosine, an exponential, a single hyperbolic secant, a hyperbolic secant squared, a Gaussian, and the full functional form proposed for edge-on galaxy disks (de Grijs *et al.*, 1997). The four independent parameters are b_0, h_{b1}, h_{b2}, and $f_1 = 1 - f_2$. The value A_b is the normalization, chosen so that $B(b)$ integrates to 1 over the interval $-90° \leq b \leq +90°$. The parameter b_0 represents the offset position of the central peak, about which the distribution is

---

[5] Note that $\operatorname{sech} x$ is the hyperbolic secant of x, defined as $\operatorname{sech} x \equiv 1/\cosh x = 2/(e^x + e^{-x})$, where cosh is the hyperbolic cosine.

symmetric. Such an offset from the Galactic plane is expected due to the vertical position of the Sun within the Galactic disk. The parameter h_{b1} is the (relatively narrow) angular width of the first sech distribution (representing the thin disk of the Galaxy), and h_{b2} is the (relatively broad) angular width of the second sech distribution (representing the thick disk). The parameters f_1 and f_2 are the fractional amplitudes of the two sech distributions, which together comprise a single independent parameter.

The longitude distribution $L(\ell)$ varied by catalog. For some catalogs, the dependence on longitude was weak enough that the best model was a uniform distribution with the functional form

$$L(\ell) = \frac{1}{360^\circ}. \tag{3.3}$$

This model has zero parameters, and the constant value $1/360^\circ$ is the necessary normalization so that $L(\ell)$ integrates to 1 over the interval $-180^\circ \leq \ell < +180^\circ$. Other catalogs were better modeled by a standard exponential disk model (e.g., see Section 2.2 of Sparke and Gallagher, 2007) of the form

$$L(\ell) = A_\ell \exp\left(\frac{-|\ell - \ell_0|}{h_\ell}\right), \tag{3.4}$$

where the periodic longitude angle is always chosen such that $-180^\circ \leq \ell - \ell_0 < +180^\circ$. The two independent parameters are ℓ_0 and h_ℓ, with the value A_ℓ serving as the normalization. The ℓ_0 parameter represents any necessary offset between the central peak of the distribution and the Galactic center at $\ell = 0^\circ$, and h_ℓ is an angular scale height related to the radial scale height of the Galactic disk. No additional longitude distribution models were considered.

For each class of Galactic sources considered in this work—OCs and SNRs—we used the largest catalog of sources—i.e., OPENCLUST (Dias *et al.*, 2002) and the Green SNRs (Green, 2014, 2017), respectively—for the `dynesty` distribution fitting, since the largest sample is likely to provide the best representation of the true distri-

Table 3.1: Median posterior values for the four parameters in the OC latitude model (Equation 3.2), including the corresponding normalization value. For each parameter, the 68% interval shows the 16th and 84th percentiles of posterior samples.

Parameter	Description	Median Value	68% Interval	Units
b_0	Center offset	-0.349	$[-0.416, -0.284]$	deg
h_{b1}	Scale height 1	1.83	$[1.77, 1.90]$	deg
h_{b2}	Scale height 2	10.1	$[9.51, 10.8]$	deg
f_1	Amplitude fraction	0.950	$[0.943, 0.956]$	—
A_b	Normalization	0.142	$[0.138, 0.146]$	deg^{-1}

bution. Both OPENCLUST and the Green SNRs involve selection effects as discussed in Section 3.3, but these can mostly be overlooked, since our primary goal is to produce a randomized facsimile of *the catalogs themselves*, rather than a fully accurate Galactic model. The best latitude models for both the OPENCLUST data and the Green SNRs data used the double hyperbolic secant given in Equation 3.2, but the best longitude model for the OPENCLUST data was the uniform model of Equation 3.3, while the Green SNRs data was a better match to the exponential disk of Equation 3.4. Figure 3.2 shows how the best distribution models visually compare with the data from all four catalogs using cumulative distribution functions (CDFs) which show the cumulative integrated area of the PDF. The median posterior parameter values for each model as obtained by `dynesty` are presented in Tables 3.1–3.3.

The top two panels of Figure 3.2 show the best-fit models for the OPENCLUST data using Equations 3.2 and 3.3. The largest visible discrepancies occur in the longitude distribution between $\ell \simeq -120°$ and $\ell \simeq +60°$. The OCs listed in OPENCLUST are all visible at optical wavelengths, implying that they are all close enough to still be observable after accounting for interstellar dust extinction. More than 95% of OPENCLUST sources that have tabulated distances are within 6 kpc of Earth, with

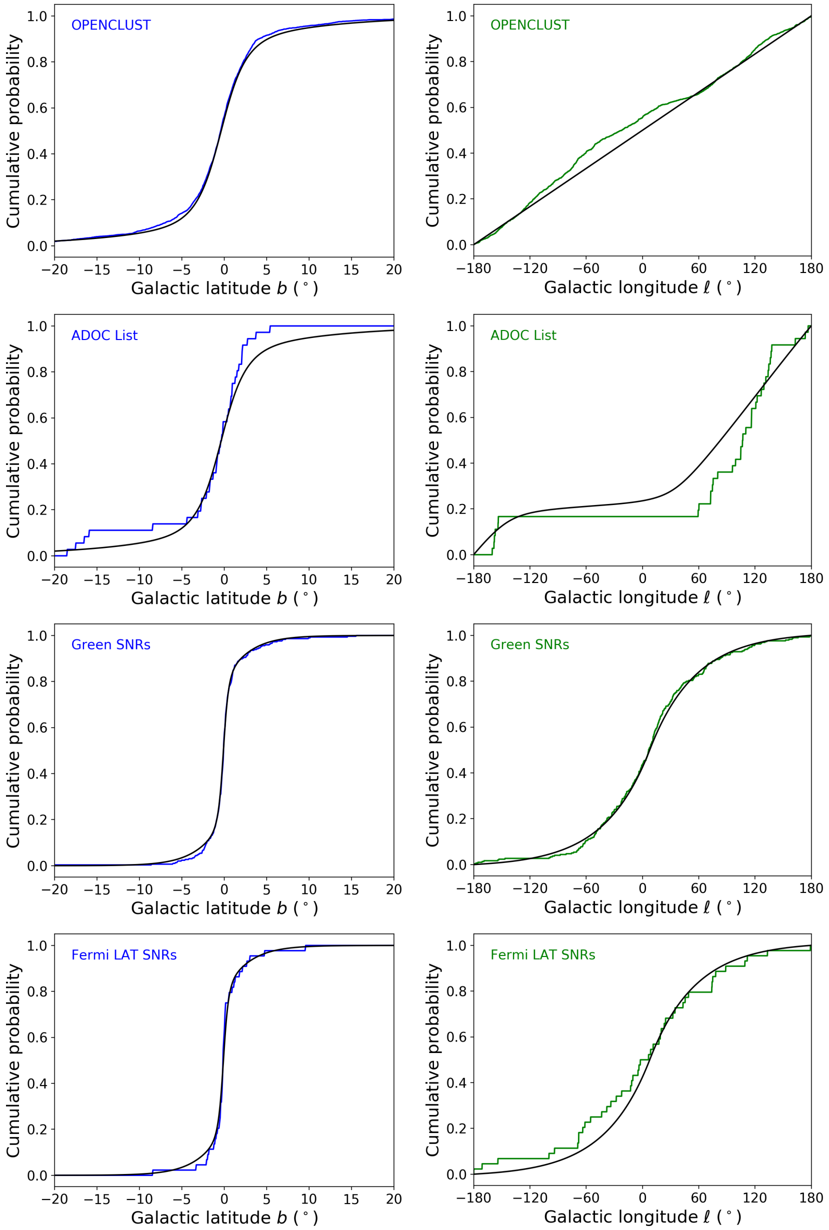

Figure 3.2: Empirical cumulative distribution functions (ECDFs) for each catalog of candidate sources plotted against Galactic latitude (left column, blue lines) and Galactic longitude (right column, green lines). Rows from top to bottom: OPENCLUST (Dias *et al.*, 2002), ADOC list (Odrowski *et al.*, 2013), Green SNRs (Green, 2014, 2017), and Fermi LAT Classified and Marginally Classified SNRs (Acero *et al.*, 2016). The black lines overlaid on each plot show the CDF of the distributions which were used to model the catalog data when generating the null distributions, as described in the text. The horizontal axes of the Galactic latitude plots have been constrained in order to show details near the Galactic plane.

Table 3.2: Same as Table 3.1, but for the SNR latitude model.

Parameter	Description	Median Value	68% Interval	Units
b_0	Center offset	-0.0814	$[-0.124, -0.0383]$	deg
h_{b1}	Scale height 1	0.384	$[0.335, 0.438]$	deg
h_{b2}	Scale height 2	2.58	$[2.28, 2.94]$	deg
f_1	Amplitude fraction	0.921	$[0.899, 0.938]$	—
A_b	Normalization	0.568	$[0.517, 0.625]$	deg^{-1}

Table 3.3: Same as Tables 3.1 and 3.2, but for the SNR longitude model (Equation 3.4).

Parameter	Description	Median Value	68% Interval	Units
ℓ_0	Center offset	7.96	$[5.27, 10.7]$	deg
h_ℓ	Scale height	48.4	$[45.1, 52.1]$	deg
A_ℓ	Normalization	0.0106	$[0.00991, 0.0113]$	deg^{-1}

a thin tail extending out to ~15 kpc. These distances are too short to reveal large-scale asymmetries in the disk structure of the Milky Way, so we expect the longitude distribution to be uniform to first order, with a few discrepancies due to the relative positions of the local spiral arms. Since the ADOC list also consists of Galactic OCs, we expect those 36 OCs to follow the same distribution with some additional scatter due to the small number of objects. One complication here is that the ADOC list consists only of OCs which are north of the celestial equator, so their longitude distribution is uniform, but has a gap between $\ell \simeq -147^\circ$ and $\ell \simeq +33^\circ$ where the Galactic plane dips south of the equator. This issue is addressed by composition of the factorized PDF $F(b, \ell)$ with an additional step distribution PDF that excludes the southern hemisphere. The second row of Figure 3.2 shows an approximation of the resulting longitude CDF with this step distribution filter included—the distribution models are otherwise identical to those used for OPENCLUST.

The third row in Figure 3.2 shows the best models for the Green SNRs data using Equations 3.2 and 3.4. When compared to the OC distributions, there are two important differences for this case. Firstly, the SNR latitude distribution has a narrower spread about the Galactic plane than the OC distribution. Comparing the h_{b1} and h_{b2} values in Tables 3.1 and 3.2, the SNR distribution is narrower by a factor of ∼4–5 in both parameters. This difference is a consequence of the scale heights of young and old stars in the Galactic disk. Stars form in the thin disk, which has a scale height of about 280–350 pc, but older stars diffuse into the thick disk, which has a larger scale height of about 0.75–1 kpc (see, e.g., Section 2.2 of Sparke and Gallagher, 2007). SNRs are the remains of high-mass stars, which live short lives and die before they have time to diffuse into the thick disk, so the SNRs are typically found near stellar formation sites in the thin disk. The second big difference for SNRs is the form of the longitude distribution, which follows an exponential instead of a uniform distribution—there are more SNRs visible when looking towards the Galactic center than away from it (for an in-depth discussion, see Green, 2015). This is because the Green SNR catalog was primarily compiled using observations at radio wavelengths, which detect SNRs via their synchrotron radiation. Since long wavelengths are subject to minimal extinction from interstellar dust, large-scale asymmetries in the star formation activity of the Galactic disk are more apparent. The fourth row of Figure 3.2 shows that the 44 objects from the Fermi LAT Classified & Marginally Classified SNRs catalog also conform to the same distribution whose parameters were obtained from the Green SNRs data. Again, the smaller number of objects produces some additional scatter.

3.5 Results and Discussion

In this section, we present the results of our analyses. For each candidate source set, we present a sky map in Galactic coordinates showing the arrival directions of the IceCube neutrino events (with circularized errors at the 90% confidence level) as well as the positions of the relevant candidate sources. We also include comparative histograms showing the empirical r distribution and the Monte Carlo null distribution of r as described in Section 3.4.1. The null distribution histograms display the averaged distribution over $K = 10^6$ Monte Carlo realizations. We note that negative r values can occur when the most probable arrival direction of a neutrino falls within the angular extent of a candidate source. For our histograms, any $r < 0$ will be rounded up to $r = 0$ and then tabulated in the first bin (covering $0 \leq r < 1$), so that the first bin always represents N_c, the total number of coincidences. In the interest of focusing on neutrinos with small r values, the histograms are truncated to the range $r < 40$. For each analysis, we report ΔN_c, the number of excess coincidences in the empirical r distribution when compared with the averaged null distribution, as well as p_{N_c}, which is the p-value associated with ΔN_c. For each catalog, we also present the complementary results of a K-S test applied to the two histogram distributions, with its p-value denoted by $p_{\text{K-S}}$. For both types of statistical analysis, we choose $\alpha = 0.01$ as our significance threshold—if $p_{N_c} < \alpha$ or $p_{\text{K-S}} < \alpha$, then we will consider the disparity between the empirical and null distributions to possibly be indicative of a causal connection between the candidate sources and the neutrinos.

3.5.1 Open Cluster Analyses

The top two panels of Figure 3.3 show the analysis results for the hypothesis of causal association with the OPENCLUST (Dias *et al.*, 2002) candidate sources. The empirical r distribution has $N_c = 7$ coincidences, which is an excess of $\Delta N_c = 0.7$ coincidences over the averaged null distribution expectation. Table 3.4 gives specific information regarding each of the seven coincidences, as well as the four additional cases in which $r < 3$. While these cases are not coincidences, they are near enough

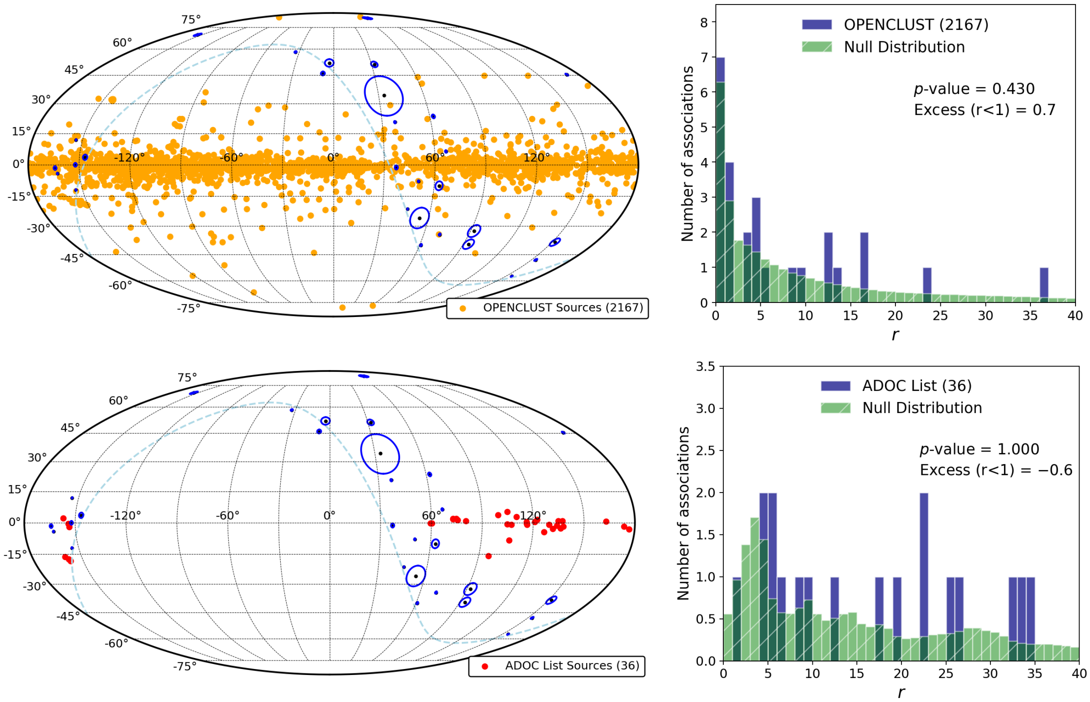

Figure 3.3: *Top left:* Sky map showing the positions of OC candidate sources (orange circles) from OPENCLUST (Dias *et al.*, 2002). Black dots mark the arrival directions of track-like neutrinos (Aartsen *et al.*, 2016), with blue circles showing their circularized angular errors. The dashed light blue line is the celestial equator. *Top right:* Histogram of r values for the analysis of the OPENCLUST sources. The empirical distribution of r values is shown in blue, with the averaged null distribution overplotted in semi-transparent green. See text for details. *Bottom left:* Same as top left, but showing the positions of the 36 ADOCs (Odrowski *et al.*, 2013) instead (red circles). *Bottom right:* Same as top right, but showing r distributions for the ADOCs analysis.

to potentially be of some interest. The fraction of Monte Carlo null distribution realizations which yielded at least seven coincidences by chance was $p_{N_c} = 0.430$, which is far too large to be considered significant at the $\alpha = 0.01$ level. Likewise, a K-S test comparing the two distributions resulted in $p_{\text{K-S}} = 0.973$, suggesting that the empirical r distribution is in excellent agreement with the null distribution.

The two lower panels of Figure 3.3 show the results of our analysis using the ADOC list (Odrowski *et al.*, 2013) with 36 objects. The empirical r distribution did not result in any coincidences at all, in contrast to the averaged null distribution

Table 3.4: List of the eleven track-like neutrino events having $r < 3$ with OPENCLUST (Dias *et al.*, 2002) sources. The dashed line separates coincidences ($r < 1$) from events with $1 < r < 3$. The ν ID and E_ν columns list the IceCube neutrino ID number and energy proxy taken from Table 4 of (Aartsen *et al.*, 2016). The σ_ν column is the circularized 90% confidence level error on the neutrino arrival direction b_ν, ℓ_ν, which is listed in Galactic coordinates. The nearest candidate source is listed with its position b, ℓ, angular radius a, and center-to-center separation S from the neutrino event.

r	ν ID	E_ν (TeV)	σ_ν (°)	b_ν (°)	ℓ_ν (°)	Source	b (°)	ℓ (°)	a (°)	S (°)
0.102	2	250	0.438	−7.93	+50.52	NGC 6837	−8.01	+50.52	0.038	0.083
0.195	26	340	1.276	+3.61	−146.67	NGC 2324	+3.30	−146.55	0.088	0.337
0.364	28	210	0.882	−0.03	−152.21	NGC 2269	+0.30	−152.11	0.025	0.346
0.429	21	670	0.881	−1.61	−164.23	FSR 0940	−1.29	−164.45	0.012	0.389
0.530	6	770	10.248	+34.07	+33.47	Dol Dzim 7	+29.17	+36.29	0.025	5.457
0.597	8	660	0.530	−34.30	+70.61	NGC 7193	−34.28	+70.09	0.108	0.425
0.902	5	230	2.156	−10.13	+62.97	NGC 6938	−10.74	+64.91	0.060	2.005
1.089	9	950	0.340	−12.12	−153.96	NGC 2112	−12.61	−154.13	0.150	0.520
1.202	17	200	1.020	+82.97	+77.71	Latham 1	+84.59	+72.32	0.500	1.726
1.440	10	520	0.961	−1.31	+37.15	NGC 6755	−1.69	+38.60	0.117	1.500
1.996	14	210	5.187	−25.98	+54.33	NGC 7036	−21.44	+64.54	0.033	10.387

Table 3.5: Tabulated details for the one track-like neutrino event having $r < 3$ with an ADOC (Odrowski *et al.*, 2013). Columns are the same as in Table 3.4.

r	ν ID	E_ν (TeV)	σ_ν (°)	b_ν (°)	ℓ_ν (°)	Source	b (°)	ℓ (°)	a (°)	S (°)
1.442	28	210	0.882	−0.03	−152.21	Collinder 106	−0.40	−153.96	0.520	1.791

expectation of ∼0.6 coincidences, so we find $\Delta N_c = -0.6$. Table 3.5 provides a few details for the single case where $r < 3$ in this analysis, which had $r = 1.442$. Since all null distribution realizations will necessarily produce zero or more coincidences, $p_{N_c} = 1.0$ for this analysis. The associated K-S test result was $p_{\text{K-S}} = 0.442$, which also greatly exceeds the significance threshold. In summary, we find no evidence of causal association between the neutrino events and the ADOCs.

It is interesting to note that none of the OPENCLUST coincidences in Table 3.4

involved young OCs: five out of the seven coincident sources have ages of 1 Gyr or older, placing them among the oldest 25% of OPENCLUST sources with tabulated ages. In fact, NGC 7193 (aged 4.47 Gyr) is in the top 2%. The youngest two coincident OCs are NGC 2324 and NGC 2269, both of which still have ages over 200 Myr. All eleven OCs in Table 3.4 are older than the threshold of ∼40 Myr that was used to select the 36 ADOCs (Odrowski *et al.*, 2013). NGC 6755, with $r = 1.440$ and an age of 52 Myr, is the only OC in the table that is younger than 100 Myr.

In addition to being old, the OPENCLUST sources in Table 3.4 are also preferentially nearby, being below the catalog's median distance of 1800 pc for OCs with tabulated distances, with the exception of NGC 2324 (3800 pc) and FSR 0940 (2421 pc). However, the OCs in Table 3.4 are *not* preferentially those having the largest angular sizes. Five of the eleven OCs listed have angular diameters below the catalog median of 5.0 arcmin (radius 0.042°). Those five OCs include FSR 0940, which is among the smallest 10% of OCs with tabulated angular sizes due to its diameter of only 1.4 arcmin (radius 0.012°). Despite being a comparatively small target, FSR 0940 found itself in a coincidence at $r = 0.429$ with neutrino ID 21.

OPENCLUST is such a broad catalog that many objects it includes have not been studied in detail. Typical OCs are rarely mentioned in literature outside of large studies that survey tens to thousands of objects. For instance, a recent study concludes that NGC 7193 and NGC 7036, both of which appear in Table 3.4, are most likely to be asterisms (Cantat-Gaudin and Anders, 2020). While their stars appear in the same direction on the sky, they do not form a convincing cluster in either parallax or proper motion space, so they are not likely to be physical clusters of gravitationally bound stars with a common origin. The status of NGC 6837 is similarly dubious (Krone-Martins *et al.*, 2010). None of these eleven OCs have been explicitly considered as potential neutrino sources in past literature.

While the ADOC analysis produced no coincidences, there is one case of $r < 3$ documented in Table 3.5. The relevant ADOC, Collinder 106, is among the 10 ADOCs that are within the Local Arm of the Galaxy, and it has a larger angular size (radius 0.52°) than two-thirds of the ADOCs. The OC is located in the Monoceros Loop within the larger Monoceros star-forming region (Costado and Alfaro, 2018). It has also been proposed that Collinder 106 is associated with the gamma-ray pulsar J0633+0632 (Danilenko *et al.*, 2020). The COCD, which the ADOCs were selected from, lists Collinder 106 with an age estimate of 5.50 Myr, which would place it among the youngest 25% of ADOCs. However, the same source is also cataloged in OPENCLUST, where it has a dramatically different age estimate of 7.94 Gyr. This inconsistency suggests the need for further study of this object.

There are also trends among the track-like neutrino events that appear in Tables 3.4–3.5. Neutrino ID 28 appears in both tables, which may be due in part to the fact that it is the closest of the 29 neutrino events to the Galactic plane ($b_\nu = -0.03°$). This same event also has one of the lowest energy proxies in the IceCube data set—all of the track-like events were selected to have energies of at least 200 TeV, and ID 28 with $E_\nu = 210$ TeV is close to that threshold. Neutrino IDs 10, 21, and 26 (which all appear in Table 3.4) are the next closest events to the Galactic plane, with $|b_\nu| < 4°$ for their most probable arrival directions. The closest coincidence in the OPENCLUST analysis (Table 3.4) is neutrino ID 2 at $r = 0.102$ from NGC 6837. ID 2 is within 10° of the Galactic plane and also has a small energy proxy at $E_\nu = 250$ TeV. The only neutrino event appearing in either Table 3.4 or Table 3.5 that has $|b_\nu| > 35°$ is ID 17. At $b_\nu = 82.97°$, it is the farthest of the 29 neutrino events from the Galactic plane, making its near-coincidence with an OC something of an unusual result. We also note that neutrino ID 6, which has an OPENCLUST coincidence (Dol Dzim 7) in Table 3.4, has the largest circularized error among the 29 neutrinos at $\sigma_\nu = 10.248°$.

The correspondingly large area that its error ellipse covers on the sky increases the likelihood of its involvement in chance coincidences.

3.5.2 Supernova Remnant Analyses

The top sky map and histogram in Figure 3.4 show the analysis results when using the Green SNRs catalog (Green, 2014, 2017) as the list of candidate sources. There were $N_c = 3$ coincidences in the empirical r distribution, yielding an excess of $\Delta N_c = 2.0$ over the null expectation of only about 1.0 coincidence. The three coincidences are listed with details in Table 3.6 along with two additional cases where $r < 3$. The p-value was $p_{N_c} = 0.018$, which is close to being significant at the threshold level of $\alpha = 0.01$. Alternatively, the result of a K-S test comparing the two distributions was $p_{\text{K-S}} = 0.444$, which leads us to conclude that this case is also consistent with a null distribution.

The lower sky map and histogram in Figure 3.4 show the analysis results for the Fermi LAT Classified and Marginally Classified SNRs (Acero *et al.*, 2016). The number of coincidences present was $N_c = 1$, which is an excess of $\Delta N_c = 0.7$ over the null distribution expectation. The one coincidence is detailed in Table 3.7, as is one other case of $r < 3$ occurring in this analysis. The fraction of null distribution iterations producing at least one coincidence was $p_{N_c} = 0.243$, which is well above the threshold. The K-S test result of $p_{\text{K-S}} = 0.699$ for the two distributions similarly indicates consistency between the data and the Monte Carlo null case.

A noteworthy detail in regards to these SNR results is that the associated candidate sources are preferentially those that cover larger areas on the sky, which is suggestive of chance coincidences. The median circularized angular diameter of the entire catalog of Green SNRs is 17 arcmin (radius 0.14°). Of the six total SNRs appearing in Tables 3.6–3.7 (G205.5+0.5 appears twice), all have circularized angular

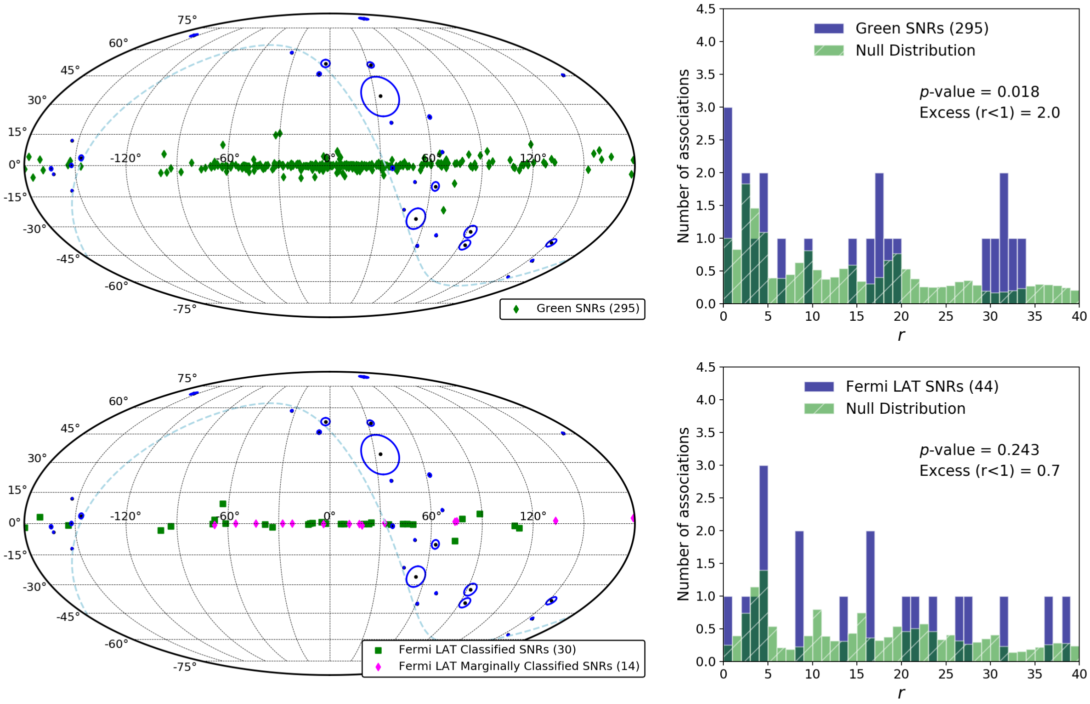

Figure 3.4: *Top left:* Same as sky maps in Figure 3.3, but showing positions of the 295 Green SNRs (Green, 2014, 2017) with green diamonds. *Top right:* Same as histograms in Figure 3.3, but showing the relevant r distributions for the Green SNRs analysis. *Bottom left:* Sky map of the 44 Fermi LAT Classified and Marginally Classified SNRs (Acero *et al.*, 2016). Classified SNRs are indicated with green squares, and marginally classified SNRs are indicated with magenta diamonds. *Bottom right:* Histogram of r distributions for the Fermi LAT SNRs analysis.

Table 3.6: List of the five track-like neutrino events having $r < 3$ with Green SNRs (Green, 2014, 2017). The dashed line separates coincidences ($r < 1$) from events with $1 < r < 3$. Columns are the same as in Table 3.4.

r	ν ID	E_ν (TeV)	σ_ν (°)	b_ν (°)	ℓ_ν (°)	Source	b (°)	ℓ (°)	a (°)	S (°)
−1.116	24	850	0.555	+6.42	+66.66	G65.3+5.7	+5.66	+65.18	2.273	1.654
0.270	28	210	0.882	−0.03	−152.21	G205.5+0.5	+0.21	−154.27	1.833	2.072
0.649	10	520	0.961	−1.31	+37.15	G36.6−0.7	−0.69	+36.59	0.208	0.832
2.140	26	340	1.276	+3.61	−146.67	G213.0−0.6	−0.36	−146.69	1.247	3.977
2.444	14	210	5.187	−25.98	+54.33	G70.0−21.5	−21.54	+70.03	2.345	15.023

Table 3.7: List of the two track-like neutrino events having $r < 3$ with Fermi LAT SNRs (Acero *et al.*, 2016). The dashed line separates the coincidence ($r < 1$) from the event with $1 < r < 3$. Columns are the same as in Table 3.4. Both candidate sources appearing in this table are listed among the 30 classified SNRs in (Acero *et al.*, 2016) (as opposed to the 14 marginally classified SNRs).

r	ν ID	E_ν (TeV)	σ_ν (°)	b_ν (°)	ℓ_ν (°)	Source	b (°)	ℓ (°)	a (°)	S (°)
−0.276	28	210	0.882	−0.03	−152.21	G205.5+0.5	−0.82	−154.09	2.280	2.037
2.410	10	520	0.961	−1.31	+37.15	G34.7−0.4	−0.44	+34.66	0.310	2.627

sizes larger than the median, and four of the six are among the largest 5% of objects in the Green SNR catalog. In particular, G70.0−21.5 is actually the largest Green SNR in the catalog, having a circularized angular diameter of 280 arcmin (radius 2.3°). Interestingly, the same SNR also has the distinction of being located at $|b| = 21.5°$ from the Galactic plane, which is the most extreme Galactic latitude of any Green SNR.

One more notable result is the appearance of G34.7−0.4 in the Fermi LAT SNRs analysis (Table 3.7). Better known as W44, this source is one of two SNRs whose gamma-ray spectra were found to display a characteristic pion-decay signature, providing evidence of cosmic ray proton acceleration in SNRs (Ackermann *et al.*, 2013). This SNR also appears to be interacting with nearby molecular clouds (Claussen *et al.*, 1997; Chevalier, 1999). At $r = 2.410$, our analysis does not show a coincidence involving this object, but W44 is not the only SNR in Tables 3.6–3.7 to have been previously considered as a cosmic ray accelerator. The coincident SNR G65.3+5.7 has been considered as a potential cosmic ray accelerator in the past (e.g., Kobayashi *et al.*, 2004; Delahaye *et al.*, 2010), but it is suspected to be a *leptonic* cosmic ray source, which would be inconsistent with the pion-decay model for production of high-energy neutrinos. G205.5+0.5 has also been studied as a particle accelerator candidate (e.g., Fiasson *et al.*, 2008), as well as for possible interactions with the nearby Rosette Nebula (e.g., Delahaye *et al.*, 2010; Xiao and Zhu, 2012; Su *et al.*, 2017). G213.0−0.6 is also a candidate for interaction with molecular clouds in its proximity (e.g., Su *et al.*, 2017).

Both of the SNR analyses found a coincidence between neutrino ID 28 and the candidate source G205.5+0.5, also known as the Monoceros Nebula, Monoceros Loop, or Monoceros SNR. Of the five SNRs appearing in Table 3.6 for the Green SNRs analysis, G205.5+0.5 is the only one to appear in the Fermi LAT SNRs catalog (Acero *et al.*, 2016) as either a classified or marginally classified SNR. The gamma-ray source detected by Fermi LAT above 1 GeV has an apparent angular radius of ~2.3°, nearly 30% larger than the ~1.8° radius observed in the radio (Acero *et al.*, 2016), which accounts for most of the difference in r values observed between our two analyses. The gamma-ray source is also offset slightly in the direction of the Rosette Nebula (Acero *et al.*, 2016), which slightly reduces the separation angle S between it and the neutrino arrival direction. Since the publication of Acero *et al.* (2016), there has also been a detailed analysis of the GeV morphology of this SNR by Fermi LAT which concluded that the decay of neutral pions could explain the observed gamma-ray emission (Katagiri *et al.*, 2016).

As with the OC analyses, we close this discussion by examining trends in the track-like neutrino events that appear in Tables 3.6–3.7. Neutrino ID 28 is notable for having appeared in all four analyses, coincident with G205.5+0.5 in both SNR analyses, coincident with NGC 2269 in the OPENCLUST analysis, and having $r = 1.442$ with Collinder 106 in the ADOC analysis. Also notable is neutrino ID 10, which appears in three out of four analyses, though only in the Green SNRs analysis (Table 3.6) was it close enough to a candidate source to have a coincidence (SNR G36.6−0.7). In the Fermi LAT SNRs analysis (Table 3.7), ID 10 was associated with a different SNR and only at $r = 2.410$. Neutrino IDs 26 and 14 also appeared in more than one analysis—both appeared in the OPENCLUST analysis (Table 3.4), though only ID 26 had a coincidence (NGC 2324), and both appeared without coincidences in the Green SNRs analysis (Table 3.6). We note again that neutrino IDs 28, 10, and 26 all have arrival directions within 4° of the Galactic plane, which makes chance coincidences with Galactic candidate sources more likely. In a similar vein, neutrino ID 14 has the second-largest circularized neutrino error at $\sigma_\nu = 5.187°$. The closest coincidence in the Green SNRs analysis (Table 3.6) was neutrino ID 24, which has $r = -1.116$ with SNR G65.3+5.7 and appears in no other analyses. ID 24 is still within 10° of the Galactic plane, and is unusual in that it has one of the highest energy proxies in the track-like neutrino data set at $E_\nu = 850$ TeV.

3.6 Conclusions

Neutrino astronomy is a growing field which is expected to help illuminate the origins of cosmic rays above the knee and provide insights into the physical mechanisms powering their accelerators. As the field matures, diverse approaches are being developed to address questions regarding the origins of the high-energy neutrinos observed by IceCube. One fundamental question to be answered is that of a possible Galactic component, i.e., whether there exists some non-negligible fraction ($\gtrsim 5\%$) of the neutrino flux which can be attributed to the Milky Way.

In our previous work (Emig *et al.*, 2015; Lunardini *et al.*, 2019), we adopted the "nearest neighbor" method to search for positional associations (or *coincidences*) of IceCube neutrino events with candidates from specific classes of extragalactic astronomical objects. In the present paper, we developed this method further in order to accommodate candidate neutrino sources that are not uniformly distributed across the sky. This new version of the method was applied to search for IceCube track-like neutrino coincidences with specific classes of Galactic objects, namely open clusters

(OCs) and supernova remnants (SNRs). As in the past, we assess the compatibility of our results with the null hypothesis of no causal relationship using Monte Carlo randomization and Kolmogorov-Smirnov tests.

In particular, this work presents the first statistical analysis of Galactic OCs as candidate neutrino sources. Using a catalog of 2,167 OCs observed at optical wavelengths (Dias *et al.*, 2002), seven coincidences were found, a result that is statistically consistent with the null case. The overall distribution of the r parameter, which represents the normalized angular distance from a neutrino to the nearest candidate source, is consistent with the null hypothesis as well. The analysis was then repeated with a restricted set of 36 Galactic "accelerator-dominated" open clusters (ADOCs) (Odrowski *et al.*, 2013) which were identified as likely neutrino producers on theoretical grounds. Zero coincidences were found and the overall r distribution was again consistent with the null hypothesis.

We have identified the coincident neutrino events and OCs appearing in both of these analyses (Tables 3.4–3.5). It is interesting to note that our results defy the physical motivations that were used to select the 36 ADOCs—none of the ADOCs were coincident with a neutrino event, and the coincident objects from the larger OC catalog were far older than the ADOC age threshold of $\sim$40 Myr. This fact can perhaps be regarded as secondary confirmation that the coincidences are consistent with random chance. While at this time there is no evidence that these OCs are Galactic high-energy neutrino sources, they might be worth further monitoring in the future.

In our analysis of Galactic SNRs, we found three coincidences between neutrinos and the 295 objects in Green's catalog (Green, 2014, 2017), the most complete catalog of Galactic SNRs available. This result was only narrowly consistent with the null case, but the overall distribution of the r parameter was in good agreement the null hypothesis expectation. As with the Galactic OC analysis, we also took the opportunity to investigate a smaller set of SNRs which were selected to be more likely neutrino sources. When restricting our analysis to 44 SNRs observed in gamma rays by Fermi LAT (Acero *et al.*, 2016), only one coincidence was found, and again the final results were consistent with the null hypothesis.

In Tables 3.6–3.7 we have identified those neutrino events and SNRs which produced coincidences in each SNR analysis. Once again, we find that the results are in tension with the scenario of hadronic neutrino production, in which we expect gamma-ray counterparts due to π^0 decay. G205.5+0.5 was the only SNR in the Fermi LAT catalog found to produce a coincidence in our analyses. The other coincident SNRs from Green's catalog have not been detected at gamma-ray energies. Our SNR results are overall consistent with the null results from other works, in particular the stacking analysis performed by the IceCube collaboration using 7 years of data (Aartsen *et al.*, 2017e), where p-values of 0.25 and higher were obtained for three different sets of 4–10 SNRs each. Those SNRs were selected based on age and TeV gamma ray observation, and were sorted into sets based on environment (e.g., molecular cloud, pulsar wind nebula).

More broadly, our Galactic neutrino findings are compatible with the general conclusion of the IceCube Collaboration that less than 14% of the astrophysical flux is due to Galactic sources(Aartsen *et al.*, 2017e). Across our four analyses, we found a total of 11 coincidences involving 9 unique neutrino events from the data set of 29 track-like neutrinos (Aartsen *et al.*, 2016). If we assume that all these neutrinos are of Galactic origin, then we can estimate the Galactic component due to OCs and SNRs at $9/29 \sim 31\%$. This assumption is too generous to be realistic, but it does provide a qualitative upper limit.

Future data from IceCube will likely yield improved limits on the Galactic component. More direct measurements of the exact fraction may also be forthcoming once sufficient statistical power is available. This would also allow greater scrutiny into the question of which types of Galactic sources are most responsible for the neutrino flux. However, if the Galactic component is found to be negligible, this would also have important implications for Galactic OCs and SNRs, which are theoretically well-motivated as particle accelerators. The lack of any observable Galactic neutrino flux would certainly warrant a theoretical investigation.

Chapter 4

DEPENDENCE OF SIMULATED SUPERNOVA YIELDS ON EXPLOSION MORPHOLOGY

4.1 Abstract

Both observed supernova remnants and many modern supernova models have explosion morphologies that deviate significantly from simple spherical symmetry. These variations can have significant consequences for supernova nucleosynthesis via their effects on the burning conditions in the explosion, but their influence is still not fully understood. To examine the results of asymmetries in supernova explosions, we employ supercomputer simulations of supernovae in three dimensions using the SNSPH code, with additional post-processing used to predict total and spatially mapped yields over a network of 524 isotopes. We impose initial asymmetries on the explosions, in order to present comparative analysis and visualizations of the yields produced in models with spherically symmetric, unipolar, and bipolar geometries for 15- and 20-solar-mass progenitors. Of particular interest, we examine how small changes in the peak temperatures and densities experienced by the supernova ejecta can influence the production of the radioisotopes ^{44}Ti and ^{56}Ni in α-rich freezeout conditions. Emission lines from the decay of these isotopes are observed in Cassiopeia A and other supernova remnants, so our simulations may be able to shed light on the conditions that existed in the midst of these real explosion events.

4.2 Introduction

The inclusion of imposed asymmetries in models of core-collapse supernovae is now a common method for explaining observations of features present in supernova remnants. For instance, asymmetric explosion models with global jet-like, equatorial, or single-lobe morphologies were necessary in order to explain the amount of mixing observed in SN 1987A (Hungerford *et al.*, 2003, 2005). These sorts of large-scale asymmetries can be the result of pre-existing convective imbalances in the progenitor star, angular momentum of stellar rotation, or the supernova engine mechanism itself. Similar pursuits were what led to the development of the convective supernova engine, where neutrino-driven convection in the region above the proto-neutron star revives the supernova shock and imprints low-mode asphericities on the explosion (Herant and Benz, 1991, 1992; Colgate *et al.*, 1993; Herant *et al.*, 1994). These asphericities are intrinsic to the supernova engine itself (Fryer *et al.*, 2017), and it has been argued that such intrinsic effects are equally important for mixing when compared with extrinsic influences like interactions of ejecta with the circumstellar medium (Ellinger *et al.*, 2013). Interactions with the surrounding medium can produce reverse shocks and Rayleigh-Taylor (RT) instabilities, as can steep entropy gradients within the progenitor star, but the supernova engine seeds the instabilities from the start. RT instabilities produce mushroom- and finger-shaped structures in the ejecta at angular scales of no more than 10–15°, as opposed to large-scale global asphericities. The full extent to which any of these effects can influence the explosion is not yet well understood, especially as applied to nucleosynthetic yields.

Intrinsic explosion asymmetries can cause further asymmetries to develop in the supernova reverse shock, and they arguably have a stronger effect on yield asymmetries than extrinsic factors do. When asphericities in the supernova engine produce large-scale angular asymmetries in the explosion, even pockets of material that begin at the same radial position in the progenitor star can experience drastically different thermodynamic trajectories (Fryer *et al.*, 2005). Full dimensionality in supernova models is important for capturing many of these effects, since lower-dimensional models can produce unrealistic convection effects that artificially affect the explosion results (Radice *et al.*, 2018). In addition, Young and Fryer (2007) showed that 1D supernova models can be made to produce non-unique yields. There is a necessity to explore the uncertainties encountered in 3D supernova models, and to evaluate how asymmetries in these models affect yields predictions. Some other recent work exploring nucleosynthesis in the context of asymmetric supernovae includes Orlando *et al.* (2016), Janka *et al.* (2017), and Grimmett *et al.* (2018).

In relatively nearby supernova remnants, detailed observations of spatially resolved yields are available. The supernova remnants Cassiopeia A (Cas A) and G292.0+1.8 (G292) have one- and half-megasecond observations respectively from the Chandra X-ray Observatory (Hwang *et al.*, 2004; Park *et al.*, 2007) and massive amounts of other observational data from radio to gamma ray wavelengths. Emission from nuclear decay lines of ^{44}Ti in Cas A has been imaged by NuStar (Grefenstette *et al.*, 2017). These NuStar observations, combined with measurements of Fe from Chandra, provide a sensitive diagnostic of the thermodynamic conditions under which explosive burning took place, and therefore insight into the explosion mechanism. As both detailed observations and 3D simulations become more common, the possibilities for producing predictive yields and quantifying yield uncertainties in supernova models will expand.

Here, we present the results of several fully 3D hydrodynamic simulations of core-collapse supernova explosions. Our models include two stellar progenitors, and we utilize a variety of symmetric and asymmetric initialization schemes. In post-processing, we produce detailed nucleosynthetic yields for our models, and use these to visualize the spatial distribution of isotopes in the ejecta. By comparing our models to each other, and to observations of spatially-mapped yields in supernova remnants, we endeavor to isolate some of the variations in yields that are the results of asymmetries. In Section 4.3, we explain the computational methods used in our simulations and provide a complete list of our explosion models. In Section 4.4, we present the results of our models and compare the differing yields observed for the same stellar progenitors using different explosion initializations. Finally, Section 4.5 contains a continued discussion of the results, the production of important short-lived radionuclides, and plans for future work.

4.3 Methods

4.3.1 Computational Methods

All stellar progenitors used for this study were non-rotating, solar-metallicity models evolved from the pre-main sequence up to the point of core collapse using the TYCHO one-dimensional stellar evolution code (Young and Arnett, 2005). TYCHO is a 1D stellar evolution code with a hydrodynamic formulation of the stellar evolution equations. It uses OPAL opacities (Iglesias and Rogers, 1996; Alexander and Ferguson, 1994b; Rogers and Nayfonov, 2002), a combined OPAL and Timmes equation of state (HELMHOLTZ) (Timmes and Arnett, 1999; Rogers and Nayfonov, 2002), gravitational settling (diffusion) (Thoul *et al.*, 1994), general relativistic gravity, time lapse, curvature, automatic rezoning, and an adaptable nuclear reaction network with a sparse solver. A 177 isotope network terminating at ^{74}Ge was used for these calculations. The network uses the latest REACLIB rates (Rauscher *et al.*, 2000; Angulo *et al.*, 1999; Iliadis *et al.*, 2001; Wiescher *et al.*, 2006), weak rates from Langanke and

Martínez-Pinedo (2000), and screening from Graboske *et al.* (1973). Neutrino cooling from plasma processes and the Urca process is included. Mass loss uses a choice of updated versions of the prescriptions of (Kudritzki *et al.*, 1989) or prescriptions based on Vink *et al.* (2001); Mokiem *et al.* (2007) for OB mass loss, Bloecker (1995) for red supergiant mass loss, and Lamers and Nugis (2002) for WR phases. It incorporates the 321D description of turbulent convection (Meakin and Arnett, 2007; Arnett *et al.*, 2009, 2010; Arnett and Meakin, 2011; Arnett and Moravveji, 2017), which is based on three-dimensional, well-resolved simulations of convection sandwiched between stable layers, which were analyzed in detail using a Reynolds decomposition into average and fluctuating quantities and projected down to 1D secularly evolving average behavior. It has no free convective parameters to adjust, unlike mixing-length theory. The inclusion of these processes, which approximate the integrated effect of dynamic stability criteria for convection, entrainment at convective boundaries, and wave-driven mixing, results in significantly larger extents of regions processed by nuclear burning stages.

Once the progenitor stars had reached core collapse, a one-dimensional Lagrangian code was then used to model the continuation of the collapse up through the core bounce (Herant *et al.*, 1994; Fryer, 1999). This code for modeling the ignition of the supernova includes three-flavor neutrino transport using a flux-limited diffusion calculation and a coupled set of equations of state in order to model the wide range of densities encountered in the collapse phase. To follow the energy generation in this phase, the code uses a limited network of 14 isotopes (Benz *et al.*, 1989), which is sufficient for modeling the start of the explosion in one dimension. Once the supernova shock was revived and had moved beyond the iron core into the first silicon-sulfur rich shell, the 1D model was mapped into a three-dimensional smoothed particle hydrodynamics (SPH) model. SPH models have some inherent scatter in the pressure and density conditions, but convection in burning shells before and during stellar collapse produces density perturbations of order 10% (Arnett and Meakin, 2011). This is larger than the mapping scatter and comparable to or larger than hydrodynamic instability seed perturbations used in grid codes (Ellinger *et al.*, 2012). Velocity scaling (see Section 4.3.2) was imposed on the models during the 3D mapping to seed asymmetries.

We used the supernova smoothed particle hydrodynamics (SNSPH) code (Fryer *et al.*, 2006) to follow the long-term evolution of the supernova explosion and remnant. SNSPH is a particle-based algorithm and is derived from the version of SPH developed by Benz (1984, 1988, 1990). SNSPH uses adaptive time steps and variable particle scale lengths, and is designed to be run in parallel for speed of computation. The radiation transport for SNSPH is modeled with a two-dimensional, explicit flux-limited diffusion scheme (Herant *et al.*, 1994) adapted to three dimensions. The scheme considers the transport of three neutrino flavors (electron, electron antineutrino, and all others) by summing the flux of neutrinos into and out of an SPH particle weighted by average energy. Outside of a "trapping radius" neutrinos are essentially in the free-streaming regime, and a light bulb approximation is used.

The SNSPH code makes use of a limited nuclear reaction network of 20 isotopes to expedite the energy calculations for the hydrodynamics. The network terminates at ^{56}Ni and neutron excess is directed to ^{54}Fe. The network runs in parallel to the hydrodynamics calculations, and features its own time step sub-cycling algorithm in order to not slow down the hydrodynamics. Changes in energy and composition are fed back into the SPH calculation at each SPH time step. This scheme accurately models the energy production during explosive burning to within 20%.

In order to obtain more accurate nucleosynthetic data, the thermodynamic trajectories of the particles were post-processed using the Burnf code (Young and Fryer, 2007). Burnf employs the same architecture and micro-physics as TYCHO and SNSPH, and has a flexible network. This work is focused on comparisons with species readily observable in supernova remnants. With this aim, it was possible to economize on processor time by using a moderately-sized network. Calculations here used a 524-isotope network complete up to ^{99}Tc, which provides accurate yields up through the weak s-process. Reverse rates are calculated from detailed balance and allow a smooth transition to a nuclear statistical equilibrium (NSE) solver at temperatures exceeding 10^{10} K. Neutrino cooling from plasma processes and the Urca process is calculated. For this work, Burnf chooses an appropriate time step based on the rate of change of abundances and performs a log-linear interpolation in the thermodynamic trajectory of each zone in the explosion calculation. The initial abundances are those of the 177 nuclei in the TYCHO stellar model. Only particles that reached temperatures over 2×10^8 K were post-processed. The individual particle yields from post-processing with Burnf were recombined with the particle temporal and spatial information for analysis and visualization.

4.3.2 Simulations

We ran a total of seven supernova simulations for two progenitor star models with different imposed explosion asymmetries. The progenitors were 15 and 20 $M_\odot$non-rotating, solar composition stars. Both stars were red supergiants at the time of explosion. The radii and masses at the end of the evolution were 7.01×10^{13} cm and 12.12 $M_\odot$ for the 15 $M_\odot$ progenitor and 8.23×10^{13} cm and 10.21 $M_\odot$ for the 20 $M_\odot$ progenitor due to extensive mass loss. Asymmetries were implemented by modifying the velocities of particles in and inside of the shock according to the prescription in

Table 4.1: Simulation Models

Model Name	Progenitor Mass	Explosion Asymmetry	Other Notes
15M_sym	15 $M_\odot$	none	—
15M_bip	15 $M_\odot$	bipolar 2:1	$v_{\text{polar}}/v_{\text{equator}} = 2$
15M_dco	15 $M_\odot$	none	1.35 $M_\odot$ compact object
20M_sym	20 $M_\odot$	none	—
20M_bip	20 $M_\odot$	bipolar 2:1	$v_{\text{polar}}/v_{\text{equator}} = 2$
20M_equ	20 $M_\odot$	equatorial 2:1	$v_{\text{equator}}/v_{\text{polar}} = 2$

Hungerford *et al.* (2003), namely

$$v_{\text{radial}} = \left(\alpha + \beta\frac{|z|}{r}\right) v_{\text{radial}}^{\text{sym}} \tag{4.1}$$

for the "jet-like" scenarios, and

$$v_{\text{radial}} = \left(\alpha - \beta\frac{|x|}{r}\right) v_{\text{radial}}^{\text{sym}} \tag{4.2}$$

for the equatorial scenario, where the values for α and β were chosen to produce 2:1 velocity asymmetries. The parameters and imposed asymmetries for all of our models are presented in Table 4.1. This scheme achieves the desired geometry for the supernova but roughly conserves kinetic energy. All explosions were approximately 10^{51} ergs. The simulation 15M_dco was modeled with a non-fixed central compact object of initial mass 1.35 $M_\odot$ that accreted momentum and mass from in-falling material. It included no other imposed asymmetries.

4.4 Results

The primary focus of this work is to establish the variation in bulk yields introduced by variations in supernova explosion morphology. We will be comparing bulk explosion yields calculated for each of the seven supernova models described in Section 4.3.2. Variations due to asymmetry can be assessed by comparing the three models of each progenitor mass to one another. The degree to which asymmetry effects are uniform across mass can be assessed by comparing the symmetric and bipolar models for each progenitor mass to those of the other mass.

After the completion of all simulations with SNSPH and nuclear post-processing with Burnf, the results entered a data mining pipeline managed by several smaller pieces of code that extracted, sorted, and assembled the binary data into useful formats for plotting and analysis. Selected SPH plots of the final spatial distribution of yields are included in Sections 4.4.1–4.4.2. These SPH plots show the composition and distribution of material at the final time step of the simulations. The plots were rendered using the SPLASH smoothed particle hydrodynamics visualization tool (Price, 2007).

Of the large network of isotopes provided by the Burnf code, we focused our analysis on a smaller subset of significant nucleosynthetic products. The nuclei we inspected included the most common isotopes of helium, carbon, oxygen, neon, sodium, magnesium, aluminum, silicon, sulfur, phosphorous, argon, potassium, calcium, titanium, iron, and nickel. Many of these elements are alpha products, where a common isotope is formed by simply joining several ^{4}He nuclei together. Alpha products serve as important signposts of nucleosynthesis over the course of the star's lifetime and the duration of the supernova explosion. The isotopes ^{44}Ti and ^{56}Ni are of interest in understanding the supernova explosion mechanism. High-energy emission lines from the decay of ^{44}Ti can be detected in young remnants, and ^{56}Ni can be inferred from the brightness of the supernova or the total Fe abundance observed in the remnant (e.g., Grefenstette *et al.*, 2017). To make the data more manageable and curb small numerical errors, we plot only those SPH particles whose mass fractions of the relevant nuclei exceed one part in 10^6.

In addition to determining isotopic abundances for each individual SPH particle, we also recorded the peak temperature experienced by each particle over the length of the simulation, as well as its density at the time of peak temperature. The peak temperature and associated density are diagnostics of nucleosynthetic conditions in supernova explosions; they influence nuclear reaction rates, especially for the products of α-rich freezeouts, where rapidly changing conditions terminate nuclear reactions before NSE can be reached. Production of ^{44}Ti and ^{56}Ni and their resulting ratio can be very sensitive to peak temperatures, peak densities, and lepton fraction in the explosion (Magkotsios *et al.*, 2010), so we expect this ratio to be spatially correlated with these conditions. High-energy emission lines from the decay of ^{44}Ti can be detected in young remnants. Under the assumption that most Fe-rich material originating in the interior of the remnant are dominated by ^{56}Fe from ^{56}Ni decay, the geometry of ^{56}Ni production and abundance relative to ^{44}Ti can be inferred (e.g., Grefenstette *et al.*, 2017).

4.4.1 15 $M_\odot$ Models

Of our four 15 $M_\odot$ models, there is one spherically symmetric explosion (15M_sym), one bipolar explosion (15M_bip), and one explosion with a non-fixed compact object accreting material (15M_dco). The full yields from these explosions for all 524 isotopes in the Burnf network can be found in Tables B.1–B.3. A visual summary of the bulk yields produced in these three models for $Z < 35$ can be seen in Figure 4.1 (left). The mass fractions of the yields relative to the spherically symmetric model 15M_sym are shown in Figure 4.1 (right) to highlight differences between the models. The observed differences represent the effects of the imposed asymmetries in the models.

There are only minor differences in yields for the bipolar and spherically symmetric

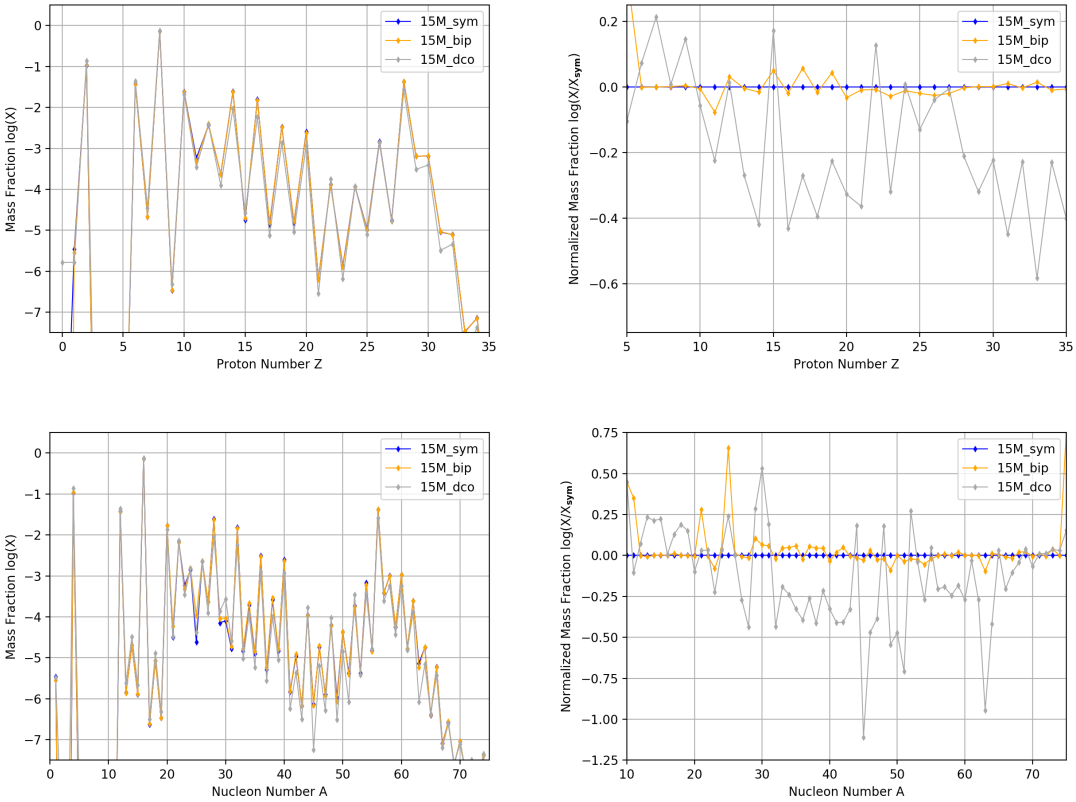

Figure 4.1: Comparative line plots of the yields for all four 15 $M_\odot$ models. Blue indicates the symmetric model 15M_sym, green indicates the bipolar model 15M_bip, and yellow indicates the dynamic compact object model 15M_dco. *Top left:* Mass fractions of total yields produced in the 15 $M_\odot$ models, plotted by element up to proton number $Z = 35$. Note that $Z = 0$ indicates free neutrons. *Top right:* Same data as top left, but normalized to the yields of the symmetric model 15M_sym. *Bottom left:* Mass fractions of total yields for the 15 $M_\odot$ models, plotted by nucleon number up to $A = 75$. *Bottom right:* Same data as bottom left, but normalized to the yields of the symmetric model.

explosions. For a 15 $M_\odot$ star, most of the material outside the iron core escapes with the moderate explosion energy used in these simulations. With a 2:1 velocity asymmetry, the difference in thermodynamic history inside and outside the fast ejecta has only a small effect on explosive burning. This effect features most prominently in the carbon/neon burning shell that reaches near-explosive conditions (Young *et al.*, 2009).

The yields of the 15M_dco model with the dynamic compact object differ noticeably from the first two models, and this is primarily due to the influence of the compact object. This model has additional fallback onto the compact object when compared to the 15M_sym and 15M_bip simulations using fixed inner boundary conditions, and the neutron-rich material and free neutrons brought up by the resulting convection had a significant influence on the yields. The advected neutron-rich isotopes manage to appear in the supernova ejecta despite the large amount of fallback that occurred. In most cases, the species with large differences relative to the baseline spherically symmetric explosion are odd-Z nuclei that have a low starting abundance, so small absolute changes are highlighted on a normalized plot. The prominent spike at $Z = 15$ for the 15M_dco model shows a difference in the abundance of phosphorous that is more a result of computation than of physics. It reflects an excess of ^{30}P, a short-lived isotope ($t_{1/2} \approx 2.5$ min) which decays to stable ^{30}Si. The burning calculation for the 15M_dco model was terminated at an earlier time than for the 15M_sym model, so fewer atoms of ^{30}P have time to decay. The same effect may also contribute to the relative deficit of silicon at $Z = 14$ for the 15M_dco model.

The most salient feature of the 15M_dco nucleosynthesis is the strong signature of α-rich freezeout in the inner convective region driven by motion of the compact object. Figure 4.2 (left) shows the ^{4}He abundance in a cross section of the simulation, rendering the freezeout regions easily identifiable. Elements heavier than silicon are

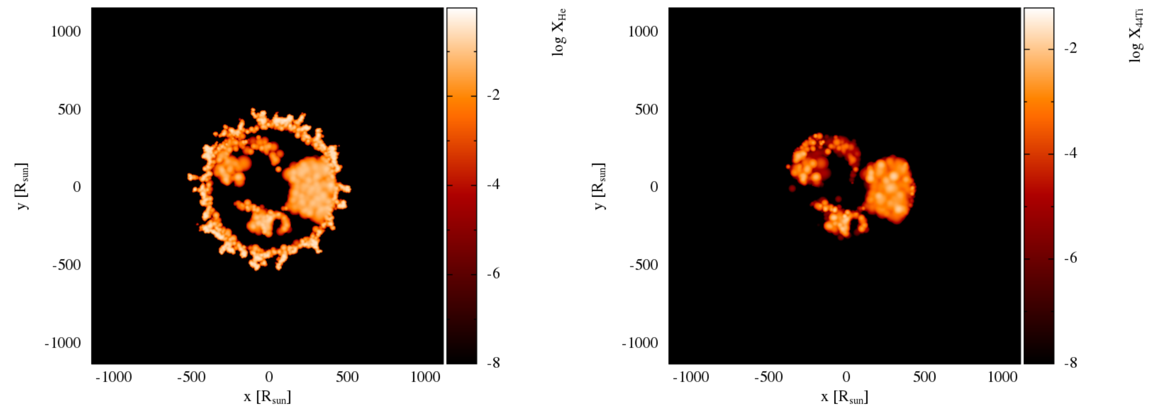

Figure 4.2: *Left:* The spatial ^{4}He abundance in the 15M_dco model at the final time step of the simulation, highlighting the locations where an α-rich freezeout occurred. *Right:* The spatial abundance of ^{44}Ti in the 15M_dco model at the final simulation time step for comparison.

mostly depleted due to the increased fallback of material when compared to the 15M_sym and 15M_bip models. The exceptions are ^{44}Ti and ^{48}Cr, produced in the freezeout. Figure 4.2 (right) shows the spatial distribution of ^{44}Ti for the 15M_dco model in the aftermath of the α-rich freezeout. The freezeout is concentrated in the outward-moving plumes. Unlike the other models, material with high X(^{44}Ti) ($> 10^{-2}$) reaching the base of the Rayleigh-Taylor fingers generated by the reverse shock at the CO shell. The same material is high in ^{56}Ni as well, though the ^{56}Ni/^{44}Ti ratio varies considerably. It is thus possible to anisotropically overturn substantial parcels of Fe-rich material (from decay of ^{56}Ni) to the outside of other burning shells.

4.4.2 20 $M_\odot$ Models

Our set of 20 $M_\odot$ models include one symmetric explosion (20M_sym), one bipolar explosion (20M_bip), and one equatorial explosion (20M_equ). As with the set of 15 $M_\odot$ models, we have included tables of the full yields for all 524 isotopes in the Burnf network (see Tables B.4–B.6). Figure 4.3 (left) shows a graphical summary of the bulk yields of these three simulations for $Z < 35$, and Figure 4.3 (right) shows

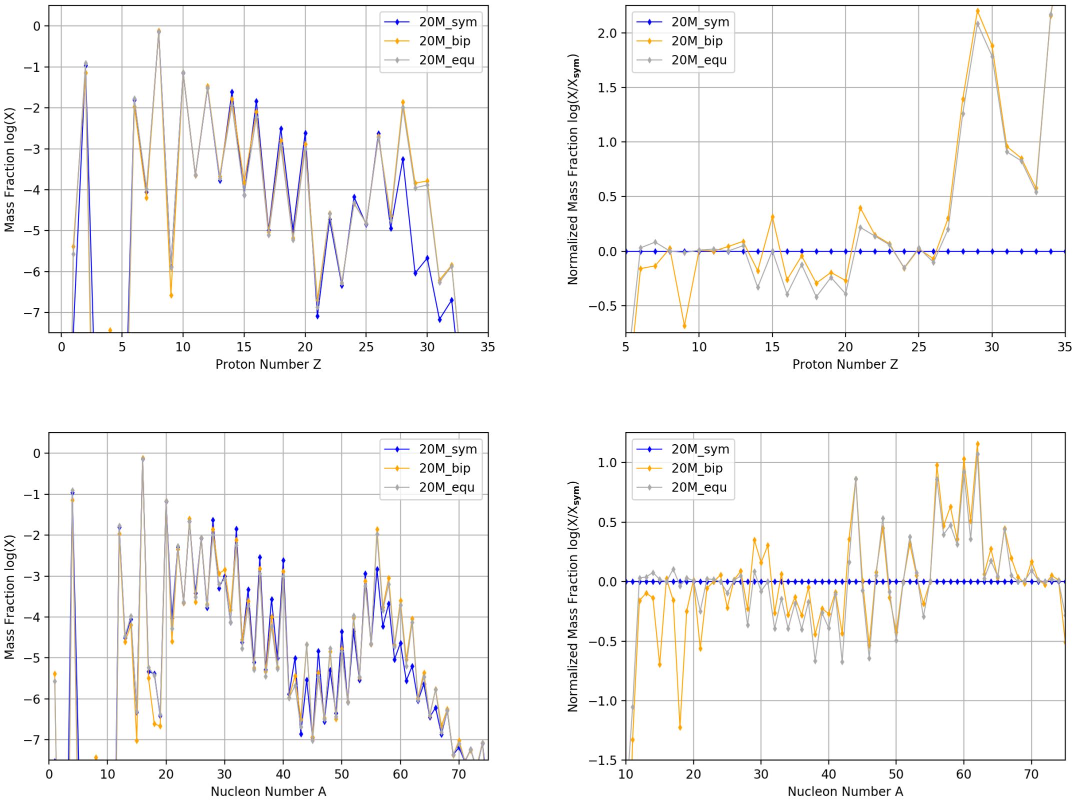

Figure 4.3: Comparative line plots of the yields for all three 20 $M_\odot$ models. Blue indicates the symmetric model 20M_sym, green indicates the bipolar model 20M_bip, and yellow indicates the equatorial model 20M_equ. *Top left:* Mass fractions of total yields produced in the 20 $M_\odot$ models, plotted by element up to proton number $Z = 35$. Note that $Z = 0$ indicates free neutrons. *Top right:* Same data as top left, but normalized to the yields of the symmetric model 20M_sym. *Bottom left:* Mass fractions of total yields for the 20 $M_\odot$ models, plotted by nucleon number up to $A = 75$. *Bottom right:* Same data as bottom left, but normalized to the yields of the symmetric model.

the same data normalized to the symmetric model 20M_sym. Again, the normalized plot is designed to emphasize differences between the models, since these represent the effects of the imposed asymmetries.

The differences in overall yields for the bipolar and equatorial models are small, likely because the imposed bipolar and equatorial asymmetries are of similar nature. Both are 2:1 velocity asymmetries of the supernova ejecta, with the only difference being that one concentrates its highest-velocity SPH particles near two antipodal

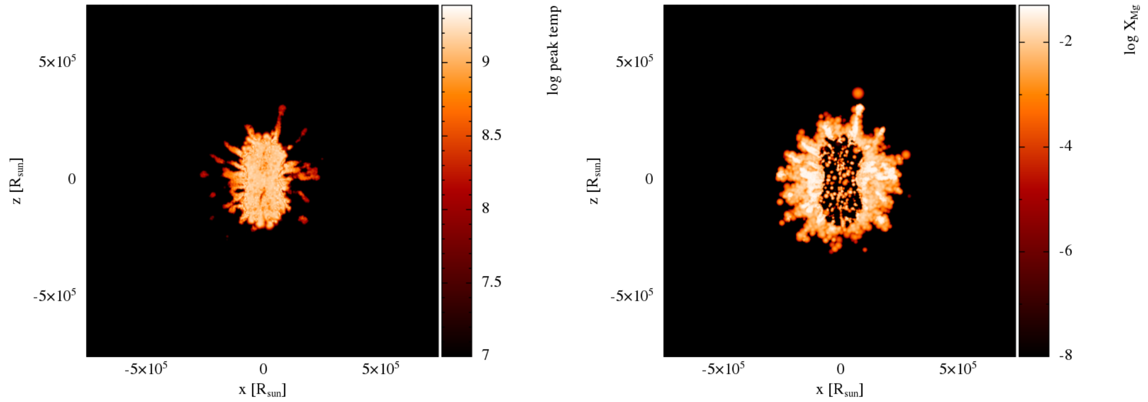

Figure 4.4: *Left:* The peak temperatures encountered by particles in the 20M_bip model. Temperatures are in units of log Kelvin. *Right:* The spatial abundance of Mg in the 20M_bip model at the final simulation time step.

points on the star, while the other concentrates them near a great circle on the star. Among these two models, the bipolar explosion produced less explosive burning overall than the equatorial explosion did. This is due to the fact that the bipolar velocity scheme concentrates kinetic energy among fewer particles than the equatorial scheme does. In the bipolar model, a few very energetic particles get over the energy threshold to trigger explosive burning. The equatorial model spreads that energy out so that more particles are able to cross the energy threshold, but there will be fewer particles at even higher energies. Since the equatorial model allows more particles to reach the threshold, more material in the star is able to undergo explosive burning.

While the two asymmetric models show similar yields, the supernova that stands out in this trio is the symmetric model. The lack of any velocity asymmetry in the symmetric model prevents much of the core material having a chance to escape the star. Fallback is significantly higher than in the other models, the collapsing core of the star is larger, and yields of nickel and heavier elements are greatly reduced. The symmetric model ultimately yields more sulfur and silicon than the other models due to reduced explosive burning. Without any velocity asymmetry, the limited explosion energy is less concentrated at any particular location in the stellar material, and less explosive burning is able to occur. In the case of these 20 $M_\odot$ models, the simple existence of an asymmetry proves to be more influential than the precise nature of the asymmetry.

4.5 Conclusions

We have presented a series of seven supernova simulations carried out in full 3D with the goal of understanding the effects of supernova morphology on nucleosynthetic yields. We imposed a variety of symmetric and asymmetric explosion geometries on progenitor stars of 15 and 20 solar masses. Comparing the overall yields across supernovae with the same progenitor mass showed that asymmetries in the explosion morphology can lead to significant differences. Continuing in this way, we hope to show that 3D supernova simulations can be used to begin probing the natural variations present in actual supernovae and using observed yields to extrapolate to the conditions in the explosion.

The results of our yields confirm the general sentiment that supernova asymmetries are influential for nucleosynthetic considerations. Small changes in the temperature and density conditions of the explosion can favor or disfavor specific nuclear reactions to alter the composition of material. Structures in the velocities of the ejecta change what material escapes and what is accreted onto the compact object, which also affects the composition of the supernova remnant. As seen with the 15 $M_\odot$ progenitors, non-static modeling of the compact object can generate convective asymmetries from fallback that do not occur for models employing simpler static inner boundary conditions. These differences can produce yields differing by orders of magnitude for many isotopes, especially heavier, neutron-rich nuclei from the deep stellar interior that might not otherwise escape the explosion. From the 20 $M_\odot$ progenitors, we learned that simply having an asymmetry present in the explosion can be more important than the exact nature of the asymmetry. When some regions of the explosion have more concentrated kinetic energy than others, those regions can be subject to more explosive burning than would be the case without such asymmetric concentrations.

Even among those models that differed from one another the least, there can still be isotopes that differ strongly in abundance due to more subtle variations in the amount of explosive burning that results from the angular distribution of kinetic energy in the supernova ejecta. Explosive silicon and oxygen burning are common in supernova explosions, so those elements and the explosive burning products can see their abundances change under these conditions. In addition, nucleosynthetic products from deep within the star depend on the velocity distribution of the explosion, so distributions that disperse that material more effectively will yield different ejecta compositions than distributions that do not.

In the 15 $M_\odot$ simulation with an explicitly modeled compact object (15M_dco), the asymmetry in the explosion led to an α-rich freezeout with conditions such that production of ^{44}Ti was disfavored in many regions. Magkotsios *et al.* (2010) explore how the peak temperatures and associated densities that material is subjected to can influence production of ^{44}Ti under just such conditions. We find that particles in our 15M_dco supernova model sample the lower ranges of temperatures and densities considered by Magkotsios *et al.* (2010), and we encounter the same "crevice" where the resulting abundance of ^{44}Ti is substantially lower than would be the case for slightly higher peak temperatures. See Figure 4.5 for a two-dimensional plot of the ^{44}Ti abundance of our SPH particles against the peak explosion conditions. This plot is scaled and colored in the style of Magkotsios *et al.* (2010) for ease of comparison with their results. Predictions of our simulation can also be compared to the abundances of ^{44}Ti observed in the supernova remnant Cas A, which were recently spatially mapped by Grefenstette *et al.* (2017). It may be possible to combine these results with ours to

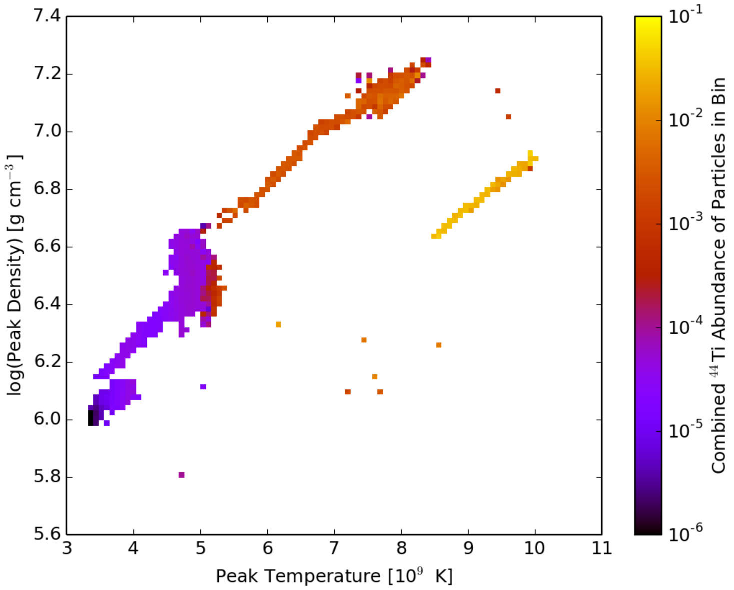

Figure 4.5: A plot of the ^{44}Ti abundance of SPH particles in our 15M_dco simulation (15 $M_\odot$, compact object) against the peak temperatures and densities encountered by the particles over the course of the explosion. It can be seen that for the conditions encountered in this explosion model, many particles had very low abundances of ^{44}Ti. Our results sample the lower ranges of peak temperature and density considered in Magkotsios *et al.* (2010), and the above plot is scaled and colored for straightforward comparison with their results.

gain insights into the conditions present in the Cas A ejecta that led to the production of these isotopes.

In future work, we intend to continue the analysis of these models, which include a wealth of information about expectations for the eventual possibility of predictive yields from supernova simulations. One current endeavor is exploring the potassium production mechanisms in these models. In practice, potassium is difficult to measure spectroscopically, but isotopes of K may be significant for protostellar disks and the formation of planetary systems. There is something to be gained by searching for reliable methods of associating the abundance of potassium with other indicator elements like calcium or magnesium, which can be more easily measured in supernova remnants by observational means.

Chapter 5

CONCLUSIONS

5.1 Summary

In this dissertation, I have presented an exploration of supernovae conducted through the chemical elements and high-energy particles that these events spread into the universe. These products of supernovae can offer a window into several astrophysical models that are used to understand the universe, such as the history of cosmic chemical evolution, the origins of cosmic rays, and the inner workings of the supernova engine itself. Beyond this, the implications of supernova research have fundamental importance to many subfields of astronomy and planetary science, such as radioisotope dating, SiC X grains in meteoritics, and chemistry in astrobiology.

5.2 Titanium and Iron

The central engine of the supernova can be explored via the closely connected yields of iron and ^{44}Ti in supernova remnants. Using a supernova model which allowed for dynamic motion of the compact object, it was demonstrated that mixing above the proto-neutron star, an important element of the supernova engine, is able to stochastically occur in a three-dimensional supernova simulation. The conditions produced in the inner ejecta by this phenomenon affect the production of ^{44}Ti and ^{56}Ni, which can in turn be used to examine the nucleosynthetic conditions. Since high-energy observations of supernova remnants are now able to map the distributions of ^{44}Ti and iron (including decayed ^{56}Ni), these measurements could allow model-aided inference of explosion conditions and progenitor mass.

While this model provides some insights about the central engine, it represents more of a case study than an in-depth analysis dedicated to the subject. For example, the late-time engine interactions that are seen in many multi-dimensional supernova models are absent from this work (e.g., Harris *et al.*, 2017). For more explicit comparison with the recent high-energy observations of Cassiopeia A (Cas A) (Grefenstette *et al.*, 2014, 2017), a supernova simulation progenitor could be more explicitly tailored to align with known constraints on the Cas A progenitor (e.g., Young *et al.*, 2006).

This model demonstrates the future need for additional simulations studying the effects of dynamic compact objects in three-dimensional models. Numerous neutron stars within supernova remnants have been observed to have "kicks"—velocities of hundreds of km/s relative to the center of the expanding remnant. The explicit addition of neutron star kicks into simulations employing dynamic compact objects could result in even more dramatic effects on yields. On the observational side, additional abundance mappings of supernova remnants might help to verify whether the bimodal distribution of Fe/^{44}Ti ratios observed in this work is actually a common feature of remnants.

5.3 Neutrinos

In the examination of IceCube neutrinos, I presented a null result in a statistical analysis of spatial coincidence using the "nearest neighbor" method with Monte Carlo randomization. For track-like IceCube neutrino events at energies over 200 TeV (Aartsen *et al.*, 2016), there was no evidence to suggest a causal relationship with Galactic supernova remnants or open star clusters. A Galactic component of the IceCube neutrino flux (within the limitations used to select the 29 events) was conservatively restricted to no more than 31%, not accounting for other types of potential Galactic neutrino sources. These scenarios do not seem to be the primary way in which the universe produces neutrinos in this energy range, if there is any contribution at all.

The number of qualifications that must be applied to statements of these results demonstrate the limits their applicability. At the very least, the combination of catalogs (the neutrino data set and the four candidate source lists) chosen for my analysis was unfavorable for uncovering evidence of Galactic supernova remnants or open clusters as high-energy neutrino sources. Some of the more exotic models cited in Sections 3.3.2–3.3.3 that would permit these classes of objects to produce PeV cosmic rays are disfavored by these results. If the predictions of these models are accurate, then it seems the confluence of conditions they require is ultimately too rare to be widespread in the Milky Way. Unfortunately, the method of analysis also did not permit a rigorous estimate of the Galactic component of the IceCube flux, nut instead allowed only a very conservative upper limit for two classes of Galactic sources.

Future work on this question would require a number of different approaches. More recently published data from the IceCube collaboration might provide a clearer picture through stronger statistics. Some of the objects singled out in this analysis could warrant future study even if they were not found to be significant here, since the possibility of true causal associations can never be fully ruled out. A more carefully chosen selection of candidate objects might be more capable of finding a small subset of neutrino events that are likely to be associated with Galactic sources. Finally, there are numerous other statistical techniques that might be applied to this problem to greater effect, such as analyses making use of the correlation function.

5.4 Asymmetric Explosions

The analysis of supernova simulation asymmetries presented in this work revealed the significance of three-dimensional explosion asymmetries to the study of supernova nucleosynthesis. By examining the effects of both spherically symmetrical and asymmetrical explosion morphologies on two progenitor stars of differing masses, it was shown that nucleosynthetic yields will vary considerably as a result of morphology. Moreover, it was apparent that simply incorporating a three-dimensional asymmetry into the simulation could be more significant to the yields than the exact nature of the asymmetry. The redistribution of energy relative to a symmetric model may have the effect of producing energy-rich and energy-poor regions of the star that follow distinct thermodynamic trajectories.

One limitation of the approach used is that the artificial imposition of explosion morphology on the models is somewhat unrealistic. More realistic asymmetries, like those which arose in model 15M_dco (which also formed the basis of Chapter 2) are to be preferred, especially since their effect on yields may be even greater. In real stars, a number of internal and external factors can drive the formation of asymmetries in a core-collapse supernova (e.g., rotation rate, stellar convection, circumstellar medium). Simulations that allow asymmetries to arise as physical consequences of the initial conditions represent a more "natural" approach to modeling supernova nucleosynthesis as it actually occurs.

The preliminary discoveries of this work suggest that supernova nucleosynthesis models published in the future should strive to incorporate three-dimensional asymmetries, or at least address how spherical symmetry might influence the results. At this point, a larger spread of simulation models is needed in order to further quantify the precise effects of various types of asymmetries on progenitor stars of different masses. It is also important to increase the number of models incorporating realistic asymmetries, such as a circumstellar medium based on stellar wind models of mass loss or a stellar interior seeded with convective asymmetries from the late burning stages of a stellar evolution model.

REFERENCES

Aartsen, M. G., R. Abbasi, M. Ackermann, J. Adams, J. A. Aguilar, M. Ahlers, D. Altmann, C. Arguelles, J. Auffenberg, X. Bai, M. Baker, S. W. Barwick, V. Baum, R. Bay, J. J. Beatty, J. Becker Tjus, K. H. Becker, S. BenZvi, P. Berghaus, D. Berley, E. Bernardini, A. Bernhard, D. Z. Besson, G. Binder, D. Bindig, M. Bissok, E. Blaufuss, J. Blumenthal, D. J. Boersma, C. Bohm, D. Bose, S. Böser, O. Botner, L. Brayeur, H. P. Bretz, A. M. Brown, R. Bruijn, J. Casey, M. Casier, D. Chirkin, A. Christov, B. Christy, K. Clark, L. Classen, F. Clevermann, S. Coenders, S. Cohen, D. F. Cowen, A. H. Cruz Silva, M. Danninger, J. Daughhetee, J. C. Davis, M. Day, C. De Clercq, S. De Ridder, P. Desiati, K. D. de Vries, M. de With, T. DeYoung, J. C. Díaz-Vélez, M. Dunkman, R. Eagan, B. Eberhardt, B. Eichmann, J. Eisch, S. Euler, P. A. Evenson, O. Fadiran, A. R. Fazely, A. Fedynitch, J. Feintzeig, T. Feusels, K. Filimonov, C. Finley, T. Fischer-Wasels, S. Flis, A. Franckowiak, K. Frantzen, T. Fuchs, T. K. Gaisser, J. Gallagher, L. Gerhardt, L. Gladstone, T. Glüsenkamp, A. Goldschmidt, G. Golup, J. G. Gonzalez, J. A. Goodman, D. Góra, D. T. Grandmont, D. Grant, P. Gretskov, J. C. Groh, A. Groß, C. Ha, A. Haj Ismail, P. Hallen, A. Hallgren, F. Halzen, K. Hanson, D. Hebecker, D. Heereman, D. Heinen, K. Helbing, R. Hellauer, S. Hickford, G. C. Hill, K. D. Hoffman, R. Hoffmann, A. Homeier, K. Hoshina, F. Huang, W. Huelsnitz, P. O. Hulth, K. Hultqvist, S. Hussain, A. Ishihara, S. Jackson, E. Jacobi, J. Jacobsen, K. Jagielski, G. S. Japaridze, K. Jero, O. Jlelati, B. Kaminsky, A. Kappes, T. Karg, A. Karle, M. Kauer, J. L. Kelley, J. Kiryluk, J. Kläs, S. R. Klein, J. H. Köhne, G. Kohnen, H. Kolanoski, L. Köpke, C. Kopper, S. Kopper, D. J. Koskinen, M. Kowalski, M. Krasberg, A. Kriesten, K. Krings, G. Kroll, J. Kunnen, N. Kurahashi, T. Kuwabara, M. Labare, H. Landsman, M. J. Larson, M. Lesiak-Bzdak, M. Leuermann, J. Leute, J. Lünemann, O. Macías, J. Madsen, G. Maggi, R. Maruyama, K. Mase, H. S. Matis, F. McNally, K. Meagher, M. Merck, T. Meures, S. Miarecki, E. Middell, N. Milke, J. Miller, L. Mohrmann, T. Montaruli, R. Morse, R. Nahnhauer, U. Naumann, H. Niederhausen, S. C. Nowicki, D. R. Nygren, A. Obertacke, S. Odrowski, A. Olivas, A. Omairat, A. O'Murchadha, L. Paul, J. A. Pepper, C. Pérez de los Heros, C. Pfendner, D. Pieloth, E. Pinat, J. Posselt, P. B. Price, G. T. Przybylski, M. Quinnan, L. Rädel, M. Rameez, K. Rawlins, P. Redl, R. Reimann, E. Resconi, W. Rhode, M. Ribordy, M. Richman, B. Riedel, S. Robertson, J. P. Rodrigues, C. Rott, T. Ruhe, B. Ruzybayev, D. Ryckbosch, S. M. Saba, H. G. Sander, M. Santander, S. Sarkar, K. Schatto, F. Scheriau, T. Schmidt, M. Schmitz, S. Schoenen, S. Schöneberg, A. Schönwald, A. Schukraft, L. Schulte, O. Schulz, D. Seckel, Y. Sestayo, S. Seunarine, R. Shanidze, C. Sheremata, M. W. E. Smith, D. Soldin, G. M. Spiczak, C. Spiering, M. Stamatikos, T. Stanev, N. A. Stanisha, A. Stasik, T. Stezelberger, R. G. Stokstad, A. Stößl, E. A. Strahler, R. Ström, N. L. Strotjohann, G. W. Sullivan, H. Taavola, I. Taboada, A. Tamburro, A. Tepe, S. Ter-Antonyan, G. Te{š}ić, S. Tilav, P. A. Toale, M. N. Tobin, S. Toscano, M. Tselengidou, E. Unger, M. Usner, S. Vallecorsa, N. van Eijndhoven, A. Van Overloop, J. van Santen, M. Vehring, M. Voge, M. Vraeghe, C. Walck, T. Waldenmaier, M. Wallraff, C. Weaver, M. Wellons, C. Wendt, S. Westerhoff, B. Whelan, N. Whitehorn, K. Wiebe, C. H. Wiebusch, D. R. Williams, H. Wissing, M. Wolf, T. R. Wood, K. Woschnagg, D. L. Xu, X. W. Xu, J. P.

Yanez, G. Yodh, S. Yoshida, P. Zarzhitsky, J. Ziemann, S. Zierke and M. Zoll, "Energy reconstruction methods in the IceCube neutrino telescope", Journal of Instrumentation **9**, 3, P03009 (2014a).

Aartsen, M. G., K. Abraham, M. Ackermann, J. Adams, J. A. Aguilar, M. Ahlers, M. Ahrens, D. Altmann, K. Andeen, T. Anderson and et al., "Observation and Characterization of a Cosmic Muon Neutrino Flux from the Northern Hemisphere Using Six Years of IceCube Data", Astrophys. J. **833**, 3 (2016).

Aartsen, M. G., K. Abraham, M. Ackermann, J. Adams, J. A. Aguilar, M. Ahlers, M. Ahrens, D. Altmann, K. Andeen, T. Anderson and et al., "All-sky Search for Time-integrated Neutrino Emission from Astrophysical Sources with 7 yr of IceCube Data", Astrophys. J. **835**, 2, 151 (2017a).

Aartsen, M. G., K. Abraham, M. Ackermann, J. Adams, J. A. Aguilar, M. Ahlers, M. Ahrens, D. Altmann, K. Andeen, T. Anderson and et al., "The Contribution of Fermi-2LAC Blazars to Diffuse TeV-PeV Neutrino Flux", Astrophys. J. **835**, 1, 45 (2017b).

Aartsen, M. G., M. Ackermann, J. Adams, J. A. Aguilar, M. Ahlers, M. Ahrens, C. Alispach, D. Altmann, K. Andeen, T. Anderson, I. Ansseau, G. Anton, C. Argüelles, J. Auffenberg, S. Axani, P. Backes, H. Bagherpour, X. Bai, A. Barbano, S. W. Barwick, V. Baum, R. Bay, J. J. Beatty, K. H. Becker, J. Becker Tjus, S. BenZvi, D. Berley, E. Bernardini, D. Z. Besson, G. Binder, D. Bindig, E. Blaufuss, S. Blot, C. Bohm, M. Börner, S. Böser, O. Botner, E. Bourbeau, J. Bourbeau, F. Bradascio, J. Braun, H. P. Bretz, S. Bron, J. Brostean-Kaiser, A. Burgman, R. S. Busse, T. Carver, C. Chen, E. Cheung, D. Chirkin, K. Clark, L. Classen, G. H. Collin, J. M. Conrad, P. Coppin, P. Correa, D. F. Cowen, R. Cross, P. Dave, J. P. A. M. de André, C. De Clercq, J. J. DeLaunay, H. Dembinski, K. Deoskar, S. De Ridder, P. Desiati, K. D. de Vries, G. de Wasseige, M. de With, T. DeYoung, J. C. Díaz-Vélez, H. Dujmovic, M. Dunkman, E. Dvorak, B. Eberhardt, T. Ehrhardt, P. Eller, P. A. Evenson, S. Fahey, A. R. Fazely, J. Felde, K. Filimonov, C. Finley, A. Franckowiak, E. Friedman, A. Fritz, T. K. Gaisser, J. Gallagher, E. Ganster, S. Garrappa, L. Gerhardt, K. Ghorbani, T. Glauch, T. Glüsenkamp, A. Goldschmidt, J. G. Gonzalez, D. Grant, Z. Griffith, M. Günder, M. Gündüz, C. Haack, A. Hallgren, L. Halve, F. Halzen, K. Hanson, D. Hebecker, D. Heereman, K. Helbing, R. Hellauer, F. Henningsen, S. Hickford, J. Hignight, G. C. Hill, K. D. Hoffman, R. Hoffmann, T. Hoinka, B. Hokanson-Fasig, K. Hoshina, F. Huang, M. Huber, K. Hultqvist, M. Hünnefeld, R. Hussain, S. In, N. Iovine, A. Ishihara, E. Jacobi, G. S. Japaridze, M. Jeong, K. Jero, B. J. P. Jones, W. Kang, A. Kappes, D. Kappesser, T. Karg, M. Karl, A. Karle, U. Katz, M. Kauer, A. Keivani, J. L. Kelley, A. Kheirandish, J. Kim, T. Kintscher, J. Kiryluk, T. Kittler, S. R. Klein, R. Koirala, H. Kolanoski, L. Köpke, C. Kopper, S. Kopper, D. J. Koskinen, M. Kowalski, K. Krings, G. Krückl, N. Kulacz, S. Kunwar, N. Kurahashi, A. Kyriacou, M. Labare, J. L. Lanfranchi, M. J. Larson, F. Lauber, J. P. Lazar, K. Leonard, M. Leuermann, Q. R. Liu, E. Lohfink, C. J. Lozano Mariscal, L. Lu, F. Lucarelli, J. Lünemann, W. Luszczak, J. Madsen, G. Maggi, K. B. M. Mahn, Y. Makino, K. Mallot, S. Mancina, I. C. Mariș, R. Maruyama, K. Mase, R. Maunu,

K. Meagher, M. Medici, A. Medina, M. Meier, S. Meighen-Berger, T. Menne, G. Merino, T. Meures, S. Miarecki, J. Micallef, G. Momenté, T. Montaruli, R. W. Moore, M. Moulai, R. Nagai, R. Nahnhauer, P. Nakarmi, U. Naumann, G. Neer, H. Niederhausen, S. C. Nowicki, D. R. Nygren, A. Obertacke Pollmann, A. Olivas, A. O'Murchadha, E. O'Sullivan, T. Palczewski, H. Pandya, D. V. Pankova, N. Park, P. Peiffer, C. Pérez de los Heros, D. Pieloth, E. Pinat, A. Pizzuto, M. Plum, P. B. Price, G. T. Przybylski, C. Raab, A. Raissi, M. Rameez, L. Rauch, K. Rawlins, I. C. Rea, R. Reimann, B. Relethford, G. Renzi, E. Resconi, W. Rhode, M. Richman, S. Robertson, M. Rongen, C. Rott, T. Ruhe, D. Ryckbosch, D. Rysewyk, I. Safa, S. E. Sanchez Herrera, A. Sandrock, J. Sandroos, M. Santander, S. Sarkar, S. Sarkar, K. Satalecka, M. Schaufel, P. Schlunder, T. Schmidt, A. Schneider, J. Schneider, L. Schumacher, S. Sclafani, D. Seckel, S. Seunarine, M. Silva, R. Snihur, J. Soedingrekso, D. Soldin, M. Song, G. M. Spiczak, C. Spiering, J. Stachurska, M. Stamatikos, T. Stanev, A. Stasik, R. Stein, J. Stettner, A. Steuer, T. Stezelberger, R. G. Stokstad, A. Stößl, N. L. Strotjohann, R. Ström, T. Stuttard, G. W. Sullivan, M. Sutherland, I. Taboada, F. Tenholt, S. Ter-Antonyan, A. Terliuk, S. Tilav, L. Tomankova, C. Tönnis, S. Toscano, D. Tosi, M. Tselengidou, C. F. Tung, A. Turcati, R. Turcotte, C. F. Turley, B. Ty, E. Unger, M. A. Unland Elorrieta, M. Usner, J. Vandenbroucke, W. Van Driessche, D. van Eijk, N. van Eijndhoven, S. Vanheule, J. van Santen, M. Vraeghe, C. Walck, A. Wallace, M. Wallraff, N. Wandkowsky, T. B. Watson, C. Weaver, M. J. Weiss, J. Weldert, C. Wendt, J. Werthebach, S. Westerhoff, B. J. Whelan, N. Whitehorn, K. Wiebe, C. H. Wiebusch, L. Wille, D. R. Williams, L. Wills, M. Wolf, J. Wood, T. R. Wood, K. Woschnagg, G. Wrede, D. L. Xu, X. W. Xu, Y. Xu, J. P. Yanez, G. Yodh, S. Yoshida and T. Yuan, "Neutrinos below 100 TeV from the southern sky employing refined veto techniques to IceCube data", Astroparticle Physics **116**, 102392 (2020a).

Aartsen, M. G., M. Ackermann, J. Adams, J. A. Aguilar, M. Ahlers, M. Ahrens, C. Alispach, K. Andeen, T. Anderson, I. Ansseau, G. Anton, C. Argüelles, J. Auffenberg, S. Axani, P. Backes, H. Bagherpour, X. Bai, A. Balagopal, A. Barbano, S. W. Barwick, B. Bastian, V. Baum, S. Baur, R. Bay, J. J. Beatty, K. H. Becker, J. Becker Tjus, S. BenZvi, D. Berley, E. Bernardini, D. Z. Besson, G. Binder, D. Bindig, E. Blaufuss, S. Blot, C. Bohm, M. Börner, S. Böser, O. Botner, J. Böttcher, E. Bourbeau, J. Bourbeau, F. Bradascio, J. Braun, S. Bron, J. Brostean-Kaiser, A. Burgman, J. Buscher, R. S. Busse, T. Carver, C. Chen, E. Cheung, D. Chirkin, S. Choi, K. Clark, L. Classen, A. Coleman, G. H. Collin, J. M. Conrad, P. Coppin, P. Correa, D. F. Cowen, R. Cross, P. Dave, C. De Clercq, J. J. DeLaunay, H. Dembinski, K. Deoskar, S. De Ridder, P. Desiati, K. D. de Vries, G. de Wasseige, M. de With, T. DeYoung, A. Diaz, J. C. Díaz-Vélez, H. Dujmovic, M. Dunkman, E. Dvorak, B. Eberhardt, T. Ehrhardt, P. Eller, R. Engel, P. A. Evenson, S. Fahey, A. R. Fazely, J. Felde, K. Filimonov, C. Finley, D. Fox, A. Franckowiak, E. Friedman, A. Fritz, T. K. Gaisser, J. Gallagher, E. Ganster, S. Garrappa, L. Gerhardt, K. Ghorbani, T. Glauch, T. Glüsenkamp, A. Goldschmidt, J. G. Gonzalez, D. Grant, Z. Griffith, S. Griswold, M. Günder, M. Gündüz, C. Haack, A. Hallgren, R. Halliday, L. Halve, F. Halzen, K. Hanson, A. Haungs, D. Hebecker, D. Heereman, P. Heix, K. Helbing, R. Hellauer, F. Henningsen, S. Hickford, J. Hignight, G. C. Hill, K. D. Hoffman, R. Hoffmann, T. Hoinka, B. Hokanson-Fasig, K. Hoshina, F. Huang,

M. Huber, T. Huber, K. Hultqvist, M. Hünnefeld, R. Hussain, S. In, N. Iovine, A. Ishihara, G. S. Japaridze, M. Jeong, K. Jero, B. J. P. Jones, F. Jonske, R. Joppe, D. Kang, W. Kang, A. Kappes, D. Kappesser, T. Karg, M. Karl, A. Karle, U. Katz, M. Kauer, J. L. Kelley, A. Kheirandish, J. Kim, T. Kintscher, J. Kiryluk, T. Kittler, S. R. Klein, R. Koirala, H. Kolanoski, L. Köpke, C. Kopper, S. Kopper, D. J. Koskinen, M. Kowalski, K. Krings, G. Krückl, N. Kulacz, N. Kurahashi, A. Kyriacou, M. Labare, J. L. Lanfranchi, M. J. Larson, F. Lauber, J. P. Lazar, K. Leonard, A. Leszczyńska, M. Leuermann, Q. R. Liu, E. Lohfink, C. J. Lozano Mariscal, L. Lu, F. Lucarelli, J. Lünemann, W. Luszczak, Y. Lyu, W. Y. Ma, J. Madsen, G. Maggi, K. B. M. Mahn, Y. Makino, P. Mallik, K. Mallot, S. Mancina, I. C. Mariș, R. Maruyama, K. Mase, H. S. Matis, R. Maunu, F. McNally, K. Meagher, M. Medici, A. Medina, M. Meier, S. Meighen-Berger, T. Menne, G. Merino, T. Meures, J. Micallef, D. Mockler, G. Momenté, T. Montaruli, R. W. Moore, R. Morse, M. Moulai, P. Muth, R. Nagai, U. Naumann, G. Neer, H. Niederhausen, M. U. Nisa, S. C. Nowicki, D. R. Nygren, A. Obertacke Pollmann, M. Oehler, A. Olivas, A. O'Murchadha, E. O'Sullivan, T. Palczewski, H. Pandya, D. V. Pankova, N. Park, P. Peiffer, C. Pérez de los Heros, S. Philippen, D. Pieloth, E. Pinat, A. Pizzuto, M. Plum, A. Porcelli, P. B. Price, G. T. Przybylski, C. Raab, A. Raissi, M. Rameez, L. Rauch, K. Rawlins, I. C. Rea, R. Reimann, B. Relethford, M. Renschler, G. Renzi, E. Resconi, W. Rhode, M. Richman, S. Robertson, M. Rongen, C. Rott, T. Ruhe, D. Ryckbosch, D. Rysewyk, I. Safa, S. E. Sanchez Herrera, A. Sandrock, J. Sandroos, M. Santander, S. Sarkar, S. Sarkar, K. Satalecka, M. Schaufel, H. Schieler, P. Schlunder, T. Schmidt, A. Schneider, J. Schneider, F. G. Schröder, L. Schumacher, S. Sclafani, D. Seckel, S. Seunarine, S. Shefali, M. Silva, R. Snihur, J. Soedingrekso, D. Soldin, M. Song, G. M. Spiczak, C. Spiering, J. Stachurska, M. Stamatikos, T. Stanev, R. Stein, P. Steinmüller, J. Stettner, A. Steuer, T. Stezelberger, R. G. Stokstad, A. Stößl, N. L. Strotjohann, T. Stürwald, T. Stuttard, G. W. Sullivan, I. Taboada, F. Tenholt, S. Ter-Antonyan, A. Terliuk, S. Tilav, K. Tollefson, L. Tomankova, C. Tönnis, S. Toscano, D. Tosi, A. Trettin, M. Tselengidou, C. F. Tung, A. Turcati, R. Turcotte, C. F. Turley, B. Ty, E. Unger, M. A. Unland Elorrieta, M. Usner, J. Vandenbroucke, W. Van Driessche, D. van Eijk, N. van Eijndhoven, S. Vanheule, J. van Santen, M. Vraeghe, C. Walck, A. Wallace, M. Wallraff, N. Wandkowsky, T. B. Watson, C. Weaver, A. Weindl, M. J. Weiss, J. Weldert, C. Wendt, J. Werthebach, B. J. Whelan, N. Whitehorn, K. Wiebe, C. H. Wiebusch, L. Wille, D. R. Williams, L. Wills, M. Wolf, J. Wood, T. R. Wood, K. Woschnagg, G. Wrede, D. L. Xu, X. W. Xu, Y. Xu, J. P. Yanez, G. Yodh, S. Yoshida, T. Yuan and M. Zöcklein, "Time-Integrated Neutrino Source Searches with 10 Years of IceCube Data", Phys. Rev. Lett. **124**, 5, 051103 (2020b).

Aartsen, M. G., M. Ackermann, J. Adams, J. A. Aguilar, M. Ahlers, M. Ahrens, D. Altmann, K. Andeen, T. Anderson, I. Ansseau, G. Anton, M. Archinger, C. Argüelles, R. Auer, J. Auffenberg, S. Axani, J. Baccus, X. Bai, S. Barnet, S. W. Barwick, V. Baum, R. Bay, K. Beattie, J. J. Beatty, J. Becker Tjus, K. H. Becker, T. Bendfelt, S. BenZvi, D. Berley, E. Bernardini, A. Bernhard, D. Z. Besson, G. Binder, D. Bindig, M. Bissok, E. Blaufuss, S. Blot, D. Boersma, C. Bohm, M. Börner, F. Bos, D. Bose, S. Böser, O. Botner, A. Bouchta, J. Braun, L. Brayeur, H. P. Bretz, S. Bron, A. Burgman, C. Burreson, T. Carver, M. Casier, E. Cheung,

D. Chirkin, A. Christov, K. Clark, L. Classen, S. Coenders, G. H. Collin, J. M. Conrad, D. F. Cowen, R. Cross, C. Day, M. Day, J. P. A. M. de André, C. De Clercq, E. del Pino Rosendo, H. Dembinski, S. De Ridder, F. Descamps, P. Desiati, K. D. de Vries, G. de Wasseige, M. de With, T. DeYoung, J. C. Díaz-Vélez, V. di Lorenzo, H. Dujmovic, J. P. Dumm, M. Dunkman, B. Eberhardt, W. R. Edwards, T. Ehrhardt, B. Eichmann, P. Eller, S. Euler, P. A. Evenson, S. Fahey, A. R. Fazely, J. Feintzeig, J. Felde, K. Filimonov, C. Finley, S. Flis, C. C. Fösig, A. Franckowiak, M. Frère, E. Friedman, T. Fuchs, T. K. Gaisser, J. Gallagher, L. Gerhardt, K. Ghorbani, W. Giang, L. Gladstone, T. Glauch, D. Glowacki, T. Glüsenkamp, A. Goldschmidt, J. G. Gonzalez, D. Grant, Z. Griffith, L. Gustafsson, C. Haack, A. Hallgren, F. Halzen, E. Hansen, T. Hansmann, K. Hanson, J. Haugen, D. Hebecker, D. Heereman, K. Helbing, R. Hellauer, R. Heller, S. Hickford, J. Hignight, G. C. Hill, K. D. Hoffman, R. Hoffmann, K. Hoshina, F. Huang, M. Huber, P. O. Hulth, K. Hultqvist, S. In, M. Inaba, A. Ishihara, E. Jacobi, J. Jacobsen, G. S. Japaridze, M. Jeong, K. Jero, A. Jones, B. J. P. Jones, J. Joseph, W. Kang, A. Kappes, T. Karg, A. Karle, U. Katz, M. Kauer, A. Keivani, J. L. Kelley, J. Kemp, A. Kheirandish, J. Kim, M. Kim, T. Kintscher, J. Kiryluk, N. Kitamura, T. Kittler, S. R. Klein, S. Kleinfelder, M. Kleist, G. Kohnen, R. Koirala, H. Kolanoski, R. Konietz, L. Köpke, C. Kopper, S. Kopper, D. J. Koskinen, M. Kowalski, M. Krasberg, K. Krings, M. Kroll, G. Krückl, C. Krüger, J. Kunnen, S. Kunwar, N. Kurahashi, T. Kuwabara, M. Labare, K. Laihem, H. Landsman, J. L. Lanfranchi, M. J. Larson, F. Lauber, A. Laundrie, D. Lennarz, H. Leich, M. Lesiak-Bzdak, M. Leuermann, L. Lu, J. Ludwig, J. Lünemann, C. Mackenzie, J. Madsen, G. Maggi, K. B. M. Mahn, S. Mancina, M. Mand elartz, R. Maruyama, K. Mase, H. Matis, R. Maunu, F. McNally, C. P. McParland, P. Meade, K. Meagher, M. Medici, M. Meier, A. Meli, T. Menne, G. Merino, T. Meures, S. Miarecki, R. H. Minor, T. Montaruli, M. Moulai, T. Murray, R. Nahnhauer, U. Naumann, G. Neer, M. Newcomb, H. Niederhausen, S. C. Nowicki, D. R. Nygren, A. Obertacke Pollmann, A. Olivas, A. O'Murchadha, T. Palczewski, H. Pandya, D. V. Pankova, S. Patton, P. Peiffer, Ö. Penek, J. A. Pepper, C. Pérez de los Heros, C. Pettersen, D. Pieloth, E. Pinat, P. B. Price, G. T. Przybylski, M. Quinnan, C. Raab, L. Rädel, M. Rameez, K. Rawlins, R. Reimann, B. Relethford, M. Relich, E. Resconi, W. Rhode, M. Richman, B. Riedel, S. Robertson, M. Rongen, C. Roucelle, C. Rott, T. Ruhe, D. Ryckbosch, D. Rysewyk, L. Sabbatini, S. E. Sanchez Herrera, A. Sandrock, J. Sandroos, P. Sand strom, S. Sarkar, K. Satalecka, P. Schlunder, T. Schmidt, S. Schoenen, S. Schöneberg, A. Schukraft, L. Schumacher, D. Seckel, S. Seunarine, M. Solarz, D. Soldin, M. Song, G. M. Spiczak, C. Spiering, T. Stanev, A. Stasik, J. Stettner, A. Steuer, T. Stezelberger, R. G. Stokstad, A. Stößl, R. Ström, N. L. Strotjohann, K. H. Sulanke, G. W. Sullivan, M. Sutherland, H. Taavola, I. Taboada, J. Tatar, F. Tenholt, S. Ter-Antonyan, A. Terliuk, G. Tešić, L. Thollander, S. Tilav, P. A. Toale, M. N. Tobin, S. Toscano, D. Tosi, M. Tselengidou, A. Turcati, E. Unger, M. Usner, J. Vandenbroucke, N. van Eijndhoven, S. Vanheule, M. van Rossem, J. van Santen, M. Vehring, M. Voge, E. Vogel, M. Vraeghe, D. Wahl, C. Walck, A. Wallace, M. Wallraff, N. Wandkowsky, C. Weaver, M. J. Weiss, C. Wendt, S. Westerhoff, D. Wharton, B. J. Whelan, S. Wickmann, K. Wiebe, C. H. Wiebusch, L. Wille, D. R. Williams, L. Wills, P. Wisniewski, M. Wolf, T. R. Wood, E. Woolsey, K. Woschnagg, D. L. Xu, X. W.

Xu, Y. Xu, J. P. Yanez, G. Yodh, S. Yoshida and M. Zoll, “The IceCube Neutrino Observatory: instrumentation and online systems”, Journal of Instrumentation **12**, 3, P03012 (2017c).

Aartsen, M. G., M. Ackermann, J. Adams, J. A. Aguilar, M. Ahlers, M. Ahrens, D. Altmann, K. Andeen, T. Anderson, I. Ansseau, G. Anton, C. Argüelles, J. Auffenberg, S. Axani, P. Backes, H. Bagherpour, X. Bai, A. Barbano, J. P. Barron, S. W. Barwick, V. Baum, R. Bay, J. J. Beatty, J. Becker Tjus, K. H. Becker, S. BenZvi, D. Berley, E. Bernardini, D. Z. Besson, G. Binder, D. Bindig, E. Blaufuss, S. Blot, C. Bohm, M. Börner, F. Bos, S. Böser, O. Botner, E. Bourbeau, J. Bourbeau, F. Bradascio, J. Braun, H. P. Bretz, S. Bron, J. Brostean-Kaiser, A. Burgman, R. S. Busse, T. Carver, C. Chen, E. Cheung, D. Chirkin, K. Clark, L. Classen, G. H. Collin, J. M. Conrad, P. Coppin, P. Correa, D. F. Cowen, R. Cross, P. Dave, M. Day, J. P. A. M. de André, C. De Clercq, J. J. DeLaunay, H. Dembinski, K. Deoskar, S. De Ridder, P. Desiati, K. D. de Vries, G. de Wasseige, M. de With, T. DeYoung, J. C. Díaz-Vélez, H. Dujmovic, M. Dunkman, E. Dvorak, B. Eberhardt, T. Ehrhardt, B. Eichmann, P. Eller, P. A. Evenson, S. Fahey, A. R. Fazely, J. Felde, K. Filimonov, C. Finley, A. Franckowiak, E. Friedman, A. Fritz, T. K. Gaisser, J. Gallagher, E. Ganster, S. Garrappa, L. Gerhardt, K. Ghorbani, W. Giang, T. Glauch, T. Glüsenkamp, A. Goldschmidt, J. G. Gonzalez, D. Grant, Z. Griffith, C. Haack, A. Hallgren, L. Halve, F. Halzen, K. Hanson, D. Hebecker, D. Heereman, K. Helbing, R. Hellauer, S. Hickford, J. Hignight, G. C. Hill, K. D. Hoffman, R. Hoffmann, T. Hoinka, B. Hokanson-Fasig, K. Hoshina, F. Huang, M. Huber, K. Hultqvist, M. Hünnefeld, R. Hussain, S. In, N. Iovine, A. Ishihara, E. Jacobi, G. S. Japaridze, M. Jeong, K. Jero, B. J. P. Jones, P. Kalaczynski, W. Kang, A. Kappes, D. Kappesser, T. Karg, A. Karle, U. Katz, M. Kauer, A. Keivani, J. L. Kelley, A. Kheirandish, J. Kim, T. Kintscher, J. Kiryluk, T. Kittler, S. R. Klein, R. Koirala, H. Kolanoski, L. Köpke, C. Kopper, S. Kopper, D. J. Koskinen, M. Kowalski, K. Krings, M. Kroll, G. Krückl, S. Kunwar, N. Kurahashi, A. Kyriacou, M. Labare, J. L. Lanfranchi, M. J. Larson, F. Lauber, K. Leonard, M. Leuermann, Q. R. Liu, E. Lohfink, C. J. L. Mariscal, L. Lu, J. Lünemann, W. Luszczak, J. Madsen, G. Maggi, K. B. M. Mahn, Y. Makino, S. Mancina, I. C. Mariş, R. Maruyama, K. Mase, R. Maunu, K. Meagher, M. Medici, M. Meier, T. Menne, G. Merino, T. Meures, S. Miarecki, J. Micallef, G. Momenté, T. Montaruli, R. W. Moore, M. Moulai, R. Nagai, R. Nahnhauer, P. Nakarmi, U. Naumann, G. Neer, H. Niederhausen, S. C. Nowicki, D. R. Nygren, A. Obertacke Pollmann, A. Olivas, A. O’Murchadha, E. O’Sullivan, T. Palczewski, H. Pandya, D. V. Pankova, P. Peiffer, C. Pérez de los Heros, D. Pieloth, E. Pinat, A. Pizzuto, M. Plum, P. B. Price, G. T. Przybylski, C. Raab, M. Rameez, L. Rauch, K. Rawlins, I. C. Rea, R. Reimann, B. Relethford, G. Renzi, E. Resconi, W. Rhode, M. Richman, S. Robertson, M. Rongen, C. Rott, T. Ruhe, D. Ryckbosch, D. Rysewyk, I. Safa, S. E. Sanchez Herrera, A. Sandrock, J. Sandroos, M. Santander, S. Sarkar, S. Sarkar, K. Satalecka, M. Schaufel, P. Schlunder, T. Schmidt, A. Schneider, J. Schneider, S. Schöneberg, L. Schumacher, S. Sclafani, D. Seckel, S. Seunarine, J. Soedingrekso, D. Soldin, M. Song, G. M. Spiczak, C. Spiering, J. Stachurska, M. Stamatikos, T. Stanev, A. Stasik, R. Stein, J. Stettner, A. Steuer, T. Stezelberger, R. G. Stokstad, A. Stößl, N. L. Strotjohann, T. Stuttard, G. W. Sullivan, M. Sutherland, I. Taboada, F. Tenholt, S. Ter-Antonyan, A. Terliuk, S. Tilav,

M. N. Tobin, C. Tönnis, S. Toscano, D. Tosi, M. Tselengidou, C. F. Tung, A. Turcati, R. Turcotte, C. F. Turley, B. Ty, E. Unger, M. A. Unland Elorrieta, M. Usner, J. Vandenbroucke, W. Van Driessche, D. van Eijk, N. van Eijndhoven, S. Vanheule, J. van Santen, M. Vraeghe, C. Walck, A. Wallace, M. Wallraff, F. D. Wandler, N. Wandkowsky, T. B. Watson, C. Weaver, M. J. Weiss, C. Wendt, J. Werthebach, S. Westerhoff, B. J. Whelan, N. Whitehorn, K. Wiebe, C. H. Wiebusch, L. Wille, D. R. Williams, L. Wills, M. Wolf, J. Wood, T. R. Wood, E. Woolsey, K. Woschnagg, G. Wrede, D. L. Xu, X. W. Xu, Y. Xu, J. P. Yanez, G. Yodh, S. Yoshida and T. Yuan, "Search for steady point-like sources in the astrophysical muon neutrino flux with 8 years of IceCube data", European Physical Journal C **79**, 3, 234 (2019).

Aartsen, M. G., M. Ackermann, J. Adams, J. A. Aguilar, M. Ahlers, M. Ahrens, D. Altmann, T. Anderson, C. Arguelles, T. C. Arlen and et al., "Observation of High-Energy Astrophysical Neutrinos in Three Years of IceCube Data", Phys. Rev. Lett. **113**, 10, 101101 (2014b).

Aartsen, M. G., M. Ackermann, J. Adams, J. A. Aguilar, M. Ahlers, M. Ahrens, I. A. Samarai, D. Altmann, K. Andeen, T. Anderson, I. Ansseau, G. Anton, C. Argüelles, J. Auffenberg, S. Axani, H. Bagherpour, X. Bai, S. W. Barwick, V. Baum, R. Bay, J. J. Beatty, J. Becker Tjus, K. H. Becker, S. BenZvi, D. Berley, E. Bernardini, D. Z. Besson, G. Binder, D. Bindig, E. Blaufuss, S. Blot, C. Bohm, M. Börner, F. Bos, D. Bose, S. Böser, O. Botner, J. Bourbeau, F. Bradascio, J. Braun, L. Brayeur, M. Brenzke, H. P. Bretz, S. Bron, A. Burgman, T. Carver, J. Casey, M. Casier, E. Cheung, D. Chirkin, A. Christov, K. Clark, L. Classen, S. Coenders, G. H. Collin, J. M. Conrad, D. F. Cowen, R. Cross, M. Day, J. P. A. M. de André, C. De Clercq, J. J. DeLaunay, H. Dembinski, S. De Ridder, P. Desiati, K. D. de Vries, G. de Wasseige, M. de With, T. DeYoung, J. C. Díaz-Vélez, V. di Lorenzo, H. Dujmovic, J. P. Dumm, M. Dunkman, B. Eberhardt, T. Ehrhardt, B. Eichmann, P. Eller, P. A. Evenson, S. Fahey, A. R. Fazely, J. Felde, K. Filimonov, C. Finley, S. Flis, A. Franckowiak, E. Friedman, T. Fuchs, T. K. Gaisser, J. Gallagher, L. Gerhardt, K. Ghorbani, W. Giang, T. Glauch, T. Glüsenkamp, A. Goldschmidt, J. G. Gonzalez, D. Grant, Z. Griffith, C. Haack, A. Hallgren, F. Halzen, K. Hanson, D. Hebecker, D. Heereman, K. Helbing, R. Hellauer, S. Hickford, J. Hignight, G. C. Hill, K. D. Hoffman, R. Hoffmann, B. Hokanson-Fasig, K. Hoshina, F. Huang, M. Huber, K. Hultqvist, S. In, A. Ishihara, E. Jacobi, G. S. Japaridze, M. Jeong, K. Jero, B. J. P. Jones, P. Kalacynski, W. Kang, A. Kappes, T. Karg, A. Karle, U. Katz, M. Kauer, A. Keivani, J. L. Kelley, A. Kheirandish, J. Kim, M. Kim, T. Kintscher, J. Kiryluk, T. Kittler, S. R. Klein, G. Kohnen, R. Koirala, H. Kolanoski, L. Köpke, C. Kopper, S. Kopper, J. P. Koschinsky, D. J. Koskinen, M. Kowalski, K. Krings, M. Kroll, G. Krückl, J. Kunnen, S. Kunwar, N. Kurahashi, T. Kuwabara, A. Kyriacou, M. Labare, J. L. Lanfranchi, M. J. Larson, F. Lauber, D. Lennarz, M. Lesiak-Bzdak, M. Leuermann, Q. R. Liu, L. Lu, J. Lünemann, W. Luszczak, J. Madsen, G. Maggi, K. B. M. Mahn, S. Mancina, R. Maruyama, K. Mase, R. Maunu, F. McNally, K. Meagher, M. Medici, M. Meier, T. Menne, G. Merino, T. Meures, S. Miarecki, J. Micallef, G. Momenté, T. Montaruli, M. Moulai, R. Nahnhauer, P. Nakarmi, U. Naumann, G. Neer, H. Niederhausen, S. C. Nowicki, D. R. Nygren, A. Obertacke Pollmann,

A. Olivas, A. O'Murchadha, T. Palczewski, H. Pandya, D. V. Pankova, P. Peiffer, J. A. Pepper, C. Pérez de los Heros, D. Pieloth, E. Pinat, M. Plum, P. B. Price, G. T. Przybylski, C. Raab, L. Rädel, M. Rameez, K. Rawlins, R. Reimann, B. Relethford, M. Relich, E. Resconi, W. Rhode, M. Richman, B. Riedel, S. Robertson, M. Rongen, C. Rott, T. Ruhe, D. Ryckbosch, D. Rysewyk, T. Sälzer, S. E. Sanchez Herrera, A. Sandrock, J. Sand roos, S. Sarkar, S. Sarkar, K. Satalecka, P. Schlunder, T. Schmidt, A. Schneider, S. Schoenen, S. Schöneberg, L. Schumacher, D. Seckel, S. Seunarine, D. Soldin, M. Song, G. M. Spiczak, C. Spiering, J. Stachurska, T. Stanev, A. Stasik, J. Stettner, A. Steuer, T. Stezelberger, R. G. Stokstad, A. Stößl, N. L. Strotjohann, G. W. Sullivan, M. Sutherland, I. Taboada, J. Tatar, F. Tenholt, S. Ter-Antonyan, A. Terliuk, G. Tešić, S. Tilav, P. A. Toale, M. N. Tobin, S. Toscano, D. Tosi, M. Tselengidou, C. F. Tung, A. Turcati, C. F. Turley, B. Ty, E. Unger, M. Usner, J. Vand enbroucke, W. Van Driessche, N. van Eijndhoven, S. Vanheule, J. van Santen, M. Vehring, E. Vogel, M. Vraeghe, C. Walck, A. Wallace, M. Wallraff, N. Wandkowsky, A. Waza, C. Weaver, M. J. Weiss, C. Wendt, S. Westerhoff, B. J. Whelan, S. Wickmann, K. Wiebe, C. H. Wiebusch, L. Wille, D. R. Williams, L. Wills, M. Wolf, J. Wood, T. R. Wood, E. Woolsey, K. Woschnagg, D. L. Xu, X. W. Xu, Y. Xu, J. P. Yanez, G. Yodh, S. Yoshida, T. Yuan, M. Zoll and IceCube Collaboration, "Search for Astrophysical Sources of Neutrinos Using Cascade Events in IceCube", Astrophys. J. **846**, 2, 136 (2017d).

Aartsen, M. G., M. Ackermann, J. Adams, J. A. Aguilar, M. Ahlers, M. Ahrens, I. A. Samarai, D. Altmann, K. Andeen, T. Anderson and et al., "Constraints on Galactic Neutrino Emission with Seven Years of IceCube Data", Astrophys. J. **849**, 1, 67 (2017e).

Abdo, A. A., M. Ackermann, M. Ajello, A. Allafort, L. Baldini, J. Ballet, G. Barbiellini, M. G. Baring, D. Bastieri, R. Bellazzini, B. Berenji, R. D. Blandford, E. D. Bloom, E. Bonamente, A. W. Borgland, A. Bouvier, T. J. Brandt, J. Bregeon, M. Brigida, P. Bruel, R. Buehler, S. Buson, G. A. Caliandro, R. A. Cameron, P. A. Caraveo, J. M. Casandjian, C. Cecchi, S. Chaty, A. Chekhtman, C. C. Cheung, J. Chiang, A. N. Cillis, S. Ciprini, R. Claus, J. Cohen-Tanugi, J. Conrad, S. Corbel, S. Cutini, A. de Angelis, F. de Palma, C. D. Dermer, S. W. Digel, E. d. C. e. Silva, P. S. Drell, A. Drlica-Wagner, R. Dubois, D. Dumora, C. Favuzzi, E. C. Ferrara, P. Fortin, M. Frailis, Y. Fukazawa, Y. Fukui, S. Funk, P. Fusco, F. Gargano, D. Gasparrini, N. Gehrels, S. Germani, N. Giglietto, F. Giordano, M. Giroletti, T. Glanzman, G. Godfrey, I. A. Grenier, M. H. Grondin, S. Guiriec, D. Hadasch, Y. Hanabata, A. K. Harding, M. Hayashida, K. Hayashi, E. Hays, D. Horan, M. S. Jackson, G. Jóhannesson, A. S. Johnson, T. Kamae, H. Katagiri, J. Kataoka, M. Kerr, J. Knödlseder, M. Kuss, J. Lande, L. Latronico, S. H. Lee, M. Lemoine-Goumard, F. Longo, F. Loparco, M. N. Lovellette, P. Lubrano, G. M. Madejski, A. Makeev, M. N. Mazziotta, J. E. McEnery, P. F. Michelson, R. P. Mignani, W. Mitthumsiri, T. Mizuno, A. A. Moiseev, C. Monte, M. E. Monzani, A. Morselli, I. V. Moskalenko, S. Murgia, M. Naumann-Godo, P. L. Nolan, J. P. Norris, E. Nuss, T. Ohsugi, A. Okumura, E. Orlando, J. F. Ormes, D. Paneque, D. Parent, V. Pelassa, M. Pesce-Rollins, M. Pierbattista, F. Piron, M. Pohl, T. A. Porter, S. Rainò, R. Rando, M. Razzano, O. Reimer, T. Reposeur, S. Ritz, R. W. Romani, M. Roth, H. F. W. Sadrozinski, P. M. Saz Parkinson, C. Sgrò, D. A. Smith,

P. D. Smith, G. Spandre, P. Spinelli, M. S. Strickman, H. Tajima, H. Takahashi, T. Takahashi, T. Tanaka, J. G. Thayer, J. B. Thayer, D. J. Thompson, L. Tibaldo, O. Tibolla, D. F. Torres, G. Tosti, A. Tramacere, E. Troja, Y. Uchiyama, J. Vandenbroucke, V. Vasileiou, G. Vianello, N. Vilchez, V. Vitale, A. P. Waite, P. Wang, B. L. Winer, K. S. Wood, H. Yamamoto, R. Yamazaki, Z. Yang and M. Ziegler, "Observations of the Young Supernova Remnant RX J1713.7-3946 with the Fermi Large Area Telescope", Astrophys. J. **734**, 1, 28 (2011).

Abdo, A. A., M. Ackermann, M. Ajello, W. B. Atwood, M. Axelsson, L. Baldini, J. Ballet, D. L. Band, G. Barbiellini, D. Bastieri, M. Battelino, B. M. Baughman, K. Bechtol, R. Bellazzini, B. Berenji, G. F. Bignami, R. D. Blandford, E. D. Bloom, E. Bonamente, A. W. Borgland, A. Bouvier, J. Bregeon, A. Brez, M. Brigida, P. Bruel, T. H. Burnett, G. A. Caliandro, R. A. Cameron, P. A. Caraveo, J. M. Casandjian, E. Cavazzuti, C. Cecchi, E. Charles, A. Chekhtman, C. C. Cheung, J. Chiang, S. Ciprini, R. Claus, J. Cohen-Tanugi, L. R. Cominsky, J. Conrad, R. Corbet, L. Costamante, S. Cutini, D. S. Davis, C. D. Dermer, A. de Angelis, A. de Luca, F. de Palma, S. W. Digel, M. Dormody, E. do Couto e Silva, P. S. Drell, R. Dubois, D. Dumora, C. Farnier, C. Favuzzi, S. J. Fegan, E. C. Ferrara, W. B. Focke, M. Frailis, Y. Fukazawa, S. Funk, P. Fusco, F. Gargano, D. Gasparrini, N. Gehrels, S. Germani, B. Giebels, N. Giglietto, P. Giommi, F. Giordano, T. Glanzman, G. Godfrey, I. A. Grenier, M. H. Grondin, J. E. Grove, L. Guillemot, S. Guiriec, Y. Hanabata, A. K. Harding, R. C. Hartman, M. Hayashida, E. Hays, S. E. Healey, D. Horan, R. E. Hughes, G. Jóhannesson, A. S. Johnson, R. P. Johnson, T. J. Johnson, W. N. Johnson, T. Kamae, H. Katagiri, J. Kataoka, N. Kawai, M. Kerr, J. Knödlseder, D. Kocevski, M. L. Kocian, N. Komin, F. Kuehn, M. Kuss, J. Lande, L. Latronico, S. H. Lee, M. Lemoine-Goumard, F. Longo, F. Loparco, B. Lott, M. N. Lovellette, P. Lubrano, G. M. Madejski, A. Makeev, M. Marelli, M. N. Mazziotta, W. McConville, J. E. McEnery, S. McGlynn, C. Meurer, P. F. Michelson, W. Mitthumsiri, T. Mizuno, A. A. Moiseev, C. Monte, M. E. Monzani, E. Moretti, A. Morselli, I. V. Moskalenko, S. Murgia, T. Nakamori, P. L. Nolan, J. P. Norris, E. Nuss, M. Ohno, T. Ohsugi, N. Omodei, E. Orlando, J. F. Ormes, M. Ozaki, D. Paneque, J. H. Panetta, D. Parent, V. Pelassa, M. Pepe, M. Pesce-Rollins, F. Piron, T. A. Porter, L. Poupard, S. Rainò, R. Rando, P. S. Ray, M. Razzano, N. Rea, A. Reimer, O. Reimer, T. Reposeur, S. Ritz, L. S. Rochester, A. Y. Rodriguez, R. W. Romani, M. Roth, F. Ryde, H. F. W. Sadrozinski, D. Sanchez, A. Sander, P. M. Saz Parkinson, J. D. Scargle, T. L. Schalk, A. Sellerholm, C. Sgrò, M. S. Shaw, C. Shrader, A. Sierpowska-Bartosik, E. J. Siskind, D. A. Smith, P. D. Smith, G. Spandre, P. Spinelli, J. L. Starck, T. E. Stephens, M. S. Strickman, A. W. Strong, D. J. Suson, H. Tajima, H. Takahashi, T. Takahashi, T. Tanaka, J. B. Thayer, J. G. Thayer, D. J. Thompson, L. Tibaldo, O. Tibolla, D. F. Torres, G. Tosti, A. Tramacere, Y. Uchiyama, T. L. Usher, A. Van Etten, N. Vilchez, V. Vitale, A. P. Waite, E. Wallace, P. Wang, K. Watters, B. L. Winer, K. S. Wood, T. Ylinen, M. Ziegler and Fermi/LAT Collaboration, "Fermi/Large Area Telescope Bright Gamma-Ray Source List", Astrophys. J. Suppl. **183**, 1, 46–66 (2009).

Abeysekara, A. U., A. Albert, R. Alfaro, C. Alvarez, J. R. A. Camacho, J. C. Arteaga-Velázquez, K. P. Arunbabu, D. A. Rojas, H. A. A. Solares, V. Baghmanyan, E. Belmont-Moreno, S. Y. BenZvi, R. Blandford, C. Brisbois, K. S. Caballero-

Mora, T. Capistrán, A. Carramiñana, S. Casanova, U. Cotti, S. C. d. León, E. De la Fuente, R. D. Hernandez, B. L. Dingus, M. A. DuVernois, M. Durocher, J. C. Díaz-Vélez, R. W. Ellsworth, K. Engel, C. Espinoza, K. L. Fan, K. Fang, H. Fleischhack, N. Fraija, A. Galván-Gámez, D. Garcia, J. A. García-González, F. Garfias, G. Giacinti, M. M. González, J. A. Goodman, J. P. Harding, S. Hernandez, J. Hinton, B. Hona, D. Huang, F. Hueyotl-Zahuantitla, P. Hüntemeyer, A. Iriarte, A. Jardin-Blicq, V. Joshi, D. Kieda, A. Lara, W. H. Lee, H. L. Vargas, J. T. Linnemann, A. L. Longinotti, G. Luis-Raya, J. Lundeen, K. Malone, O. Martinez, I. Martinez-Castellanos, J. Martínez-Castro, J. A. Matthews, P. Miranda-Romagnoli, J. A. Morales-Soto, E. Moreno, M. Mostafá, A. Nayerhoda, L. Nellen, M. Newbold, M. U. Nisa, R. Noriega-Papaqui, L. Olivera-Nieto, N. Omodei, A. Peisker, Y. Pérez Araujo, E. G. Pérez-Pérez, Z. Ren, C. D. Rho, D. Rosa-González, E. Ruiz-Velasco, H. Salazar, F. S. Greus, A. Sandoval, M. Schneider, H. Schoorlemmer, F. Serna, A. J. Smith, R. W. Springer, P. Surajbali, K. Tollefson, I. Torres, R. Torres-Escobedo, F. Ureña-Mena, T. Weisgarber, F. Werner, E. Willox, A. Zepeda, H. Zhou, C. De León and J. D. Álvarez, "HAWC observations of the acceleration of very-high-energy cosmic rays in the Cygnus Cocoon", Nature Astronomy **5**, 465–471 (2021).

Abramowski, A., F. Acero, F. Aharonian, A. G. Akhperjanian, G. Anton, A. Balzer, A. Barnacka, U. Barres de Almeida, Y. Becherini, J. Becker, B. Behera, K. Bernlöhr, E. Birsin, J. Biteau, A. Bochow, C. Boisson, J. Bolmont, P. Bordas, J. Brucker, F. Brun, P. Brun, T. Bulik, I. Büsching, S. Carrigan, S. Casanova, M. Cerruti, P. M. Chadwick, A. Charbonnier, R. C. G. Chaves, A. Cheesebrough, L. M. Chounet, A. C. Clapson, G. Coignet, G. Cologna, J. Conrad, M. Dalton, M. K. Daniel, I. D. Davids, B. Degrange, C. Deil, H. J. Dickinson, A. Djannati-Ataï, W. Domainko, L. O'C. Drury, F. Dubois, G. Dubus, K. Dutson, J. Dyks, M. Dyrda, K. Egberts, P. Eger, P. Espigat, L. Fallon, C. Farnier, S. Fegan, F. Feinstein, M. V. Fernandes, A. Fiasson, G. Fontaine, A. Förster, M. Füßling, Y. A. Gallant, H. Gast, L. Gérard, D. Gerbig, B. Giebels, J. F. Glicenstein, B. Glück, P. Goret, D. Göring, S. Häffner, J. D. Hague, D. Hampf, M. Hauser, S. Heinz, G. Heinzelmann, G. Henri, G. Hermann, J. A. Hinton, A. Hoffmann, W. Hofmann, P. Hofverberg, M. Holler, D. Horns, A. Jacholkowska, O. C. de Jager, C. Jahn, M. Jamrozy, I. Jung, M. A. Kastendieck, K. Katarzyński, U. Katz, S. Kaufmann, D. Keogh, D. Khangulyan, B. Khélifi, D. Klochkov, W. Kluźniak, T. Kneiske, N. Komin, K. Kosack, R. Kossakowski, H. Laffon, G. Lamanna, D. Lennarz, T. Lohse, A. Lopatin, C. C. Lu, V. Marandon, A. Marcowith, J. Masbou, D. Maurin, N. Maxted, M. Mayer, T. J. L. McComb, M. C. Medina, J. Méhault, R. Moderski, E. Moulin, C. L. Naumann, M. Naumann-Godo, M. de Naurois, D. Nedbal, D. Nekrassov, N. Nguyen, B. Nicholas, J. Niemiec, S. J. Nolan, S. Ohm, E. de Oña Wilhelmi, B. Opitz, M. Ostrowski, I. Oya, M. Panter, M. Paz Arribas, G. Pedaletti, G. Pelletier, P. O. Petrucci, S. Pita, G. Pühlhofer, M. Punch, A. Quirrenbach, M. Raue, S. M. Rayner, A. Reimer, O. Reimer, M. Renaud, R. de Los Reyes, F. Rieger, J. Ripken, L. Rob, S. Rosier-Lees, G. Rowell, B. Rudak, C. B. Rulten, J. Ruppel, V. Sahakian, D. Sanchez, A. Santangelo, R. Schlickeiser, F. M. Schöck, A. Schulz, U. Schwanke, S. Schwarzburg, S. Schwemmer, F. Sheidaei, M. Sikora, J. L. Skilton, H. Sol, G. Spengler, Ł. Stawarz, R. Steenkamp, C. Stegmann, F. Stinzing, K. Stycz, I. Sushch, A. Szostek, J. P. Tavernet, R. Terrier, M. Tluczykont, K. Valerius, C. van Eldik, G. Vasileiadis, C. Venter, J. P. Vialle, A. Viana, P. Vincent, H. J. Völk, F. Volpe, S. Vorobiov, M. Vorster, S. J. Wagner, M. Ward, R. White, A. Wierzcholska, M. Zacharias, A. Zajczyk, A. A. Zdziarski, A. Zech and H. S. Zechlin, "Discovery of extended VHE γ-ray emission from the vicinity of the young massive stellar cluster Westerlund 1", Astron. Astrophys. **537**, A114 (2012).

Acero, F., M. Ackermann, M. Ajello, L. Baldini, J. Ballet, G. Barbiellini, D. Bastieri, R. Bellazzini, E. Bissaldi, R. D. Blandford, E. D. Bloom, R. Bonino, E. Bottacini, T. J. Brandt, J. Bregeon, P. Bruel, R. Buehler, S. Buson, G. A. Caliandro, R. A. Cameron, R. Caputo, M. Caragiulo, P. A. Caraveo, J. M. Casandjian, E. Cavazzuti, C. Cecchi, A. Chekhtman, J. Chiang, G. Chiaro, S. Ciprini, R. Claus, J. M. Cohen, J. Cohen-Tanugi, L. R. Cominsky, B. Condon, J. Conrad, S. Cutini, F. D'Ammando, A. de Angelis, F. de Palma, R. Desiante, S. W. Digel, L. Di Venere, P. S. Drell, A. Drlica-Wagner, C. Favuzzi, E. C. Ferrara, A. Franckowiak, Y. Fukazawa, S. Funk, P. Fusco, F. Gargano, D. Gasparrini, N. Giglietto, P. Giommi, F. Giordano, M. Giroletti, T. Glanzman, G. Godfrey, G. A. Gomez-Vargas, I. A. Grenier, M.-H. Grondin, L. Guillemot, S. Guiriec, M. Gustafsson, D. Hadasch, A. K. Harding, M. Hayashida, E. Hays, J. W. Hewitt, A. B. Hill, D. Horan, X. Hou, G. Iafrate, T. Jogler, G. Jóhannesson, A. S. Johnson, T. Kamae, H. Katagiri, J. Kataoka, J. Katsuta, M. Kerr, J. Knödlseder, D. Kocevski, M. Kuss, H. Laffon, J. Lande, S. Larsson, L. Latronico, M. Lemoine-Goumard, J. Li, L. Li, F. Longo, F. Loparco, M. N. Lovellette, P. Lubrano, J. Magill, S. Maldera, M. Marelli, M. Mayer, M. N. Mazziotta, P. F. Michelson, W. Mitthumsiri, T. Mizuno, A. A. Moiseev, M. E. Monzani, E. Moretti, A. Morselli, I. V. Moskalenko, S. Murgia, R. Nemmen, E. Nuss, T. Ohsugi, N. Omodei, M. Orienti, E. Orlando, J. F. Ormes, D. Paneque, J. S. Perkins, M. Pesce-Rollins, V. Petrosian, F. Piron, G. Pivato, T. A. Porter, S. Rainò, R. Rando, M. Razzano, S. Razzaque, A. Reimer, O. Reimer, M. Renaud, T. Reposeur, R. Rousseau, P. M. Saz Parkinson, J. Schmid, A. Schulz, C. Sgrò, E. J. Siskind, F. Spada, G. Spandre, P. Spinelli, A. W. Strong, D. J. Suson, H. Tajima, H. Takahashi, T. Tanaka, J. B. Thayer, D. J. Thompson, L. Tibaldo, O. Tibolla, D. F. Torres, G. Tosti, E. Troja, Y. Uchiyama, G. Vianello, B. Wells, K. S. Wood, M. Wood, M. Yassine, P. R. den Hartog and S. Zimmer, "The First Fermi LAT Supernova Remnant Catalog", Astrophys. J. Suppl. **224**, 8 (2016).

Ackermann, M., M. Ajello, A. Allafort, L. Baldini, J. Ballet, G. Barbiellini, M. G. Baring, D. Bastieri, K. Bechtol, R. Bellazzini, R. D. Blandford, E. D. Bloom, E. Bonamente, A. W. Borgland, E. Bottacini, T. J. Brandt, J. Bregeon, M. Brigida, P. Bruel, R. Buehler, G. Busetto, S. Buson, G. A. Caliandro, R. A. Cameron, P. A. Caraveo, J. M. Casandjian, C. Cecchi, Ö. Çelik, E. Charles, S. Chaty, R. C. G. Chaves, A. Chekhtman, C. C. Cheung, J. Chiang, G. Chiaro, A. N. Cillis, S. Ciprini, R. Claus, J. Cohen-Tanugi, L. R. Cominsky, J. Conrad, S. Corbel, S. Cutini, F. D'Ammando, A. de Angelis, F. de Palma, C. D. Dermer, E. do Couto e Silva, P. S. Drell, A. Drlica-Wagner, L. Falletti, C. Favuzzi, E. C. Ferrara, A. Franckowiak, Y. Fukazawa, S. Funk, P. Fusco, F. Gargano, S. Germani, N. Giglietto, P. Giommi, F. Giordano, M. Giroletti, T. Glanzman, G. Godfrey,

I. A. Grenier, M. H. Grondin, J. E. Grove, S. Guiriec, D. Hadasch, Y. Hanabata, A. K. Harding, M. Hayashida, K. Hayashi, E. Hays, J. W. Hewitt, A. B. Hill, R. E. Hughes, M. S. Jackson, T. Jogler, G. Jóhannesson, A. S. Johnson, T. Kamae, J. Kataoka, J. Katsuta, J. Knödlseder, M. Kuss, J. Lande, S. Larsson, L. Latronico, M. Lemoine-Goumard, F. Longo, F. Loparco, M. N. Lovellette, P. Lubrano, G. M. Madejski, F. Massaro, M. Mayer, M. N. Mazziotta, J. E. McEnery, J. Mehault, P. F. Michelson, R. P. Mignani, W. Mitthumsiri, T. Mizuno, A. A. Moiseev, M. E. Monzani, A. Morselli, I. V. Moskalenko, S. Murgia, T. Nakamori, R. Nemmen, E. Nuss, M. Ohno, T. Ohsugi, N. Omodei, M. Orienti, E. Orlando, J. F. Ormes, D. Paneque, J. S. Perkins, M. Pesce-Rollins, F. Piron, G. Pivato, S. Rainò, R. Rando, M. Razzano, S. Razzaque, A. Reimer, O. Reimer, S. Ritz, C. Romoli, M. Sánchez-Conde, A. Schulz, C. Sgrò, P. E. Simeon, E. J. Siskind, D. A. Smith, G. Spandre, P. Spinelli, F. W. Stecker, A. W. Strong, D. J. Suson, H. Tajima, H. Takahashi, T. Takahashi, T. Tanaka, J. G. Thayer, J. B. Thayer, D. J. Thompson, S. E. Thorsett, L. Tibaldo, O. Tibolla, M. Tinivella, E. Troja, Y. Uchiyama, T. L. Usher, J. Vandenbroucke, V. Vasileiou, G. Vianello, V. Vitale, A. P. Waite, M. Werner, B. L. Winer, K. S. Wood, M. Wood, R. Yamazaki, Z. Yang and S. Zimmer, "Detection of the Characteristic Pion-Decay Signature in Supernova Remnants", Science **339**, 6121, 807–811 (2013).

Adrián-Martínez, S., M. Ageron, F. Aharonian, S. Aiello, A. Albert, F. Ameli, E. Anassontzis, M. Andre, G. Androulakis, M. Anghinolfi, G. Anton, M. Ardid, T. Avgitas, G. Barbarino, E. Barbarito, B. Baret, J. Barrios-Martí, B. Belhorma, A. Belias, E. Berbee, A. van den Berg, V. Bertin, S. Beurthey, V. van Beveren, N. Beverini, S. Biagi, A. Biagioni, M. Billault, M. Bondì, R. Bormuth, B. Bouhadef, G. Bourlis, S. Bourret, C. Boutonnet, M. Bouwhuis, C. Bozza, R. Bruijn, J. Brunner, E. Buis, J. Busto, G. Cacopardo, L. Caillat, M. Calamai, D. Calvo, A. Capone, L. Caramete, S. Cecchini, S. Celli, C. Champion, R. Cherkaoui El Moursli, S. Cherubini, T. Chiarusi, M. Circella, L. Classen, R. Cocimano, J. A. B. Coelho, A. Coleiro, S. Colonges, R. Coniglione, M. Cordelli, A. Cosquer, P. Coyle, A. Creusot, G. Cuttone, A. D'Amico, G. De Bonis, G. De Rosa, C. De Sio, F. Di Capua, I. Di Palma, A. F. Díaz García, C. Distefano, C. Donzaud, D. Dornic, Q. Dorosti-Hasankiadeh, E. Drakopoulou, D. Drouhin, L. Drury, M. Durocher, T. Eberl, S. Eichie, D. van Eijk, I. El Bojaddaini, N. El Khayati, D. Elsaesser, A. Enzenhöfer, F. Fassi, P. Favali, P. Fermani, G. Ferrara, C. Filippidis, G. Frascadore, L. A. Fusco, T. Gal, S. Galatà, F. Garufi, P. Gay, M. Gebyehu, V. Giordano, N. Gizani, R. Gracia, K. Graf, T. Grégoire, G. Grella, R. Habel, S. Hallmann, H. van Haren, S. Harissopulos, T. Heid, A. Heijboer, E. Heine, S. Henry, J. J. Hernández-Rey, M. Hevinga, J. Hofestädt, C. M. F. Hugon, G. Illuminati, C. W. James, P. Jansweijer, M. Jongen, M. de Jong, M. Kadler, O. Kalekin, A. Kappes, U. F. Katz, P. Keller, G. Kieft, D. Kießling, E. N. Koffeman, P. Kooijman, A. Kouchner, V. Kulikovskiy, R. Lahmann, P. Lamare, A. Leisos, E. Leonora, M. L. Clark, A. Liolios, C. D. Llorens Alvarez, D. Lo Presti, H. Löhner, A. Lonardo, M. Lotze, S. Loucatos, E. Maccioni, K. Mannheim, A. Margiotta, A. Marinelli, O. Mariş, C. Markou, J. A. Martínez-Mora, A. Martini, R. Mele, K. W. Melis, T. Michael, P. Migliozzi, E. Migneco, P. Mijakowski, A. Miraglia, C. M. Mollo, M. Mongelli, M. Morganti, A. Moussa, P. Musico, M. Musumeci, S. Navas, C. A. Nicolau, I. Olcina, C. Olivetto, A. Orlando, A. Papaikonomou, R. Papaleo, G. E.

Păvălaş, H. Peek, C. Pellegrino, C. Perrina, M. Pfutzner, P. Piattelli, K. Pikounis, G. E. Poma, V. Popa, T. Pradier, F. Pratolongo, G. Pühlhofer, S. Pulvirenti, L. Quinn, C. Racca, F. Raffaelli, N. Randazzo, P. Rapidis, P. Razis, D. Real, L. Resvanis, J. Reubelt, G. Riccobene, C. Rossi, A. Rovelli, M. Saldaña, I. Salvadori, D. F. E. Samtleben, A. Sánchez García, A. Sánchez Losa, M. Sanguineti, A. Santangelo, D. Santonocito, P. Sapienza, F. Schimmel, J. Schmelling, V. Sciacca, M. Sedita, T. Seitz, I. Sgura, F. Simeone, I. Siotis, V. Sipala, B. Spisso, M. Spurio, G. Stavropoulos, J. Steijger, S. M. Stellacci, D. Stransky, M. Taiuti, Y. Tayalati, D. Tézier, S. Theraube, L. Thompson, P. Timmer, C. Tönnis, L. Trasatti, A. Trovato, A. Tsirigotis, S. Tzamarias, E. Tzamariudaki, B. Vallage, V. Van Elewyck, J. Vermeulen, P. Vicini, S. Viola, D. Vivolo, M. Volkert, G. Voulgaris, L. Wiggers, J. Wilms, E. de Wolf, K. Zachariadou, J. D. Zornoza and J. Zúñiga, "Letter of intent for KM3NeT 2.0", Journal of Physics G Nuclear Physics **43**, 8, 084001 (2016).

Aharonian, F., A. Akhperjanian, M. Beilicke, K. Bernlöhr, H. Börst, H. Bojahr, O. Bolz, T. Coarasa, J. Contreras, J. Cortina, S. Denninghoff, V. Fonseca, M. Girma, N. Götting, G. Heinzelmann, G. Hermann, A. Heusler, W. Hofmann, D. Horns, I. Jung, R. Kankanyan, M. Kestel, J. Kettler, A. Kohnle, A. Konopelko, H. Kornmeyer, D. Kranich, H. Krawczynski, H. Lampeitl, M. Lopez, E. Lorenz, F. Lucarelli, N. Magnussen, O. Mang, H. Meyer, M. Milite, R. Mirzoyan, A. Moralejo, E. Ona, M. Panter, A. Plyasheshnikov, J. Prahl, G. Pühlhofer, G. Rauterberg, R. Reyes, W. Rhode, J. Ripken, A. Röhring, G. P. Rowell, V. Sahakian, M. Samorski, M. Schilling, F. Schröder, M. Siems, D. Sobzynska, W. Stamm, M. Tluczykont, H. J. Völk, C. A. Wiedner, W. Wittek, Y. Uchiyama, T. Takahashi and HEGRA Collaboration, "An unidentified TeV source in the vicinity of Cygnus OB2", Astron. Astrophys. **393**, L37–L40 (2002).

Aharonian, F., A. G. Akhperjanian, A. R. Bazer-Bachi, M. Beilicke, W. Benbow, D. Berge, K. Bernlöhr, C. Boisson, O. Bolz, V. Borrel, I. Braun, E. Brion, A. M. Brown, R. Bühler, I. Büsching, T. Boutelier, S. Carrigan, P. M. Chadwick, L. M. Chounet, G. Coignet, R. Cornils, L. Costamante, B. Degrange, H. J. Dickinson, A. Djannati-Ataï, L. O. Drury, G. Dubus, K. Egberts, D. Emmanoulopoulos, P. Espigat, C. Farnier, F. Feinstein, E. Ferrero, A. Fiasson, G. Fontaine, S. Funk, S. Funk, M. Füßling, Y. A. Gallant, B. Giebels, J. F. Glicenstein, B. Glück, P. Goret, C. Hadjichristidis, D. Hauser, M. Hauser, G. Heinzelmann, G. Henri, G. Hermann, J. A. Hinton, A. Hoffmann, W. Hofmann, M. Holleran, S. Hoppe, D. Horns, A. Jacholkowska, O. C. de Jager, E. Kendziorra, M. Kerschhaggl, B. Khélifi, N. Komin, K. Kosack, G. Lamanna, I. J. Latham, R. Le Gallou, A. Lemière, M. Lemoine-Goumard, T. Lohse, J. M. Martin, O. Martineau-Huynh, A. Marcowith, C. Masterson, G. Maurin, T. J. L. McComb, E. Moulin, M. de Naurois, D. Nedbal, S. J. Nolan, A. Noutsos, J. P. Olive, K. J. Orford, J. L. Osborne, M. Panter, G. Pelletier, P. O. Petrucci, S. Pita, G. Pühlhofer, M. Punch, S. Ranchon, B. C. Raubenheimer, M. Raue, S. M. Rayner, A. Reimer, O. Reimer, J. Ripken, L. Rob, L. Rolland, S. Rosier-Lees, G. Rowell, V. Sahakian, A. Santangelo, L. Saugé, S. Schlenker, R. Schlickeiser, R. Schröder, U. Schwanke, S. Schwarzburg, S. Schwemmer, A. Shalchi, H. Sol, D. Spangler, F. Spanier, R. Steenkamp, C. Stegmann, G. Superina, P. H. Tam, J. P. Tavernet, R. Terrier,

M. Tluczykont, C. van Eldik, G. Vasileiadis, C. Venter, J. P. Vialle, P. Vincent, H. J. Völk, S. J. Wagner and M. Ward, “Detection of extended very-high-energy γ-ray emission towards the young stellar cluster Westerlund 2”, Astron. Astrophys. **467**, 3, 1075–1080 (2007).

Ahlers, M., Y. Bai, V. Barger and R. Lu, “Galactic neutrinos in the TeV to PeV range”, Phys. Rev. D **93**, 1, 013009 (2016).

Ahlers, M. and F. Halzen, “Pinpointing extragalactic neutrino sources in light of recent IceCube observations”, Phys. Rev. D **90**, 4, 043005 (2014).

Ahlers, M. and F. Halzen, “Opening a new window onto the universe with IceCube”, Progress in Particle and Nuclear Physics **102**, 73–88 (2018).

Albert, A., M. André, M. Anghinolfi, G. Anton, M. Ardid, J. J. Aubert, J. Aublin, B. Baret, S. Basa, B. Belhorma, V. Bertin, S. Biagi, M. Bissinger, J. Boumaaza, S. Bourret, M. Bouta, M. C. Bouwhuis, H. Brânzaş, R. Bruijn, J. Brunner, J. Busto, A. Capone, L. Caramete, J. Carr, S. Celli, M. Chabab, T. N. Chau, R. C. El Moursli, T. Chiarusi, M. Circella, A. Coleiro, M. Colomer, R. Coniglione, H. Costantini, P. Coyle, A. Creusot, A. F. Díaz, G. De Wasseige, A. Deschamps, C. Distefano, I. di Palma, A. Domi, C. Donzaud, D. Dornic, D. Drouhin, T. Eberl, I. E. Bojaddaini, N. E. Khayati, D. Elsässer, A. Enzenhöfer, A. Ettahiri, F. Fassi, P. Fermani, G. Ferrara, F. Filippini, L. Fusco, P. Gay, H. Glotin, R. Gozzini, R. G. Ruiz, K. Graf, C. Guidi, S. Hallmann, H. van Haren, A. J. Heijboer, Y. Hello, J. J. Hernández-Rey, J. Hößl, J. Hofestädt, G. Illuminati, C. W. James, M. De Jong, P. De Jong, M. Jongen, M. Kadler, O. Kalekin, U. Katz, N. R. Khan-Chowdhury, A. Kouchner, M. Kreter, I. Kreykenbohm, V. Kulikovskiy, R. Lahmann, R. L. Breton, D. Lefèvre, E. Leonora, G. Levi, M. Lincetto, D. Lopez-Coto, S. Loucatos, G. Maggi, J. Manczak, M. Marcelin, A. Margiotta, A. Marinelli, J. A. Martínez-Mora, R. Mele, K. Melis, P. Migliozzi, M. Moser, A. Moussa, R. Muller, L. Nauta, S. Navas, E. Nezri, C. Nielsen, A. Nuñez-Castiñeyra, B. O’Fearraigh, M. Organokov, G. E. Păvălaş, C. Pellegrino, M. Perrin-Terrin, P. Piattelli, C. Poirè, V. Popa, T. Pradier, L. Quinn, N. Randazzo, G. Riccobene, A. Sánchez-Losa, A. Salah-Eddine, D. F. E. Samtleben, M. Sanguineti, P. Sapienza, F. Schüssler, M. Spurio, T. Stolarczyk, B. Strandberg, M. Taiuti, Y. Tayalati, T. Thakore, S. J. Tingay, A. Trovato, B. Vallage, V. van Elewyck, F. Versari, S. Viola, D. Vivolo, J. Wilms, D. Zaborov, A. Zegarelli, J. D. Zornoza, J. Zúñiga, ANTARES Collaboration, M. G. Aartsen, M. Ackermann, J. Adams, J. A. Aguilar, M. Ahlers, M. Ahrens, C. Alispach, K. Andeen, T. Anderson, I. Ansseau, G. Anton, C. Argüelles, J. Auffenberg, S. Axani, P. Backes, H. Bagherpour, X. Bai, A. V. Balagopal, A. Barbano, S. W. Barwick, B. Bastian, V. Baum, S. Baur, R. Bay, J. J. Beatty, K. H. Becker, J. B. Tjus, S. Benzvi, D. Berley, E. Bernardini, D. Z. Besson, G. Binder, D. Bindig, E. Blaufuss, S. Blot, C. Bohm, S. Böser, O. Botner, J. Böttcher, E. Bourbeau, J. Bourbeau, F. Bradascio, J. Braun, S. Bron, J. Brostean-Kaiser, A. Burgman, J. Buscher, R. S. Busse, T. Carver, C. Chen, E. Cheung, D. Chirkin, S. Choi, K. Clark, L. Classen, A. Coleman, G. H. Collin, J. M. Conrad, P. Coppin, P. Correa, D. F. Cowen, R. Cross, P. Dave, C. Clercq, J. J. Delaunay, H. Dembinski, K. Deoskar, S. De Ridder, P. Desiati, K. D. De

Vries, G. De Wasseige, M. De With, T. Deyoung, A. Diaz, J. C. Díaz-Vélez, H. Dujmovic, M. Dunkman, E. Dvorak, B. Eberhardt, T. Ehrhardt, P. Eller, R. Engel, P. A. Evenson, S. Fahey, A. R. Fazely, J. Felde, K. Filimonov, C. Finley, D. Fox, A. Franckowiak, E. Friedman, A. Fritz, T. K. Gaisser, J. Gallagher, E. Ganster, S. Garrappa, L. Gerhardt, K. Ghorbani, T. Glauch, T. Glüsenkamp, A. Goldschmidt, J. G. Gonzalez, D. Grant, T. Grégoire, Z. Griffith, S. Griswold, M. Günder, M. Gündüz, C. Haack, A. Hallgren, R. Halliday, L. Halve, F. Halzen, K. Hanson, A. Haungs, D. Hebecker, D. Heereman, P. Heix, K. Helbing, R. Hellauer, F. Henningsen, S. Hickford, J. Hignight, G. C. Hill, K. D. Hoffman, R. Hoffmann, T. Hoinka, B. Hokanson-Fasig, K. Hoshina, F. Huang, M. Huber, T. Huber, K. Hultqvist, M. Hünnefeld, R. Hussain, S. in, N. Iovine, A. Ishihara, M. Jansson, G. S. Japaridze, M. Jeong, K. Jero, B. J. P. Jones, F. Jonske, R. Joppe, D. Kang, W. Kang, A. Kappes, D. Kappesser, T. Karg, M. Karl, A. Karle, U. Katz, M. Kauer, J. L. Kelley, A. Kheirandish, J. Kim, T. Kintscher, J. Kiryluk, T. Kittler, S. R. Klein, R. Koirala, H. Kolanoski, L. Köpke, C. Kopper, S. Kopper, D. J. Koskinen, M. Kowalski, K. Krings, G. Krückl, N. Kulacz, N. Kurahashi, A. Kyriacou, J. L. Lanfranchi, M. J. Larson, F. Lauber, J. P. Lazar, K. Leonard, A. Leszczyńska, M. Leuermann, Q. R. Liu, E. Lohfink, C. J. Lozano Mariscal, L. Lu, F. Lucarelli, J. Lünemann, W. Luszczak, Y. Lyu, W. Y. Ma, J. Madsen, G. Maggi, K. B. M. Mahn, Y. Makino, P. Mallik, K. Mallot, S. Mancina, I. C. Mariş, R. Maruyama, K. Mase, R. Maunu, F. McNally, K. Meagher, M. Medici, A. Medina, M. Meier, S. Meighen-Berger, G. Merino, T. Meures, J. Micallef, D. Mockler, G. Momenté, T. Montaruli, R. W. Moore, R. Morse, M. Moulai, P. Muth, R. Nagai, U. Naumann, G. Neer, H. Niederhausen, M. U. Nisa, S. C. Nowicki, D. R. Nygren, A. Obertacke Pollmann, M. Oehler, A. Olivas, A. O'Murchadha, E. O'Sullivan, T. Palczewski, H. Pandya, D. V. Pankova, N. Park, P. Peiffer, C. P. de Los Heros, S. Philippen, D. Pieloth, S. Pieper, E. Pinat, A. Pizzuto, M. Plum, A. Porcelli, P. B. Price, G. T. Przybylski, C. Raab, A. Raissi, M. Rameez, L. Rauch, K. Rawlins, I. C. Rea, R. Reimann, B. Relethford, M. Renschler, G. Renzi, E. Resconi, W. Rhode, M. Richman, S. Robertson, M. Rongen, C. Rott, T. Ruhe, D. Ryckbosch, D. Rysewyk, I. Safa, S. E. Sanchez Herrera, A. Sandrock, J. Sandroos, M. Santander, S. Sarkar, S. Sarkar, K. Satalecka, M. Schaufel, H. Schieler, P. Schlunder, T. Schmidt, A. Schneider, J. Schneider, F. G. Schröder, L. Schumacher, S. Sclafani, D. Seckel, S. Seunarine, S. Shefali, M. Silva, R. Snihur, J. Soedingrekso, D. Soldin, M. Song, G. M. Spiczak, C. Spiering, J. Stachurska, M. Stamatikos, T. Stanev, R. Stein, J. Stettner, A. Steuer, T. Stezelberger, R. G. Stokstad, A. Stößl, N. L. Strotjohann, T. Stürwald, T. Stuttard, G. W. Sullivan, I. Taboada, F. Tenholt, S. Ter-Antonyan, A. Terliuk, S. Tilav, K. Tollefson, L. Tomankova, C. Tönnis, S. Toscano, D. Tosi, A. Trettin, M. Tselengidou, C. F. Tung, A. Turcati, R. Turcotte, C. F. Turley, B. Ty, E. Unger, M. A. Unland Elorrieta, M. Usner, J. Vandenbroucke, W. van Driessche, D. van Eijk, N. van Eijndhoven, J. van Santen, S. Verpoest, M. Vraeghe, C. Walck, A. Wallace, M. Wallraff, N. Wandkowsky, T. B. Watson, C. Weaver, A. Weindl, M. J. Weiss, J. Weldert, C. Wendt, J. Werthebach, B. J. Whelan, N. Whitehorn, K. Wiebe, C. H. Wiebusch, L. Wille, D. R. Williams, L. Wills, M. Wolf, J. Wood, T. R. Wood, K. Woschnagg, G. Wrede, D. L. Xu, X. W. Xu, Y. Xu, J. P. Yanez, G. Yodh, S. Yoshida, T. Yuan, M. Zöcklein and Icecube Collaboration, "ANTARES and IceCube Combined Search for Neutrino Point-like and Extended Sources in the Southern Sky", Astrophys. J. **892**, 2, 92 (2020).

Albert, A., M. André, M. Anghinolfi, G. Anton, M. Ardid, J. J. Aubert, T. Avgitas, B. Baret, J. Barrios-Martí, S. Basa, B. Belhorma, V. Bertin, S. Biagi, R. Bormuth, S. Bourret, M. C. Bouwhuis, R. Bruijn, J. Brunner, J. Busto, A. Capone, L. Caramete, J. Carr, S. Celli, R. Cherkaoui El Moursli, T. Chiarusi, M. Circella, J. A. B. Coelho, A. Coleiro, R. Coniglione, H. Costantini, P. Coyle, A. Creusot, A. F. Díaz, A. Deschamps, G. de Bonis, C. Distefano, I. di Palma, A. Domi, C. Donzaud, D. Dornic, D. Drouhin, T. Eberl, I. El Bojaddaini, N. El Khayati, D. Elsässer, A. Enzenhöfer, A. Ettahiri, F. Fassi, I. Felis, L. A. Fusco, S. Galatà, P. Gay, V. Giordano, H. Glotin, T. Grégoire, R. Gracia Ruiz, K. Graf, S. Hallmann, H. van Haren, A. J. Heijboer, Y. Hello, J. J. Hernández-Rey, J. Hößl, J. Hofestädt, C. Hugon, G. Illuminati, C. W. James, M. de Jong, M. Jongen, M. Kadler, O. Kalekin, U. Katz, D. Kießling, A. Kouchner, M. Kreter, I. Kreykenbohm, V. Kulikovskiy, C. Lachaud, R. Lahmann, D. Lefèvre, E. Leonora, M. Lotze, S. Loucatos, M. Marcelin, A. Margiotta, A. Marinelli, J. A. Martínez-Mora, R. Mele, K. Melis, T. Michael, P. Migliozzi, A. Moussa, S. Navas, E. Nezri, M. Organokov, G. E. Păvălaș, C. Pellegrino, C. Perrina, P. Piattelli, V. Popa, T. Pradier, L. Quinn, C. Racca, G. Riccobene, A. Sánchez-Losa, M. Saldaña, I. Salvadori, D. F. E. Samtleben, M. Sanguineti, P. Sapienza, F. Schüssler, C. Sieger, M. Spurio, T. Stolarczyk, M. Taiuti, Y. Tayalati, A. Trovato, D. Turpin, C. Tönnis, B. Vallage, V. van Elewyck, F. Versari, D. Vivolo, A. Vizzoca, J. Wilms, J. D. Zornoza, J. Zúñiga, D. Gaggero, D. Grasso and ANTARES Collaboration, "New constraints on all flavor Galactic diffuse neutrino emission with the ANTARES telescope", Phys. Rev. D **96**, 6, 062001 (2017).

Alexander, D. R. and J. W. Ferguson, "Low-temperature Rosseland opacities", Astrophys. J. **437**, 879–891 (1994a).

Alexander, D. R. and J. W. Ferguson, "Low-Temperature Rosseland Opacities", Astrophys. J. **437**, 879 (1994b).

Anchordoqui, L. A., H. Goldberg, T. C. Paul, L. H. M. da Silva and B. J. Vlcek, "Estimating the contribution of Galactic sources to the diffuse neutrino flux", Phys. Rev. D **90**, 12, 123010 (2014).

Angulo, C., M. Arnould, M. Rayet, P. Descouvemont, D. Baye, C. Leclercq-Willain, A. Coc, S. Barhoumi, P. Aguer, C. Rolfs, R. Kunz, J. W. Hammer, A. Mayer, T. Paradellis, S. Kossionides, C. Chronidou, K. Spyrou, S. degl'Innocenti, G. Fiorentini, B. Ricci, S. Zavatarelli, C. Providencia, H. Wolters, J. Soares, C. Grama, J. Rahighi, A. Shotter and M. Lamehi Rachti, "A compilation of charged-particle induced thermonuclear reaction rates", Nuclear Physics A **656**, 3–183 (1999).

Araya, M. and W. Cui, "Evidence for Cosmic Ray Acceleration in Cassiopeia A", Astrophys. J. **720**, 1, 20–25 (2010).

Arnett, D., *Supernovae and Nucleosynthesis: An Investigation of the History of Matter from the Big Bang to the Present* (1996).

Arnett, D., C. Meakin and P. A. Young, “Turbulent Convection in Stellar Interiors. II. The Velocity Field”, Astrophys. J. **690**, 1715–1729 (2009).

Arnett, D., C. Meakin and P. A. Young, “Convection Theory and Sub-Photospheric Stratification”, Astrophys. J. **710**, 1619–1626 (2010).

Arnett, W. D. and C. Meakin, “Toward Realistic Progenitors of Core-collapse Supernovae”, Astrophys. J. **733**, 78 (2011).

Arnett, W. D., C. Meakin, M. Viallet, S. W. Campbell, J. C. Lattanzio and M. Mocák, “Beyond Mixing-length Theory: A Step Toward 321D”, Astrophys. J. **809**, 1, 30 (2015).

Arnett, W. D. and E. Moravveji, “Synergies between Asteroseismology and Three-dimensional Simulations of Stellar Turbulence”, Astrophys. J. Lett. **836**, L19 (2017).

Bai, Y., R. Lu and J. Salvado, “Geometric compatibility of IceCube TeV-PeV neutrino excess and its galactic dark matter origin”, Journal of High Energy Physics **2016**, 161 (2016).

Beatty, J. J. and S. Westerhoff, “The Highest-Energy Cosmic Rays”, Annual Review of Nuclear and Particle Science **59**, 1, 319–345 (2009).

Bednarek, W., “TeV Neutrinos from Microquasars in Compact Massive Binaries”, Astrophys. J. **631**, 1, 466–470 (2005).

Bednarek, W. and J. Pabich, “High-energy radiation from the massive binary system Eta Carinae”, Astron. Astrophys. **530**, A49 (2011).

Bednarek, W., J. Pabich and T. Sobczak, “Gamma rays and neutrinos from dense environment of massive binary systems in open clusters”, Phys. Rev. D **90**, 10, 103008 (2014).

Bell, A. R., “Particle Acceleration by Shocks in Supernova Remnants”, Brazilian Journal of Physics **44**, 5, 415–425 (2014).

Benz, W., “3D models of rotating magnetic gas clouds. I - Time evolution, mass spectrum and angular momentum”, Astron. Astrophys. **139**, 378–388 (1984).

Benz, W., “Applications of smooth particle hydrodynamics (SPH) to astrophysical problems.”, Computer Physics Communications **48**, 97–105 (1988).

Benz, W., “Smooth Particle Hydrodynamics - a Review”, in “Proceedings of the NATO Advanced Research Workshop on The Numerical Modelling of Nonlinear Stellar Pulsations Problems and Prospects, held in Les Arcs, France, March 20-24, 1986. Editor, J. Robert Buchler; Publisher, Kluwer Academic Publishers, Dordrecht, The Netherlands, Boston, 1990. ISBN # 0-7923-0598-1. LC # QB812 .N376. P.269, 1990”, p. 269 (1990).

Benz, W., J. G. Hills and F.-K. Thielemann, "Three-dimensional hydrodynamical simulations of stellar collisions. II - White dwarfs", Astrophys. J. **342**, 986–998 (1989).

Berezhko, E. G., L. T. Ksenofontov and H. J. Völk, "The Nature of Gamma-Ray Emission of Tycho's Supernova Remnant", Astrophys. J. **763**, 1, 14 (2013).

Binney, J. and W. Dehnen, "The outer rotation curve of the Milky Way", Mon. Not. R. Astron. Soc. **287**, L5–L7 (1997).

Binns, W. R., M. E. Wiedenbeck, M. Arnould, A. C. Cummings, J. S. George, S. Goriely, M. H. Israel, R. A. Leske, R. A. Mewaldt, G. Meynet, L. M. Scott, E. C. Stone and T. T. von Rosenvinge, "Cosmic-Ray Neon, Wolf-Rayet Stars, and the Superbubble Origin of Galactic Cosmic Rays", Astrophys. J. **634**, 1, 351–364 (2005).

Blasi, P., "The origin of galactic cosmic rays", Astronomy and Astrophysics Review **21**, 70 (2013).

Bloecker, T., "Stellar evolution of low and intermediate-mass stars. I. Mass loss on the AGB and its consequences for stellar evolution.", Astron. Astrophys. **297**, 727 (1995).

Burrows, A., D. Vartanyan, J. C. Dolence, M. A. Skinner and D. Radice, "Crucial Physical Dependencies of the Core-Collapse Supernova Mechanism", Space Sci. Rev. **214**, 33 (2018).

Bykov, A. M., A. Brandenburg, M. A. Malkov and S. M. Osipov, "Microphysics of Cosmic Ray Driven Plasma Instabilities", Space Sci. Rev. **178**, 2-4, 201–232 (2013).

Bykov, A. M., D. C. Ellison, P. E. Gladilin and S. M. Osipov, "Ultrahard spectra of PeV neutrinos from supernovae in compact star clusters", Mon. Not. R. Astron. Soc. **453**, 1, 113–121 (2015).

Bykov, A. M., D. C. Ellison, P. E. Gladilin and S. M. Osipov, "Supernovae in compact star clusters as sources of high-energy cosmic rays and neutrinos", Advances in Space Research **62**, 10, 2764–2772 (2018).

Bykov, A. M., D. C. Ellison and M. Renaud, "Magnetic Fields in Cosmic Particle Acceleration Sources", Space Sci. Rev. **166**, 1-4, 71–95 (2012).

Cantat-Gaudin, T. and F. Anders, "Clusters and mirages: cataloguing stellar aggregates in the Milky Way", Astron. Astrophys. **633**, A99 (2020).

Chakraborty, S. and I. Izaguirre, "Star-forming galaxies as the origin of IceCube neutrinos: Reconciliation with Fermi-LAT gamma rays", arXiv e-prints p. arXiv:1607.03361 (2016).

Chevalier, R. A., "Supernova Remnants in Molecular Clouds", Astrophys. J. **511**, 2, 798–811 (1999).

Chevalier, R. A. and J. Oishi, “Cassiopeia A and Its Clumpy Presupernova Wind”, Astrophys. J. Lett. **593**, L23–L26 (2003).

Chirkin, D. and W. Rhode, “Propagating leptons through matter with Muon Monte Carlo (MMC)”, arXiv e-prints pp. hep–ph/0407075 (2004).

Claussen, M. J., D. A. Frail, W. M. Goss and R. A. Gaume, “Polarization Observations of 1720 MHz OH Masers toward the Three Supernova Remnants W28, W44, and IC 443”, Astrophys. J. **489**, 1, 143–159 (1997).

Colgate, S. A., M. Herant and W. Benz, “Neutron star accretion and the neutrino fireball”, Phys. Rep. **227**, 157–174 (1993).

Costado, M. T. and E. J. Alfaro, “Spatial and kinematic structure of Monoceros star-forming region”, Mon. Not. R. Astron. Soc. **476**, 3, 3160–3168 (2018).

Couch, S. M., E. Chatzopoulos, W. D. Arnett and F. X. Timmes, “The Three-dimensional Evolution to Core Collapse of a Massive Star”, Astrophys. J. Lett. **808**, 1, L21 (2015).

Danilenko, A., A. Karpova, D. Ofengeim, Y. Shibanov and D. Zyuzin, “XMM-Newton observations of a gamma-ray pulsar J0633+0632: pulsations, cooling and large-scale emission”, Mon. Not. R. Astron. Soc. **493**, 2, 1874–1887 (2020).

de Grijs, R., R. F. Peletier and P. C. van der Kruit, “The z-structure of disk galaxies towards the galaxy planes”, Astron. Astrophys. **327**, 966–982 (1997).

de Ruiter, H. R., A. G. Willis and H. C. Arp, “A Westerbork 1415 MHz survey of background radio sources. II. Optical identifications with deep IIIa-J plates.”, Astronomy and Astrophysics Supplement Series **28**, 211–293 (1977).

Delahaye, T., J. Lavalle, R. Lineros, F. Donato and N. Fornengo, “Galactic electrons and positrons at the Earth: new estimate of the primary and secondary fluxes”, Astron. Astrophys. **524**, A51 (2010).

Denton, P. B., D. Marfatia and T. J. Weiler, “The galactic contribution to IceCube’s astrophysical neutrino flux”, J. Cosmol. Astropart. Phys. **2017**, 8, 033 (2017).

Dias, W. S., B. S. Alessi, A. Moitinho and J. R. D. Lépine, “New catalogue of optically visible open clusters and candidates”, Astron. Astrophys. **389**, 871–873 (2002).

Diehl, R. and F. X. Timmes, “Gamma-Ray Line Emission from Radioactive Isotopes in Stars and Galaxies”, Publ. Astron. Soc. Pac. **110**, 748, 637–659 (1998).

Eichler, M., K. Nakamura, T. Takiwaki, T. Kuroda, K. Kotake, M. Hempel, R. Cabezón, M. Liebendörfer and F. K. Thielemann, “Nucleosynthesis in 2D core-collapse supernovae of 11.2 and 17.0 $M_\odot$ progenitors: implications for Mo and Ru production”, Journal of Physics G Nuclear Physics **45**, 1, 014001 (2018).

Ellinger, C. I., G. Rockefeller, C. L. Fryer, P. A. Young and S. Park, “First Simulations of Core- Collapse Supernovae to Supernova Remnants with SNSPH”, arXiv e-prints (2013).

Ellinger, C. I., P. A. Young, C. L. Fryer and G. Rockefeller, “A Case Study of Small-scale Structure Formation in Three-dimensional Supernova Simulations”, Astrophys. J. **755**, 160 (2012).

Emig, K., C. Lunardini and R. Windhorst, “Do high energy astrophysical neutrinos trace star formation?”, J. Cosmol. Astropart. Phys. **12**, 029 (2015).

Farnier, C., R. Walter and J. C. Leyder, “η Carinae: a very large hadron collider”, Astron. Astrophys. **526**, A57 (2011).

Ferguson, J. W., D. R. Alexander, F. Allard, T. Barman, J. G. Bodnarik, P. H. Hauschildt, A. Heffner-Wong and A. Tamanai, “Low-Temperature Opacities”, Astrophys. J. **623**, 585–596 (2005).

Fesen, R. A. and R. H. Becker, “New clues to the Cassiopeia A supernova progenitor”, Astrophys. J. **371**, 621–625 (1991).

Fiasson, A., J. A. Hinton, Y. Gallant, A. Marcowith, O. Reimer and G. Rowell, “The Monoceros very-high-energy gamma-ray source”, in “International Cosmic Ray Conference”, vol. 2 of *International Cosmic Ray Conference*, pp. 719–722 (2008).

Fryer, C. L., “Mass Limits For Black Hole Formation”, Astrophys. J. **522**, 413–418 (1999).

Fryer, C. L., S. Andrews, W. Even, A. Heger and S. Safi-Harb, “Parameterizing the Supernova Engine and Its Effect on Remnants and Basic Yields”, Astrophys. J. **856**, 63 (2018).

Fryer, C. L., K. Belczynski, G. Wiktorowicz, M. Dominik, V. Kalogera and D. E. Holz, “Compact Remnant Mass Function: Dependence on the Explosion Mechanism and Metallicity”, Astrophys. J. **749**, 91 (2012).

Fryer, C. L., C. Ellinger, P. A. Young and G. Vance, “Diagnostics of the Supernova Engine”, in “Supernova 1987A:30 years later - Cosmic Rays and Nuclei from Supernovae and their aftermaths, Proceedings of the International Astronomical Union, IAU Symposium, Volume 331, pp. 86-95”, vol. 331, pp. 86–95 (2017).

Fryer, C. L., A. L. Hungerford and F. X. Timmes, “Changing the r-Process Paradigm”, Nucl. Phys. A **758**, 599–602 (2005).

Fryer, C. L. and V. Kalogera, “Theoretical Black Hole Mass Distributions”, Astrophys. J. **554**, 548–560 (2001).

Fryer, C. L., G. Rockefeller and M. S. Warren, “SNSPH: A Parallel Three-dimensional Smoothed Particle Radiation Hydrodynamics Code”, Astrophys. J. **643**, 292–305 (2006).

Fryer, C. L., P. Young, M. Bennett, S. Diehl, F. Herwig, R. Hirschi, A. Hungerford, M. Pignatari, G. Magkotsios, G. Rockefeller and F. X. Timmes, “Nucleosynthesis Calculations from Core-Collapse Supernovae”, arXiv e-prints p. arXiv:0811.4648 (2008).

Fryer, C. L. and P. A. Young, “Late-Time Convection in the Collapse of a 23 M_{solar} Star”, Astrophys. J. **659**, 1438–1448 (2007).

Fujimoto, S.-i. and H. Nagakura, “The impact of asymmetric neutrino emissions on nucleosynthesis in core-collapse supernovae”, Mon. Not. R. Astron. Soc. **488**, 1, L114–L118 (2019).

Gabici, S., C. Evoli, D. Gaggero, P. Lipari, P. Mertsch, E. Orlando, A. Strong and A. Vittino, “The origin of Galactic cosmic rays: Challenges to the standard paradigm”, International Journal of Modern Physics D **28**, 15, 1930022–339 (2019).

Gaisser, T. and F. Halzen, “IceCube”, Annual Review of Nuclear and Particle Science **64**, 101–123 (2014).

Gaisser, T. K., *Cosmic Rays and Particle Physics* (Cambridge University Press, Cambridge [England] ; New York, 1990).

Graboske, H. C., H. E. Dewitt, A. S. Grossman and M. S. Cooper, “Screening Factors for Nuclear Reactions. II. Intermediate Screen-Ing and Astrophysical Applications”, Astrophys. J. **181**, 457–474 (1973).

Green, D. A., “A catalogue of 294 Galactic supernova remnants”, Bulletin of the Astronomical Society of India **42**, 47–58 (2014).

Green, D. A., “Constraints on the distribution of supernova remnants with Galactocentric radius”, Mon. Not. R. Astron. Soc. **454**, 1517–1524 (2015).

Green, D. A., “A Catalogue of Galactic Supernova Remnants (2017 June version)”, URL `http://www.mrao.cam.ac.uk/surveys/snrs/`, (available at “http://www.mrao.cam.ac.uk/surveys/snrs/”) (2017).

Grefenstette, B. W., C. L. Fryer, F. A. Harrison, S. E. Boggs, T. DeLaney, J. M. Laming, S. P. Reynolds, D. M. Alexander, D. Barret, F. E. Christensen, W. W. Craig, K. Forster, P. Giommi, C. J. Hailey, A. Hornstrup, T. Kitaguchi, J. E. Koglin, L. Lopez, P. H. Mao, K. K. Madsen, H. Miyasaka, K. Mori, M. Perri, M. J. Pivovaroff, S. Puccetti, V. Rana, D. Stern, N. J. Westergaard, D. R. Wik, W. W. Zhang and A. Zoglauer, “The Distribution of Radioactive ^{44}Ti in Cassiopeia A”, Astrophys. J. **834**, 19 (2017).

Grefenstette, B. W., F. A. Harrison, S. E. Boggs, S. P. Reynolds, C. L. Fryer, K. K. Madsen, D. R. Wik, A. Zoglauer, C. I. Ellinger, D. M. Alexander, H. An, D. Barret, F. E. Christensen, W. W. Craig, K. Forster, P. Giommi, C. J. Hailey, A. Hornstrup, V. M. Kaspi, T. Kitaguchi, J. E. Koglin, P. H. Mao, H. Miyasaka, K. Mori, M. Perri, M. J. Pivovaroff, S. Puccetti, V. Rana, D. Stern, N. J. Westergaard and W. W. Zhang, “Asymmetries in core-collapse supernovae from maps of radioactive ^{44}Ti in CassiopeiaA”, Nature **506**, 339–342 (2014).

Grimmett, J. J., A. Heger, A. I. Karakas and B. Müller, “Nucleosynthesis in primordial hypernovae”, Mon. Not. R. Astron. Soc. **479**, 495–516 (2018).

Gupta, N. and S. Razzaque, “Lepto-hadronic model of gamma rays from Eta Carinae and prospects for neutrino telescopes”, Phys. Rev. D **96**, 12, 123017 (2017).

H. E. S. S. Collaboration, H. Abdalla, A. Abramowski, F. Aharonian, F. Ait Benkhali, A. G. Akhperjanian, E. O. Angüner, M. Arrieta, P. Aubert, M. Backes, A. Balzer, M. Barnard, Y. Becherini, J. Becker Tjus, D. Berge, S. Bernhard, K. Bernlöhr, E. Birsin, R. Blackwell, M. Böttcher, C. Boisson, J. Bolmont, P. Bordas, J. Bregeon, F. Brun, P. Brun, M. Bryan, T. Bulik, M. Capasso, J. Carr, S. Casanova, N. Chakraborty, R. Chalme-Calvet, R. C. G. Chaves, A. Chen, J. Chevalier, M. Chrétien, S. Colafrancesco, G. Cologna, B. Condon, J. Conrad, C. Couturier, Y. Cui, I. D. Davids, B. Degrange, C. Deil, P. deWilt, A. Djannati-Ataï, W. Domainko, A. Donath, L. O. C. Drury, G. Dubus, K. Dutson, J. Dyks, M. Dyrda, T. Edwards, K. Egberts, P. Eger, J. P. Ernenwein, S. Eschbach, C. Farnier, S. Fegan, M. V. Fernandes, A. Fiasson, G. Fontaine, A. Förster, S. Funk, M. Füßling, S. Gabici, M. Gajdus, Y. A. Gallant, T. Garrigoux, G. Giavitto, B. Giebels, J. F. Glicenstein, D. Gottschall, A. Goyal, M. H. Grondin, M. Grudzińska, D. Hadasch, J. Hahn, J. Hawkes, G. Heinzelmann, G. Henri, G. Hermann, O. Hervet, A. Hillert, J. A. Hinton, W. Hofmann, C. Hoischen, M. Holler, D. Horns, A. Ivascenko, A. Jacholkowska, M. Jamrozy, M. Janiak, D. Jankowsky, F. Jankowsky, M. Jingo, T. Jogler, L. Jouvin, I. Jung-Richardt, M. A. Kastendieck, K. Katarzyński, U. Katz, D. Kerszberg, B. Khélifi, M. Kieffer, J. King, S. Klepser, D. Klochkov, W. Kluźniak, D. Kolitzus, N. Komin, K. Kosack, S. Krakau, M. Kraus, F. Krayzel, P. P. Krüger, H. Laffon, G. Lamanna, J. Lau, J. P. Lees, J. Lefaucheur, V. Lefranc, A. Lemière, M. Lemoine-Goumard, J. P. Lenain, E. Leser, T. Lohse, M. Lorentz, R. Liu, I. Lypova, V. Marandon, A. Marcowith, C. Mariaud, R. Marx, G. Maurin, N. Maxted, M. Mayer, P. J. Meintjes, U. Menzler, M. Meyer, A. M. W. Mitchell, R. Moderski, M. Mohamed, K. Morå, E. Moulin, T. Murach, M. de Naurois, F. Niederwanger, J. Niemiec, L. Oakes, H. Odaka, S. Öttl, S. Ohm, M. Ostrowski, I. Oya, M. Padovani, M. Panter, R. D. Parsons, M. Paz Arribas, N. W. Pekeur, G. Pelletier, P. O. Petrucci, B. Peyaud, S. Pita, H. Poon, D. Prokhorov, H. Prokoph, G. Pühlhofer, M. Punch, A. Quirrenbach, S. Raab, A. Reimer, O. Reimer, M. Renaud, R. de Reyes, F. Rieger, C. Romoli, S. Rosier-Lees, G. Rowell, B. Rudak, C. B. Rulten, V. Sahakian, D. Salek, D. A. Sanchez, A. Santangelo, M. Sasaki, R. Schlickeiser, F. Schüssler, A. Schulz, U. Schwanke, S. Schwemmer, A. S. Seyffert, N. Shafi, I. Shilon, R. Simoni, H. Sol, F. Spanier, G. Spengler, F. Spies, Ł. Stawarz, R. Steenkamp, C. Stegmann, F. Stinzing, K. Stycz, I. Sushch, J. P. Tavernet, T. Tavernier, A. M. Taylor, R. Terrier, M. Tluczykont, C. Trichard, R. Tuffs, J. van der Walt, C. van Eldik, B. van Soelen, G. Vasileiadis, J. Veh, C. Venter, A. Viana, P. Vincent, J. Vink, F. Voisin, H. J. Völk, T. Vuillaume, Z. Wadiasingh, S. J. Wagner, P. Wagner, R. M. Wagner, R. White, A. Wierzcholska, P. Willmann, A. Wörnlein, D. Wouters, R. Yang, V. Zabalza, D. Zaborov, M. Zacharias, A. A. Zdziarski, A. Zech, F. Zefi, A. Ziegler and N. Żywucka, “Extended VHE γ-ray emission towards SGR1806-20, LBV 1806-20, and stellar cluster Cl* 1806-20”, Astron. Astrophys. **612**, A11 (2018).

Halzen, F. and D. Hooper, “High-energy neutrino astronomy: the cosmic ray connection”, Reports on Progress in Physics **65**, 7, 1025–1078 (2002).

Halzen, F., A. Kheirandish and V. Niro, “Prospects for detecting galactic sources of cosmic neutrinos with IceCube: An update”, Astroparticle Physics **86**, 46–56 (2017).

Hamuy, M. and P. A. Pinto, “Type II Supernovae as Standardized Candles”, Astrophys. J. Lett. **566**, L63–L65 (2002).

Harris, J. A., W. R. Hix, M. A. Chertkow, C. T. Lee, E. J. Lentz and O. E. B. Messer, “Implications for Post-processing Nucleosynthesis of Core-collapse Supernova Models with Lagrangian Particles”, Astrophys. J. **843**, 1, 2 (2017).

Heng, K., “Balmer-Dominated Shocks: A Concise Review”, Publ. Astron. Soc. Aust. **27**, 1, 23–44 (2010).

Herant, M., “The convective engine paradigm for the supernova explosion mechanism and its consequences.”, Phys. Rep. **256**, 117–133 (1995).

Herant, M. and W. Benz, “Hydrodynamical Instabilities and Mixing in SN 1987A: Two-dimensional Simulations of the First 3 Months”, Astrophys. J. **370**, L81 (1991).

Herant, M. and W. Benz, “Postexplosion hydrodynamics of SN 1987A”, Astrophys. J. **387**, 294–308 (1992).

Herant, M., W. Benz, W. R. Hix, C. L. Fryer and S. A. Colgate, “Inside the supernova: A powerful convective engine”, Astrophys. J. **435**, 339–361 (1994).

Hoffman, R. D., S. E. Woosley, T. A. Weaver, T. Rauscher and F. K. Thielemann, “The Reaction Rate Sensitivity of Nucleosynthesis in Type II Supernovae”, Astrophys. J. **521**, 2, 735–752 (1999).

Hoffman, R. D., S. E. Woosley, T. A. Weaver, F. X. Timmes, R. G. Eastman and D. H. Hartmann, “Gamma-ray producing radioactivities from supernova explosions.”, in “Gamma Ray Sky with Compton GRO and SIGMA”, pp. 267–278 (1995).

Hooper, D., T. Linden and A. Vieregg, “Active galactic nuclei and the origin of IceCube’s diffuse neutrino flux”, J. Cosmol. Astropart. Phys. **2019**, 2, 012 (2019).

Hungerford, A. L., C. L. Fryer and G. Rockefeller, “Gamma Rays from Single-Lobe Supernova Explosions”, Astrophys. J. **635**, 487–501 (2005).

Hungerford, A. L., C. L. Fryer and M. S. Warren, “Gamma-Ray Lines from Asymmetric Supernovae”, Astrophys. J. **594**, 390–403 (2003).

Hwang, U., J. M. Laming, C. Badenes, F. Berendse, J. Blondin, D. Cioffi, T. DeLaney, D. Dewey, R. Fesen, K. A. Flanagan, C. L. Fryer, P. Ghavamian, J. P. Hughes, J. A. Morse, P. P. Plucinsky, R. Petre, M. Pohl, L. Rudnick, R. Sankrit, P. O. Slane, R. K. Smith, J. Vink and J. S. Warren, “A Million Second Chandra View of Cassiopeia A”, Astrophys. J. **615**, L117–L120 (2004).

IceCube Collaboration, “Evidence for High-Energy Extraterrestrial Neutrinos at the IceCube Detector”, Science **342**, 1242856 (2013).

IceCube Collaboration, “IceCube-190730A - IceCube observation of a high-energy neutrino candidate event”, Gamma-Ray Coordination Network (GCN), 25225, URL `https://gcn.gsfc.nasa.gov/gcn3/25225.gcn3` (2019).

IceCube Collaboration, M. G. Aartsen, M. Ackermann, J. Adams, J. A. Aguilar, M. Ahlers, M. Ahrens, I. A. Samarai, D. Altmann, K. Andeen, T. Anderson, I. Ansseau, G. Anton, C. Argüelles, B. Arsioli, J. Auffenberg, S. Axani, H. Bagherpour, X. Bai, J. P. Barron, S. W. Barwick, V. Baum, R. Bay, J. J. Beatty, J. Becker Tjus, K. H. Becker, S. BenZvi, D. Berley, E. Bernardini, D. Z. Besson, G. Binder, D. Bindig, E. Blaufuss, S. Blot, C. Bohm, M. Börner, F. Bos, S. Böser, O. Botner, E. Bourbeau, J. Bourbeau, F. Bradascio, J. Braun, M. Brenzke, H. P. Bretz, S. Bron, J. Brostean-Kaiser, A. Burgman, R. S. Busse, T. Carver, E. Cheung, D. Chirkin, A. Christov, K. Clark, L. Classen, S. Coenders, G. H. Collin, J. M. Conrad, P. Coppin, P. Correa, D. F. Cowen, R. Cross, P. Dave, M. Day, J. P. A. M. de André, C. De Clercq, J. J. DeLaunay, H. Dembinski, S. DeRidder, P. Desiati, K. D. de Vries, G. de Wasseige, M. de With, T. DeYoung, J. C. Díaz-Vélez, V. di Lorenzo, H. Dujmovic, J. P. Dumm, M. Dunkman, E. Dvorak, B. Eberhardt, T. Ehrhardt, B. Eichmann, P. Eller, P. A. Evenson, S. Fahey, A. R. Fazely, J. Felde, K. Filimonov, C. Finley, S. Flis, A. Franckowiak, E. Friedman, A. Fritz, T. K. Gaisser, J. Gallagher, L. Gerhardt, K. Ghorbani, P. Giommi, T. Glauch, T. Glüsenkamp, A. Goldschmidt, J. G. Gonzalez, D. Grant, Z. Griffith, C. Haack, A. Hallgren, F. Halzen, K. Hanson, D. Hebecker, D. Heereman, K. Helbing, R. Hellauer, S. Hickford, J. Hignight, G. C. Hill, K. D. Hoffman, R. Hoffmann, T. Hoinka, B. Hokanson-Fasig, K. Hoshina, F. Huang, M. Huber, K. Hultqvist, M. Hünnefeld, R. Hussain, S. In, N. Iovine, A. Ishihara, E. Jacobi, G. S. Japaridze, M. Jeong, K. Jero, B. J. P. Jones, P. Kalaczynski, W. Kang, A. Kappes, D. Kappesser, T. Karg, A. Karle, U. Katz, M. Kauer, A. Keivani, J. L. Kelley, A. Kheirandish, J. Kim, M. Kim, T. Kintscher, J. Kiryluk, T. Kittler, S. R. Klein, R. Koirala, H. Kolanoski, L. Köpke, C. Kopper, S. Kopper, J. P. Koschinsky, D. J. Koskinen, M. Kowalski, B. Krammer, K. Krings, M. Kroll, G. Krückl, S. Kunwar, N. Kurahashi, T. Kuwabara, A. Kyriacou, M. Labare, J. L. Lanfranchi, M. J. Larson, F. Lauber, K. Leonard, M. Lesiak-Bzdak, M. Leuermann, Q. R. Liu, C. J. Lozano Mariscal, L. Lu, J. Lünemann, W. Luszczak, J. Madsen, G. Maggi, K. B. M. Mahn, S. Mancina, R. Maruyama, K. Mase, R. Maunu, K. Meagher, M. Medici, M. Meier, T. Menne, G. Merino, T. Meures, S. Miarecki, J. Micallef, G. Momenté, T. Montaruli, R. W. Moore, R. Morse, M. Moulai, R. Nahnhauer, P. Nakarmi, U. Naumann, G. Neer, H. Niederhausen, S. C. Nowicki, D. R. Nygren, A. Obertacke Pollmann, A. Olivas, A. O’Murchadha, E. O’Sullivan, P. Padovani, T. Palczewski, H. Pand ya, D. V. Pankova, P. Peiffer, J. A. Pepper, C. Pérez de los Heros, D. Pieloth, E. Pinat, M. Plum, P. B. Price, G. T. Przybylski, C. Raab, L. Rädel, M. Rameez, K. Rawlins, I. C. Rea, R. Reimann, B. Relethford, M. Relich, E. Resconi, W. Rhode, M. Richman, S. Robertson, M. Rongen, C. Rott, T. Ruhe, D. Ryckbosch, D. Rysewyk, I. Safa, N. Sahakyan, T. Sälzer, S. E. Sanchez Herrera, A. Sandrock, J. Sandroos, M. Santander, S. Sarkar, S. Sarkar, K. Satalecka, P. Schlunder, T. Schmidt, A. Schneider, S. Schoenen, S. Schöneberg, L. Schumacher, S. Sclafani, D. Seckel, S. Seunarine, J. Soedingrekso, D. Soldin, M. Song, G. M. Spiczak, C. Spiering, J. Stachurska, M. Stamatikos, T. Stanev, A. Stasik, J. Stettner, A. Steuer, T. Stezelberger, R. G. Stokstad, A. Stößl, N. L. Strotjohann, T. Stuttard, G. W. Sullivan, M. Sutherland, I. Taboada, J. Tatar, F. Tenholt, S. Ter-Antonyan, A. Terliuk, S. Tilav, P. A. Toale, M. N. Tobin, C. Toennis, S. Toscano, D. Tosi, M. Tselengidou, C. F. Tung, A. Turcati, C. F. Turley, B. Ty, E. Unger, M. Usner, J. Vandenbroucke, W. Van Driessche, D. van Eijk, N. van Eijndhoven, S. Vanheule, J. van Santen, E. Vogel, M. Vraeghe, C. Walck, A. Wallace, M. Wallraff, F. D. Wandler, N. Wand kowsky, A. Waza, C. Weaver, M. J. Weiss, C. Wendt, J. Werthebach, S. Westerhoff, B. J. Whelan, N. Whitehorn, K. Wiebe, C. H. Wiebusch, L. Wille, D. R. Williams, L. Wills, M. Wolf, J. Wood, T. R. Wood, K. Woschnagg, D. L. Xu, X. W. Xu, Y. Xu, J. P. Yanez, G. Yodh, S. Yoshida and T. Yuan, "Neutrino emission from the direction of the blazar TXS 0506+056 prior to the IceCube-170922A alert", Science **361**, 147–151 (2018).

IceCube-Gen2 Collaboration, M. G. Aartsen, M. Ackermann, J. Adams, J. A. Aguilar, M. Ahlers, M. Ahrens, D. Altmann, T. Anderson, G. Anton, C. Arguelles, T. C. Arlen, J. Auffenberg, S. Axani, X. Bai, I. Bartos, S. W. Barwick, V. Baum, R. Bay, J. J. Beatty, J. Becker Tjus, K. H. Becker, S. BenZvi, P. Berghaus, D. Berley, E. Bernardini, A. Bernhard, D. Z. Besson, G. Binder, D. Bindig, M. Bissok, E. Blaufuss, J. Blumenthal, D. J. Boersma, C. Bohm, F. Bos, D. Bose, S. Böser, O. Botner, L. Brayeur, H. P. Bretz, A. M. Brown, N. Buzinsky, J. Casey, M. Casier, E. Cheung, D. Chirkin, A. Christov, B. Christy, K. Clark, L. Classen, F. Clevermann, S. Coenders, G. H. Collin, J. M. Conrad, D. F. Cowen, A. H. Cruz Silva, J. Daughhetee, J. C. Davis, M. Day, J. P. A. M. de André, C. De Clercq, S. De Ridder, P. Desiati, K. D. de Vries, M. de With, T. DeYoung, J. C. D. andaz-Vélez, M. Dunkman, R. Eagan, B. Eberhardt, T. Ehrhardt, B. Eichmann, J. Eisch, S. Euler, J. J. Evans, P. A. Evenson, O. Fadiran, A. R. Fazely, A. Fedynitch, J. Feintzeig, J. Felde, K. Filimonov, C. Finley, T. Fischer-Wasels, S. Flis, K. Frantzen, T. Fuchs, T. K. Gaisser, R. Gaior, J. Gallagher, L. Gerhardt, D. Gier, L. Gladstone, T. Glüsenkamp, A. Goldschmidt, G. Golup, J. G. Gonzalez, J. A. Goodman, D. Góra, D. Grant, P. Gretskov, J. C. Groh, A. Groß, C. Ha, C. Haack, A. Haj Ismail, P. Hallen, A. Hallgren, F. Halzen, K. Hanson, J. Haugen, D. Hebecker, D. Heereman, D. Heinen, K. Helbing, R. Hellauer, D. Hellwig, S. Hickford, J. Hignight, G. C. Hill, K. D. Hoffman, R. Hoffmann, A. Homeier, K. Hoshina, F. Huang, W. Huelsnitz, P. O. Hulth, K. Hultqvist, A. Ishihara, E. Jacobi, J. Jacobsen, G. S. Japaridze, K. Jero, O. Jlelati, B. J. P. Jones, M. Jurkovic, O. Kalekin, A. Kappes, T. Karg, A. Karle, T. Katori, U. F. Katz, M. Kauer, A. Keivani, J. L. Kelley, A. Kheirandish, J. Kiryluk, J. Kläs, S. R. Klein, J. H. Köhne, G. Kohnen, H. Kolanoski, A. Koob, L. Köpke, C. Kopper, S. Kopper, D. J. Koskinen, M. Kowalski, C. B. Krauss, A. Kriesten, K. Krings, G. Kroll, M. Kroll, J. Kunnen, N. Kurahashi, T. Kuwabara, M. Labare, J. L. Lanfranchi, D. T. Larsen, M. J. Larson, M. Lesiak-Bzdak, M. Leuermann, J. LoSecco, J. Lünemann, J. Madsen, G. Maggi, K. B. M. Mahn, S. Marka, Z. Marka, R. Maruyama, K. Mase, H. S. Matis, R. Maunu, F. McNally, K. Meagher, M. Medici, A. Meli, T. Meures, S. Miarecki, E. Middell, E. Middlemas, N. Milke, J. Miller, L. Mohrmann, T. Montaruli, R. W. Moore, R. Morse, R. Nahnhauer, U. Naumann, H. Niederhausen, S. C. Nowicki, D. R. Nygren, A. Obertacke, S. Odrowski, A. Olivas, A. Omairat,

A. O'Murchadha, T. Palczewski, L. Paul, Ö. Penek, J. A. Pepper, C. Pérez de los Heros, C. Pfendner, D. Pieloth, E. Pinat, J. L. Pinfold, J. Posselt, P. B. Price, G. T. Przybylski, J. Pütz, M. Quinnan, L. Rädel, M. Rameez, K. Rawlins, P. Redl, I. Rees, R. Reimann, M. Relich, E. Resconi, W. Rhode, M. Richman, B. Riedel, S. Robertson, J. P. Rodrigues, M. Rongen, C. Rott, T. Ruhe, B. Ruzybayev, D. Ryckbosch, S. M. Saba, H. G. Sander, J. Sandroos, P. Sandstrom, M. Santander, S. Sarkar, K. Schatto, F. Scheriau, T. Schmidt, M. Schmitz, S. Schoenen, S. Schöneberg, A. Schönwald, A. Schukraft, L. Schulte, O. Schulz, D. Seckel, Y. Sestayo, S. Seunarine, M. H. Shaevitz, R. Shanidze, M. W. E. Smith, D. Soldin, S. Söldner-Rembold, G. M. Spiczak, C. Spiering, M. Stamatikos, T. Stanev, N. A. Stanisha, A. Stasik, T. Stezelberger, R. G. Stokstad, A. Stöß andl, E. A. Strahler, R. Ström, N. L. Strotjohann, G. W. Sullivan, H. Taavola, I. Taboada, A. Taketa, A. Tamburro, H. K. M. Tanaka, A. Tepe, S. Ter-Antonyan, A. Terliuk, G. Teš, andić, S. Tilav, P. A. Toale, M. N. Tobin, D. Tosi, M. Tselengidou, E. Unger, M. Usner, S. Vallecorsa, N. van Eijndhoven, J. Vandenbroucke, J. van Santen, S. Vanheule, M. Vehring, M. Voge, M. Vraeghe, C. Walck, M. Wallraff, C. Weaver, M. Wellons, C. Wendt, S. Westerhoff, B. J. Whelan, N. Whitehorn, C. Wichary, K. Wiebe, C. H. Wiebusch, D. R. Williams, H. Wissing, M. Wolf, T. R. Wood, K. Woschnagg, S. Wren, D. L. Xu, X. W. Xu, Y. Xu, J. P. Yanez, G. Yodh, S. Yoshida, P. Zarzhitsky, J. Ziemann and M. Zoll, "IceCube-Gen2: A Vision for the Future of Neutrino Astronomy in Antarctica", arXiv e-prints p. arXiv:1412.5106 (2014).

Iglesias, C. A. and F. J. Rogers, "Updated Opal Opacities", Astrophys. J. **464**, 943 (1996).

Iliadis, C., J. M. D'Auria, S. Starrfield, W. J. Thompson and M. Wiescher, "Proton-induced Thermonuclear Reaction Rates for A=20-40 Nuclei", Astrophys. J. Suppl. **134**, 151–171 (2001).

Janka, H.-T., M. Gabler and A. Wongwathanarat, "Spatial distribution of radionuclides in 3D models of SN 1987A and Cas A", in "Supernova 1987A:30 years later - Cosmic Rays and Nuclei from Supernovae and their Aftermaths", vol. 331, pp. 148–156 (2017).

Janka, H.-T., T. Melson and A. Summa, "Physics of Core-Collapse Supernovae in Three Dimensions: A Sneak Preview", Annual Review of Nuclear and Particle Science **66**, 1, 341–375 (2016).

Katagiri, H., S. Sugiyama, M. Ackermann, J. Ballet, J. M. Casandjian, Y. Hanabata, J. W. Hewitt, M. Kerr, H. Kubo, M. Lemoine-Goumard and P. S. Ray, "Fermi/LAT Study of Gamma-Ray Emission in the Direction of the Monoceros Loop Supernova Remnant", Astrophys. J. **831**, 1, 106 (2016).

Kharchenko, N. V., A. E. Piskunov, S. Röser, E. Schilbach and R.-D. Scholz, "109 new Galactic open clusters", Astron. Astrophys. **440**, 403–408 (2005a).

Kharchenko, N. V., A. E. Piskunov, S. Röser, E. Schilbach and R.-D. Scholz, "Astrophysical parameters of Galactic open clusters", Astron. Astrophys. **438**, 1163–1173 (2005b).

Kheirandish, A. and J. Wood, “IceCube Search for Galactic Neutrino Sources based on HAWC Observations of the Galactic Plane”, in “36th International Cosmic Ray Conference (ICRC2019)”, vol. 36 of *International Cosmic Ray Conference*, p. 932 (2019).

Kobayashi, T., Y. Komori, K. Yoshida and J. Nishimura, “The Most Likely Sources of High-Energy Cosmic-Ray Electrons in Supernova Remnants”, Astrophys. J. **601**, 1, 340–351 (2004).

Krause, O., S. M. Birkmann, T. Usuda, T. Hattori, M. Goto, G. H. Rieke and K. A. Misselt, “The Cassiopeia A Supernova Was of Type IIb”, Science **320**, 1195 (2008).

Krone-Martins, A., C. Soubiran, C. Ducourant, R. Teixeira and J. F. Le Campion, “Kinematic parameters and membership probabilities of open clusters in the Bordeaux PM2000 catalogue”, Astron. Astrophys. **516**, A3 (2010).

Kudritzki, R. P., A. Pauldrach, J. Puls and D. C. Abbott, “Radiation-driven winds of hot stars. VI - Analytical solutions for wind models including the finite cone angle effect”, Astron. Astrophys. **219**, 205–218 (1989).

Lamers, H. J. G. L. M. and T. Nugis, “An explanation for the curious mass loss history of massive stars: From OB stars, through Luminous Blue Variables to Wolf-Rayet stars”, Astron. Astrophys. **395**, L1–L4 (2002).

Langanke, K. and G. Martínez-Pinedo, “Shell-model calculations of stellar weak interaction rates: II. Weak rates for nuclei in the mass range /A=45-65 in supernovae environments”, Nuclear Physics A **673**, 481–508 (2000).

Lattimer, J. M., “The Nuclear Equation of State and Neutron Star Masses”, Annual Review of Nuclear and Particle Science **62**, 1, 485–515 (2012).

Lauberts, A., *ESO/Uppsala survey of the ESO(B) atlas* (European Southern Observatory, ESO, Garching, 1982).

Lodders, K., “Solar System Abundances of the Elements”, Astrophysics and Space Science Proceedings **16**, 379 (2010).

Lucarelli, F., M. Tavani, G. Piano, A. Bulgarelli, I. Donnarumma, F. Verrecchia, C. Pittori, L. A. Antonelli, A. Argan, G. Barbiellini, P. Caraveo, M. Cardillo, P. W. Cattaneo, A. Chen, S. Colafrancesco, E. Costa, E. Del Monte, G. Di Cocco, A. Ferrari, V. Fioretti, M. Galli, P. Giommi, A. Giuliani, P. Lipari, F. Longo, S. Mereghetti, A. Morselli, F. Paoletti, N. Parmiggiani, A. Pellizzoni, P. Picozza, M. Pilia, A. Rappoldi, A. Trois, A. Ursi, S. Vercellone, V. Vittorini and AGILE Team, “AGILE Detection of Gamma-Ray Sources Coincident with Cosmic Neutrino Events”, Astrophys. J. **870**, 2, 136 (2019).

Lunardini, C., G. S. Vance, K. L. Emig and R. A. Windhorst, “Are starburst galaxies a common source of high energy neutrinos and cosmic rays?”, J. Cosmol. Astropart. Phys. **2019**, 10, 073 (2019).

Lyngå, G., *Computer Based Catalogue of Open Cluster Data* (CDS, Strasbourg, 1987), 5th edn.

Magkotsios, G., F. X. Timmes, A. L. Hungerford, C. L. Fryer, P. A. Young and M. Wiescher, "Trends in ^{44}Ti and ^{56}Ni from Core-collapse Supernovae", Astrophys. J. Suppl. **191**, 66–95 (2010).

Mandelartz, M. and J. Becker Tjus, "Prediction of the diffuse neutrino flux from cosmic ray interactions near supernova remnants", Astroparticle Physics **65**, 80–100 (2015).

Meakin, C. A. and D. Arnett, "Turbulent Convection in Stellar Interiors. I. Hydrodynamic Simulation", Astrophys. J. **667**, 448–475 (2007).

Melson, T., H.-T. Janka, R. Bollig, F. Hanke, A. Marek and B. Müller, "Neutrino-driven Explosion of a 20 Solar-mass Star in Three Dimensions Enabled by Strange-quark Contributions to Neutrino-Nucleon Scattering", Astrophys. J. Lett. **808**, L42 (2015).

Mermilliod, J. C., in "Information and On-Line Data in Astronomy", edited by D. Egret and M. A. Albrecht, p. 127 (Kluwer, Dordrecht, 1995).

Mirzoyan, R., "First-time detection of VHE gamma rays by MAGIC from a direction consistent with the recent EHE neutrino event IceCube-170922A", The Astronomer's Telegram **10817**, 1 (2017).

Moharana, R., P. Majumdar, P. P. Basumallick, D. Bose, R. Prince and N. Gupta, "Correlation of highly variable blazars with TeV IceCube track events", arXiv e-prints p. arXiv:2002.01661 (2020).

Moharana, R. and S. Razzaque, "Angular correlation of cosmic neutrinos with ultrahigh-energy cosmic rays and implications for their sources", J. Cosmol. Astropart. Phys. **2015**, 014 (2015).

Moharana, R. and S. Razzaque, "Angular correlation between IceCube high-energy starting events and starburst sources", J. Cosmol. Astropart. Phys. **2016**, 12, 021 (2016).

Mokiem, M. R., A. de Koter, C. J. Evans, J. Puls, S. J. Smartt, P. A. Crowther, A. Herrero, N. Langer, D. J. Lennon, F. Najarro, M. R. Villamariz and J. S. Vink, "The VLT-FLAMES survey of massive stars: wind properties and evolution of hot massive stars in the Large Magellanic Cloud", Astron. Astrophys. **465**, 1003–1019 (2007).

Morlino, G. and D. Caprioli, "Strong evidence for hadron acceleration in Tycho's supernova remnant", Astron. Astrophys. **538**, A81 (2012).

Murase, K. and E. Waxman, "Constraining high-energy cosmic neutrino sources: Implications and prospects", Phys. Rev. D **94**, 10, 103006 (2016).

Neronov, A. and D. Semikoz, "Evidence the Galactic contribution to the IceCube astrophysical neutrino flux", Astroparticle Physics **75**, 60–63 (2016).

Odrowski, S., Y. Sestayo and IceCube Collaboration, "Probing cosmic ray production in massive open star clusters with three years of IceCube data", in "International Cosmic Ray Conference", vol. 33 of *International Cosmic Ray Conference*, p. 3260 (2013).

Ohira, Y., K. Murase and R. Yamazaki, "Gamma-rays from molecular clouds illuminated by cosmic rays escaping from interacting supernova remnants", Mon. Not. R. Astron. Soc. **410**, 3, 1577–1582 (2011).

Ojha, R. and J. Valverd, "Fermi-LAT detection of enhanced gamma-ray activity and hard spectrum of TXS 0506+056, located inside the IceCube-170922A error region", The Astronomer's Telegram **11419**, 1 (2018).

Oort, J. H., "The force exerted by the stellar system in the direction perpendicular to the galactic plane and some related problems", Bulletin of the Astronomical Institutes of the Netherlands **6**, 249 (1932).

Orlando, S., M. Miceli, M. L. Pumo and F. Bocchino, "Modeling SNR Cassiopeia A from the Supernova Explosion to its Current Age: The Role of Post-explosion Anisotropies of Ejecta", Astrophys. J. **822**, 22 (2016).

Palladino, A., A. Fedynitch, R. W. Rasmussen and A. M. Taylor, "IceCube Neutrinos from Hadronically Powered Gamma-Ray Galaxies", arXiv e-prints p. arXiv:1812.04685 (2018).

Palladino, A. and F. Vissani, "Extragalactic plus Galactic Model for IceCube Neutrino Events", Astrophys. J. **826**, 185 (2016).

Park, S., J. P. Hughes, P. O. Slane, D. N. Burrows, B. M. Gaensler and P. Ghavamian, "A Half-Megasecond Chandra Observation of the Oxygen-rich Supernova Remnant G292.0+1.8", Astrophys. J. **670**, L121–L124 (2007).

Press, W. H., S. A. Teukolsky, W. T. Vetterling and B. P. Flannery, *Numerical Recipes in C: The Art of Scientific Computing* (Cambridge University Press, New York, NY, USA, 1992), 2 edn.

Price, D. J., "splash: An Interactive Visualisation Tool for Smoothed Particle Hydrodynamics Simulations", Publ. Astron. Soc. Aust. **24**, 3, 159–173 (2007).

Ptuskin, V., V. Zirakashvili and E.-S. Seo, "Spectrum of Galactic Cosmic Rays Accelerated in Supernova Remnants", Astrophys. J. **718**, 1, 31–36 (2010).

Radice, D., E. Abdikamalov, C. D. Ott, P. Mösta, S. M. Couch and L. F. Roberts, "Turbulence in core-collapse supernovae", Journal of Physics G Nuclear Physics **45**, 053003 (2018).

Rauscher, T., R. D. Hoffman, S. E. Woosley and F.-K. Thielemann, "Prediction of astrophysical reaction rates: Methods, data needs, and consequences for nucleosynthesis studies", in "American Institute of Physics Conference Series", vol. 529 of *American Institute of Physics Conference Series*, pp. 331–338 (2000).

Rogers, F. J. and A. Nayfonov, "Updated and Expanded OPAL Equation-of-State Tables: Implications for Helioseismology", Astrophys. J. **576**, 1064–1074 (2002).

Saez, M. M., O. Civitarese and M. E. Mosquera, "Neutrino-induced reactions in core-collapse supernovae: Effects on the electron fraction", International Journal of Modern Physics D **27**, 12, 1850116–27 (2018).

Scheck, L., K. Kifonidis, H.-T. Janka and E. Müller, "Multidimensional supernova simulations with approximative neutrino transport. I. Neutron star kicks and the anisotropy of neutrino-driven explosions in two spatial dimensions", Astron. Astrophys. **457**, 963–986 (2006).

Schure, K. M., A. R. Bell, L. O'C Drury and A. M. Bykov, "Diffusive Shock Acceleration and Magnetic Field Amplification", Space Sci. Rev. **173**, 1-4, 491–519 (2012).

Serenelli, A. M., S. Basu, J. W. Ferguson and M. Asplund, "New Solar Composition: The Problem with Solar Models Revisited", Astrophys. J. Lett. **705**, L123–L127 (2009).

Sparke, L. S. and J. S. Gallagher, III, *Galaxies in the Universe: An Introduction* (Cambridge University Press, New York, NY, USA, 2007), 2 edn.

Speagle, J. S., "DYNESTY: a dynamic nested sampling package for estimating Bayesian posteriors and evidences", Mon. Not. R. Astron. Soc. **493**, 3, 3132–3158 (2020).

Su, Y., X. Zhou, J. Yang, X. Chen, Y. Chen, Y. Liu, H. Wang, C. Li and S. Zhang, "Molecular Environments of Three Large Supernova Remnants in the Third Galactic Quadrant: G205.5+0.5, G206.9+2.3, and G213.0-0.6", Astrophys. J. **836**, 2, 211 (2017).

Sudoh, T., T. Totani and N. Kawanaka, "High-energy gamma-ray and neutrino production in star-forming galaxies across cosmic time: Difficulties in explaining the IceCube data", Publ. Astron. Soc. Jpn. **70**, 3, 49 (2018).

Sutherland, W. and W. Saunders, "On the likelihood ratio for source identification.", Mon. Not. R. Astron. Soc. **259**, 413–420 (1992).

Takiwaki, T., K. Kotake and Y. Suwa, "A Comparison of Two- and Three-dimensional Neutrino-hydrodynamics Simulations of Core-collapse Supernovae", Astrophys. J. **786**, 83 (2014).

Tavani, M., A. Giuliani, A. W. Chen, A. Argan, G. Barbiellini, A. Bulgarelli, P. Caraveo, P. W. Cattaneo, V. Cocco, T. Contessi, F. D'Ammando, E. Costa, G. De Paris, E. Del Monte, G. Di Cocco, I. Donnarumma, Y. Evangelista, A. Ferrari, M. Feroci, F. Fuschino, M. Galli, F. Gianotti, C. Labanti, I. Lapshov, F. Lazzarotto, P. Lipari, F. Longo, M. Marisaldi, M. Mastropietro, S. Mereghetti, E. Morelli, E. Moretti, A. Morselli, L. Pacciani, A. Pellizzoni, F. Perotti, G. Piano, P. Picozza, M. Pilia, G. Pucella, M. Prest, M. Rapisarda, A. Rappoldi, E. Scalise, A. Rubini, S. Sabatini, E. Striani, P. Soffitta, M. Trifoglio, A. Trois, E. Vallazza, S. Vercellone, V. Vittorini, A. Zambra, D. Zanello, C. Pittori, F. Verrecchia, P. Santolamazza, P. Giommi, S. Colafrancesco, L. A. Antonelli and L. Salotti, "Direct Evidence for Hadronic Cosmic-Ray Acceleration in the Supernova Remnant IC 443", Astrophys. J. Lett. **710**, 2, L151–L155 (2010).

Tavani, M., S. Sabatini, E. Pian, A. Bulgarelli, P. Caraveo, R. F. Viotti, M. F. Corcoran, A. Giuliani, C. Pittori, F. Verrecchia, S. Vercellone, S. Mereghetti, A. Argan, G. Barbiellini, F. Boffelli, P. W. Cattaneo, A. W. Chen, V. Cocco, F. D'Ammando, E. Costa, G. DeParis, E. Del Monte, G. Di Cocco, I. Donnarumma, Y. Evangelista, A. Ferrari, M. Feroci, M. Fiorini, T. Froysland, F. Fuschino, M. Galli, F. Gianotti, C. Labanti, I. Lapshov, F. Lazzarotto, P. Lipari, F. Longo, M. Marisaldi, M. Mastropietro, E. Morelli, E. Moretti, A. Morselli, L. Pacciani, A. Pellizzoni, F. Perotti, G. Piano, P. Picozza, M. Pilia, G. Porrovecchio, G. Pucella, M. Prest, M. Rapisarda, A. Rappoldi, A. Rubini, P. Soffitta, M. Trifoglio, A. Trois, E. Vallazza, V. Vittorini, A. Zambra, D. Zanello, P. Santolamazza, P. Giommi, S. Colafrancesco, L. A. Antonelli and L. Salotti, "Detection of Gamma-Ray Emission from the Eta-Carinae Region", Astrophys. J. Lett. **698**, 2, L142–L146 (2009).

Thielemann, F.-K., M.-A. Hashimoto and K. Nomoto, "Explosive Nucleosynthesis in SN 1987A. II. Composition, Radioactivities, and the Neutron Star Mass", Astrophys. J. **349**, 222 (1990).

Thielemann, F.-K., K. Nomoto and M.-A. Hashimoto, "Core-Collapse Supernovae and Their Ejecta", Astrophys. J. **460**, 408 (1996).

Thorsett, S. E. and D. Chakrabarty, "Neutron Star Mass Measurements. I. Radio Pulsars", Astrophys. J. **512**, 288–299 (1999).

Thoul, A. A., J. N. Bahcall and A. Loeb, "Element diffusion in the solar interior", Astrophys. J. **421**, 828–842 (1994).

Timmes, F. X. and D. Arnett, "The Accuracy, Consistency, and Speed of Five Equations of State for Stellar Hydrodynamics", Astrophys. J. Suppl. **125**, 277–294 (1999).

Vance, G. S., K. L. Emig, C. Lunardini and R. A. Windhorst, "Searching for a Galactic component in the IceCube track-like neutrino events", arXiv e-prints p. arXiv:2108.01805 (2021).

Vance, G. S., P. A. Young, C. L. Fryer and C. I. Ellinger, "Titanium and Iron in the Cassiopeia A Supernova Remnant", Astrophys. J. **895**, 2, 82 (2020).

Villante, F. L. and F. Vissani, “How precisely can neutrino emission from supernova remnants be constrained by gamma ray observations?”, Phys. Rev. D **78**, 10, 103007 (2008).

Vink, J., “Supernova remnants: the X-ray perspective”, Astron. Astrophys. Rev. **20**, 49 (2012).

Vink, J. S., A. de Koter and H. J. G. L. M. Lamers, “Mass-loss predictions for O and B stars as a function of metallicity”, Astron. Astrophys. **369**, 574–588 (2001).

Virmani, A., S. Bhattacharya, P. Jain, S. Razzaque, J. P. Ralston and D. W. Mckay, “Angular correlation of ultra-high energy cosmic rays with compact radio-loud quasars”, Astroparticle Physics **17**, 489–495 (2002).

Völk, H. J., E. G. Berezhko and L. T. Ksenofontov, “Magnetic field amplification in Tycho and other shell-type supernova remnants”, Astron. Astrophys. **433**, 1, 229–240 (2005).

Wiescher, M., R. E. Azuma, L. Gasques, J. Görres, M. Pignatari and E. Simpson, “Charged particle reaction rates from stellar H to C burning.”, Mem. Soc. Astron. Italiana **77**, 910 (2006).

Windhorst, R. A., R. G. Kron and D. C. Koo, “A deep Westerbork survey of areas with multicolor Mayall 4 m plates. II. Optical identifications.”, Astronomy and Astrophysics Supplement Series **58**, 39–87 (1984).

Wong, T.-W., C. L. Fryer, C. I. Ellinger, G. Rockefeller and V. Kalogera, “The Fallback Mechanisms in Core-Collapse Supernovae”, arXiv e-prints (2014).

Wongwathanarat, A., H.-T. Janka, E. Müller, E. Pllumbi and S. Wanajo, “Production and Distribution of ^{44}Ti and ^{56}Ni in a Three-dimensional Supernova Model Resembling Cassiopeia A”, Astrophys. J. **842**, 13 (2017).

Woosley, S. E. and A. Heger, “Nucleosynthesis and remnants in massive stars of solar metallicity”, Phys. Rep. **442**, 1-6, 269–283 (2007).

Xiao, L. and M. Zhu, “Radio perspectives on the Monoceros SNR G205.5+0.5”, Astron. Astrophys. **545**, A86 (2012).

Yoast-Hull, T. M., J. S. Gallagher, F. Halzen, A. Kheirandish and E. G. Zweibel, “Gamma-ray puzzle in Cygnus X: Implications for high-energy neutrinos”, Phys. Rev. D **96**, 4, 043011 (2017).

Young, P. A. and D. Arnett, “Observational Tests and Predictive Stellar Evolution. II. Nonstandard Models”, Astrophys. J. **618**, 908–918 (2005).

Young, P. A., C. I. Ellinger, D. Arnett, C. L. Fryer and G. Rockefeller, “Finding Tracers for Supernova Produced ^{26}Al”, Astrophys. J. **699**, 938–947 (2009).

Young, P. A. and C. L. Fryer, “Uncertainties in Supernova Yields. I. One-dimensional Explosions”, Astrophys. J. **664**, 1033–1044 (2007).

Young, P. A., C. L. Fryer, A. Hungerford, D. Arnett, G. Rockefeller, F. X. Timmes, B. Voit, C. Meakin and K. A. Eriksen, “Constraints on the Progenitor of Cassiopeia A”, Astrophys. J. **640**, 891–900 (2006).

Young, P. A., K. A. Knierman, J. R. Rigby and D. Arnett, “Stellar Hydrodynamics in Radiative Regions”, Astrophys. J. **595**, 2, 1114–1123 (2003).

Young, P. A., C. Meakin, D. Arnett and C. L. Fryer, “The Impact of Hydrodynamic Mixing on Supernova Progenitors”, Astrophys. J. **629**, L101–L104 (2005).

Yuan, Q., P.-F. Yin and X.-J. Bi, “Neutrino emission of Fermi supernova remnants”, Astroparticle Physics **35**, 1, 33–38 (2011).

APPENDIX A

PREVIOUSLY PUBLISHED WORKS

The content of Chapter 2 was previously published by the Astrophysical Journal (ApJ) in June of 2020. See Vance *et al.* (2020).

The content of Chapter 3 was been submitted for publication to the Journal of Cosmology and Astroparticle Physics (JCAP) in August of 2021. It is currently in revision. See Vance *et al.* (2021) for a pre-print.

The content of Chapter 4 is intended for publication by the Astrophysical Journal (ApJ), but has yet to be submitted for review.

APPENDIX B

YIELDS TABLES

Table B.1: Yields Table for Model 15M_sym

Proton Number Z	Neutron Number N	Total Mass ($M_\odot$)	Mass Fraction X
0	1	8.647287e–14	3.363734e–14
1	0	8.895792e–06	3.460400e–06
1	1	6.087662e–18	2.368057e–18
1	2	7.917633e–20	3.079903e–20
2	1	2.481677e–20	9.653548e–21
2	2	2.790301e–01	1.085408e–01
3	3	7.848494e–19	3.053009e–19
3	4	2.648172e–18	1.030120e–18
4	3	7.729604e–12	3.006762e–12
4	4	5.040389e–09	1.960676e–09
⋮	⋮	⋮	⋮

NOTE—This table, as well as the other yields tables, are published in their entirety in the machine-readable format. Portions are shown here for guidance regarding their form and content.

Table B.2: Yields Table for Model 15M_bip

Proton Number Z	Neutron Number N	Total Mass ($M_\odot$)	Mass Fraction X
0	1	3.093065e–34	1.203437e–34
1	0	7.251425e–06	2.821356e–06
1	1	8.974725e–18	3.491851e–18
1	2	4.254771e–19	1.655430e–19
2	1	1.215010e–19	4.727313e–20
2	2	2.793740e–01	1.086978e–01
3	3	1.172858e–18	4.563311e–19
3	4	2.777630e–18	1.080710e–18
4	3	3.199080e–16	1.244685e–16
4	4	4.986594e–09	1.940164e–09
⋮	⋮	⋮	⋮

NOTE—This table, as well as the other yields tables, are published in their entirety in the machine-readable format. Portions are shown here for guidance regarding their form and content.

Table B.3: Yields Table for Model 15M_dco

Proton Number Z	Neutron Number N	Total Mass ($\mathrm{M}_\odot$)	Mass Fraction X
0	1	4.122962e–06	1.642001e–06
1	0	4.151149e–06	1.653227e–06
1	1	8.101277e–10	3.226396e–10
1	2	4.260988e–12	1.696971e–12
2	1	1.767639e–12	7.039758e–13
2	2	3.457885e–01	1.377129e–01
3	3	4.857823e–16	1.934665e–16
3	4	2.502545e–16	9.966577e–17
4	3	4.912367e–16	1.956388e–16
4	4	1.123973e–08	4.476309e–09
⋮	⋮	⋮	⋮

NOTE—This table, as well as the other yields tables, are published in their entirety in the machine-readable format. Portions are shown here for guidance regarding their form and content.

Table B.4: Yields Table for Model 20M_sym

Proton Number Z	Neutron Number N	Total Mass ($\mathrm{M}_\odot$)	Mass Fraction X
0	1	5.529408e–20	1.245207e–20
1	0	1.313295e–07	2.957503e–08
1	1	1.645781e–10	3.706253e–11
1	2	3.932126e–13	8.855037e–14
2	1	4.127007e–11	9.293905e–12
2	2	4.923993e–01	1.108869e–01
3	3	3.937471e–13	8.867074e–14
3	4	3.264397e–11	7.351330e–12
4	3	1.024689e–11	2.307571e–12
4	4	6.775228e–09	1.525762e–09
⋮	⋮	⋮	⋮

NOTE—This table, as well as the other yields tables, are published in their entirety in the machine-readable format. Portions are shown here for guidance regarding their form and content.

Table B.5: Yields Table for Model 20M_bip

Proton Number Z	Neutron Number N	Total Mass ($M_\odot$)	Mass Fraction X
0	1	4.405345e–28	1.133944e–28
1	0	1.617949e–05	4.164628e–06
1	1	2.434183e–14	6.265629e–15
1	2	1.994425e–19	5.133685e–20
2	1	6.871522e–15	1.768742e–15
2	2	2.818679e–01	7.255329e–02
3	3	2.714983e–17	6.988413e–18
3	4	7.789617e–18	2.005061e–18
4	3	1.343879e–14	3.459168e–15
4	4	1.455943e–07	3.747623e–08
⋮	⋮	⋮	⋮

NOTE—This table, as well as the other yields tables, are published in their entirety in the machine-readable format. Portions are shown here for guidance regarding their form and content.

Table B.6: Yields Table for Model 20M_equ

Proton Number Z	Neutron Number N	Total Mass ($M_\odot$)	Mass Fraction X
0	1	1.253074e–26	2.584363e–27
1	0	1.305948e–05	2.693413e–06
1	1	1.725701e–13	3.559119e–14
1	2	1.007780e–18	2.078465e–19
2	1	5.338820e–14	1.101089e–14
2	2	5.971839e–01	1.231644e–01
3	3	3.441024e–16	7.096835e–17
3	4	1.725504e–16	3.558712e–17
4	3	1.089466e–13	2.246935e–14
4	4	1.269082e–07	2.617379e–08
⋮	⋮	⋮	⋮

NOTE—This table, as well as the other yields tables, are published in their entirety in the machine-readable format. Portions are shown here for guidance regarding their form and content.